Electrochemical Deposition Based Micro-Additive Manufacturing System

A thesis submitted

in partial fulfillment of the requirements

for the degree of

Doctor of Philosophy

By

Anand Mohan Pandey

Roll No:-196103004

Department of Mechanical Engineering

Indian Institute of Technology Guwahati

Guwahati - 781039

June 2024

TH-3378_196103004

Department of Mechanical Engineering
Indian Institute of Technology Guwahati
Guwahati-781039
INDIA

CERTIFICATE

It is certified that the work contained in the thesis entitled "**Electrochemical Deposition Based Micro-Additive Manufacturing System**," submitted by **Anand Mohan Pandey**, Roll No. 196103004, to the Indian Institute of Technology Guwahati for the degree of Doctor of Philosophy has been carried out under our supervision in the Department of Mechanical Engineering, Indian Institute of Technology Guwahati. This work has not been submitted elsewhere for the award of any other degree or diploma.

Dr. Sajan Kapil
Department of Mechanical Engineering
Indian Institute of Technology Guwahati
Guwahati-781039, Assam, India
Date: 10/06/2024

Dr. Manas Das
Department of Mechanical Engineering
Indian Institute of Technology Guwahati
Guwahati-781039, Assam, India
Date: 10/06/2024

Declaration

I declare that this written submission represents my idea in my own words, and where others' ideas or words have been included, I have adequately cited and referenced the original sources. I also declare that I have adhered to all principles of academic honesty and integrity and have not misrepresented or fabricated or falsified any idea/data/fact/source in my submission. I understand that any violation of the above will be cause for disciplinary action by the institute can also evoke penal action from the sources which have thus not been properly cited or from whom proper permission has not been taken when needed.

Date: 10.06.2024

Anand Mohan Pandey
Roll No.: 196103004

TH-3378_196103004

Dedicated to

My Teachers

TH-3378_196103004

ACKNOWLEDGEMENT

I would like to take this opportunity to pay my deep sense of respect and sincere gratitude to my supervisor, Dr. Sajan Kapil and Dr. Manas Das, Department of Mechanical Engineering, Indian Institute of Technology Guwahati, Assam-781039 for their invaluable advice, resourceful guidance, inspiring instructions, active supervision and constant encouragement without which it would not have been possible for me to reach to this point.

I also wish to thank my doctoral committee members, Dr. Swarup Bag, Dr. Prasenjit Khanikar, and Prof. Ramagopal V. S. Uppaluri, for their guidance, moral support, and encouragement of my ideas in the subject as well as other areas of innovations. I must not miss the opportunity to thank all the Professors of the Mechanical Engineering Department, Indian Institute of Technology Guwahati, whose motivation and timely help molded me in all possible forms.

I would also like to thank Mr. Jiten Basumatary for his support in my work in the advanced manufacturing lab. I am very thankful to workshop superintendent Mr. N. K. Das and workshop technicians Mr. Upen Gohain and Mr. Santosh Gogoi for their help in fabricating my experimental setup and workpieces. I would like to acknowledge the Central Instrument Facility (CIF) of IIT Guwahati for its kind assistance in my research work.

Last but not least, I am deeply indebted to my parents for their sacrifices to ensure my dreams' fulfillment. I would like to thank my family for their support and motivation during my PhD.

The time I spent with all my friends and seniors at IIT Guwahati, Dr. Ambrish Singh, Dr. Hari Narayan Singh Yadav, Dr. Atul Singh Rajput, Dr. Manjesh Kumar, Dr. Abhinav Kumar, Ranajit Mahanti, Akash Tyagi, Kanak Jindal, Ravi Prakash, and Ritam sarma, who made my life enjoyable and memorable on the campus.

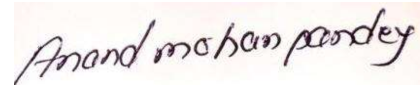

ANAND MOHAN PANDEY

Abstract

Metal-based micro-manufacturing involves fabricating miniature components using micro-tools while maintaining tolerances to only a few microns. This precise manufacturing method enables engineers to create tiny and intricately designed parts that find applications across various aerospace, automotive, and biomedical industries. The increasing demand for micro-electromechanical systems (MEMS), including actuators and sensors, underscores significant micro-manufacturing techniques while producing these components. Metal-based micro-manufacturing techniques often involve material deposition at an atomic level utilizing the electrodeposition principle, ensuring precise and accurate features. To achieve effective micro-manufacturing, specialized machinery equipped with high-accuracy motion systems capable of sub-micron resolution, high-speed spindles, and miniature-cutting tools are essential. These advanced tools and systems enable the demanding requirements of micro-manufacturing processes, ensuring the production of high-quality micro components.

Metal-based micro-manufacturing, utilizing the electrodeposition principle, can be executed through various processes, namely mask-based electrodeposition and maskless electrodeposition. Examples of mask-based electrodeposition processes include LIGA (German acronym for Lithographie, Galvanoformung, Abformung) and EFAB (Electrochemical Fabrication). On the other hand, examples of mask-less electrodeposition processes include Localized Electrodeposition (LED) and Selective Jet Electrodeposition (SJED). Mask-based micro-manufacturing techniques, such as LIGA and EFAB, face significant challenges due to the requirement of masks for each layer of deposition. These techniques often involve various hazardous chemicals, rendering them costly and environmentally unfriendly. The slow material deposition rate and high energy consumption are significant challenges of mask-based micro-manufacturing approaches. A mask-less electrodeposition method called Selective Jet Electrodeposition (SJED) is developed to address the challenges encountered with mask-based electrodeposition processes. SJED enables material deposition atom-by-atom, offering several advantages over traditional mask-based techniques. By eliminating the need for masks, SJED simplifies the manufacturing process, reducing production costs and environmental impact associated with mask fabrication and disposal. Additionally, SJED allows for greater flexibility and precision in material deposition, enabling the creation of intricate geometries with high resolution.

The SJED experimental setup has been designed and developed in the present study to fabricate micro-features. The developed setup consists of several subsystems: a power

TH-3378_196103004

supply unit, tool and workpiece holding unit, electrolyte circulation unit, and a CNC controller for precise movement. The electrolyte container is made of Perspex, a non-conductive and non-reactive material; hence, there is no charge loss during the process. A fixture is also developed to hold and provide a power supply to the workpiece.

The computer-aided process planning (CAPP) is developed with the help of SJED setup. The CAPP developed for nickel and copper depositions consists of three steps: preprocess, in-process, and post-process. The primary goal of developing CAPP is to facilitate the separation of micro parts from the substrate. This task is challenging due to the strong chemical bond formed between the deposited parts and the substrate, making it challenging to achieve separation using mechanical forces alone.

The experimental investigation was carried out for nickel and copper, considering process parameters, such as applied voltage, scanning speed, and inter-electrode gap, to obtain uniform deposition. The optimized values of the parameters selected from the single-bead deposition experimentation are considered for the multi-bead deposition. Further experimentation for multi-bead optimization is performed considering different center distances between the adjacent beads to achieve the flat surface condition.

Several toolpath strategies were also studied as part of the present study. The selection of a toolpath strategy for the deposition of material in the SJED process influences part properties and process efficiency. Space-filling Curves (SFCs) offer a unique opportunity in additive manufacturing (AM) to fabricate parts with a high strength-to-weight ratio and include a density gradient in the final product. However, an SFC should often have properties such as a common start and stop point, a minimal number of turns, and very few retractions/lifts. A Traveling Salesman Problem (TSP) based solver is utilized to synthesize a toolpath with the aforementioned properties. The optimized center distance is used for the above-mentioned toolpath strategy. By employing a Traveling Salesman Problem (TSP) approach, a toolpath with a density gradient is achieved through the strategic clustering of grid points. Areas with a high concentration of grid points will produce a densely packed toolpath, resulting in more material deposition, whereas regions with fewer grid points will yield scattered material deposition. The gradient-based microstructure (nickel and copper) is deposited with the help of the above-mentioned strategy. Finally, with the help of the tool path strategy, a thick coating is developed and compared with the conventional coating technique. The developed SJED setup is further utilized for micromanufacturing and coating purposes.

TH-3378_196103004

Table of Contents

List of Figures vi

List of Tables xi

Nomenclature xii

Chapter 1 Introduction 1

1.1 Electrochemical deposition-based micro additive manufacturing 3

1.1.1 Mask-based micro MEAM 5

1.1.2 Mask-less micro MEAM 7

1.2 Motivation for present work 10

1.3 Objectives of present thesis 10

1.4 Organization of thesis 11

Chapter 2 Literature survey 13

2.1 Introduction 13

2.1.1 Development of LECD experimental setup 13

2.1.2 Influence of significant process parameters in LECD 15

2.1.3 Microfabrication by LECD 17

2.1.4 Literature summary for LECD 18

2.1.5 Development of SJED Experimental setup 19

2.1.6 Principle of micro-electrodeposition for SJED process 20

2.1.7 Kinetics of micro-electrodeposition for SJED process 21

2.1.8 Major process parameters in SJED 24

2.1.9 Microfabrication by SJED 28

2.1.10 Characterization of deposited microparts by SJED 28

2.1.11 Literature summary for SJED 30

2.2 Scope of research 31

2.3 Research contribution 31

Chapter 3 Development of SJED process for micro-additive manufacturing ..32

3.1 Introduction 32

3.2 SJED setup 32

3.2.1 Power supply unit 33

3.2.2 Electrolyte circulation and nozzle unit 34

3.2.3 CNC control unit 36

TH-3378_196103004

3.3 Computer-aided process planning for SJED process 37
3.3.1 CAPP for nickel-based SJED process 38
3.3.2 CAPP for copper-based SJED process 39
3.4 Summary 40
Chapter 4 Parametric investigation and toolpath strategies for SJED process 41
4.1 Introduction 41
4.2 Nickel deposition through SJED process 41
4.2.1 Materials and method 42
4.2.2 Process parameters 43
4.2.3 Influence of process parameters on deposition profile/morphology 43
4.2.4 Multi-bead analysis 54
4.3 Copper deposition through SJED process 56
4.3.1 Materials and method 57
4.3.2 Process parameters 57
4.3.3 Influence of process parameters on deposition profile/morphology 58
4.4 Summary 71
Chapter 5 Application of SJED process in micromanufacturing and coating . 72
5.1 Introduction 72
5.2 Manufacturing of nickel-based complicated features through SJED process 72
5.2.1 Deposition and separation of circuit 72
5.2.2 Deposition and separation of density-based complex structure 73
5.3 Manufacturing of copper-based complicated features through SJED process ... 74
5.3.1 Deposition of density-based structure 75
5.3.2 Deposition and separation of density-based complex structure 76
5.4 Development of thick coatings through SJED and conventional methods 77
5.4.1 Coating by conventional method 77
5.4.2 Coating by SJED method 78
5.4.3 Comparative studies of surface topography and mechanical properties of coatings 79
5.5 Summary 83
Chapter 6 Conclusions, and scope for future work 84
6.1 Conclusions 84
6.1.1 Selective jet electrodeposition (SJED) 84
6.2 Scope for future work 87

TH-3378_196103004

Appendix A1 Statistical DOE study of thick coating by SJED process 88

A1.1 Introduction 88

A1.2 Materials and method 91

A1.3 Results and discussion 93

A1.3.1 ANOVA study 93

A1.3.2 Parametric study using response surface plots 94

A1.3.3 Optimization study using desirability function-based approach 97

A1.3.4 Validation of developed model 99

A1.3.5 Multi-bead optimization for flat surface condition 100

A1.3.6 Summary 101

Appendix A2 Experimental investigation of electrochemical deposition-based micro-additive manufacturing process 103

A2.1 Introduction 103

A2.2 Materials and method 106

A2.3 Results and discussion 109

A2.3.1 Effect of process parameters 110

A2.3.2 Combined effect of process parameters 113

A2.3.3 Optimization study 117

A2.3.4 Validation of ANOVA model 118

A2.3.5 Surface characterization of deposit 121

A2.3.6 Summary 122

References 122

Publications 137

TH-3378_196103004

List of Figures

Fig. 1.1 (a) Process sequence for additive manufacturing with pre-processing, (b) AM Classification, and (c) few post-processing techniques for quality improvement of AM parts 2

Fig. 1.2 Flow chart of micro-manufacturing process based on material removal 5

Fig. 1.3 Instant masking (IM) plating process 7

Fig. 1.4 Schematic diagram of localized electrochemical deposition 8

Fig. 1.5 Schematic diagram of selective jet electrodeposition process 9

Fig. 2.1 Major process parameters in LECD process 16

Fig. 2.2 Interaction of jet with substrate 21

Fig. 3.1 Different subsystems of developed SJED setup 32

Fig. 3.2 Pulse condition (a) 100 kHz and (b) 500 kHz 34

Fig. 3.3 Wave images captured by DMM at (a) 3V and (b) 5V 34

Fig. 3.4 Selective jet electrodeposition (SJED) experimental setup 35

Fig. 3.5 (a) Submersible pump and (b) deposition chamber of SJED setup 35

Fig. 3.6 XYZ gantry stage (a) top and (b) front view 36

Fig. 3.7 (a) Micro position controller and (b) spindle to rotate microtool 37

Fig. 3.8 Different subprocesses for CAPP of SJED-based deposition 38

Fig. 3.9 Steps involved in separating deposited micro parts 39

Fig. 3.10 Substrate preparation for copper-based deposition (a) untreated substrate, (b) during treatment, (c) after 10 minutes of treatment, and (d) treated substrate 40

Fig. 3.11 Separation of deposited parts 40

Fig. 4.1 Process parameters of SJED process with responses 43

Fig. 4.2 Electrolyte columns formed with nozzle diameters of (a) 250 µm and (b) 500 µm; (c) Deposition process on substrate surface at 2 mm distance below nozzle, and (d) measured surface roughness of substrate surface 44

Fig. 4.3 (a) Deposited bead and 3D morphology at a particular location, and (b) 2D profilometer image at 15 V and 80 mm/min scanning speed with 500 µm nozzle diameter 46

Fig. 4.4 (a) Deposited bead and its (b) 3D morphology, (c) FESEM image at a particular location, and (d) 2D profilometer image at 10 V applied voltage and 100 mm/min scanning speed 47

TH-3378_196103004

Fig. 4.5 (a) Deposited bead and its (b) 3D morphology, (c) FESEM image at a particular location, and (d) 2D profilometer image at 15 V applied voltage and 100 mm/min scanning speed 48
Fig. 4.6 (a) Deposited bead and its (b) 3D morphology, (c) FESEM image at a particular location, and (d) 2D profilometer image at 20 V applied voltage and 100 mm/min scanning speed 48
Fig. 4.7 Initial measured value of current at (a) 10 V, (b) 15 V, (c) 20 V applied voltage; (d) Current density measured at different applied voltages 49
Fig. 4.8 Effect of (a) applied voltage and (b) scanning speed on total layer height and width 49
Fig. 4.9 Deposited 3D structures at (a) 10 V, (b) 15 V, and (c) 20 V applied voltages with 100 mm/min scanning speed..50
Fig. 4.10 (a) Deposited bead and its (b) 3D morphology, (c) FESEM image at a particular location, and (d) 2D profilometer image at 60 mm/min scanning speed for 15 V applied voltage..51
Fig. 4.11 (a) Deposited bead and its (b) 3D morphology, (c) FESEM image at a particular location, and (d) 2D profilometer image at 80 mm/min scanning speed for 15 V applied voltage..51
Fig. 4.12 Deposited 3D structures at (a) 60 and (b) 80 mm/min scanning speeds with 15V applied voltage 52
Fig. 4.13 Surface characterization (a) microhardness and (b) EDX analyses of deposited wall (Fig. 4.9(b), fabricated at 15 V applied voltage and 100 mm/min scanning speed)..53
Fig. 4.14 Variation of traction force with stroke on samples 1 and 2 during scratch test .53
Fig. 4.15 Multi-bead profile of deposits 54
Fig. 4.16 2D profilometer images with fitted curves for (a) 10 V, (b) 15 V, and (c) 20 V applied voltages and 100 mm/min scanning speed...55
Fig. 4.17 (a) Deposited multi-bead; (b) 3D and (c) 2D profile images at d = 0.7w........56
Fig. 4.18 (a) Deposited multi-bead; (b) 3D and (c) 2D profile images at d = 0.5w.........56
Fig. 4.19 (a) Deposited bead, (b) 3D profile image, and (c) 2D profile image at 100 mm/min scanning speed with 2.5 V applied voltage...59
Fig. 4.20 (a) Deposited bead, (b) 3D profile image, and (c) 2D profile image at 125 mm/min scanning speed with 2.5 V applied voltage...59
Fig. 4.21 (a) Deposited bead, (b) 3D profile image, and (c) 2D profile image at 150 mm/min scanning speed with 2.5 V applied voltage...59

TH-3378_196103004

Fig. 4.22 (a) Deposited bead, (b) 3D profile image, and (c) 2D profile image at 100 mm/min scanning speed with 5 V applied voltage....60
Fig. 4.23 (a) Deposited bead, (b) 3D profile image, and (c) 2D profile image at 125 mm/min scanning speed with 5 V applied voltage....60
Fig. 4.24 (a) Deposited bead, (b) 3D profile image, and (c) 2D profile image at 150 mm/min scanning speed with 5 V applied voltage....61
Fig. 4.25 Variation of total bead height with scanning speed at 2.5 V and 5 V....61
Fig. 4.26 (a) Deposited bead, (b) 3D profile image, and (c) 2D profile image at 100 mm/min scanning speed with 7.5 V applied voltage....62
Fig. 4.27 (a) Deposited bead, (b) 3D profile image, and (c) 2D profile image at 125 mm/min scanning speed with 7.5 V applied voltage....62
Fig. 4.28 (a) Deposited bead, (b) 3D profile image, and (c) 2D profile image at 150 mm/min scanning speed with 7.5 V applied voltage....62
Fig. 4.29 (a) Deposited multi-beads, (b) 3D profile image, and (c) 2D profile image at d = 0.5w....64
Fig. 4.30 (a) Deposited multi-beads, (b) 3D profile image, and (c) 2D profile image at d = 0.65w....64
Fig. 4.31 (a) Deposited multi-beads, (b) 3D profile image, and (c) 2D profile image at d = 0.75w....64
Fig. 4.32 (a) Deposited multi-beads, (b) 3D profile image, and (c) 2D profile image at d = 0.47w....65
Fig. 4.33 (a) Deposited multi-beads, (b) 3D profile image, and (c) 2D profile image at d = 0.45w....65
Fig. 4.34 (a) Deposited multi-beads, (b) 3D profile image, and (c) 2D profile image at d = 0.4w....65
Fig. 4.35 Tool paths with (a) TSP horizontal biased (84 turns), (b) TSP with circular grid (137 turns), and (c) TSP with no biased (150 turns)....66
Fig. 4.36 (a) Deposited structure with TSP horizontal biased toolpath, (b) 3D profilometer image, and surface roughness at considered points in (c) Direction-1 and (d) Direction-2....67
Fig. 4.37 (a) Deposited structure with TSP circular grid toolpath, (b) 3D profilometer image, and surface roughness at considered points in (c) Direction-1 and (d) Direction-2....68

TH-3378_196103004

Fig. 4.38 (a) Deposited structure with TSP with no biased toolpath, (b) 3D profilometer image, and surface roughness at considered points in (c) Direction-1 and (d) Direction-2 69
Fig. 4.39 Surface roughness values corresponding to different tool paths 69
Fig. 4.40 (a) Surface morphology, (b) variation of traction force with stroke, (c) EDX analysis, and (d) microhardness of deposited bead 70
Fig. 5.1 (a) Fabricated circuit by SJED after separating from substrate and its (b) 3D morphology and (c) 2D profilometer image at a particular location 73
Fig. 5.2 (a) Test setup for case study and (b) its extended view 73
Fig. 5.3 (a) Density based gradient tool path using TSP, (b) deposited structure, and its (c) macroscopic image after separation from substrate; (d) 3D profilometer image at a particular location, and (e) 2D profilometer images along lines AB & CD 74
Fig. 5.4 (a) Density based gradient tool path using TSP, (b) deposited structure, (c) macroscopic image of the density-based disk, and (d) 3D surface profiles at several points marked in (b) 75
Fig. 5.5 (a) Density-based gradient tool path using TSP, (b) deposited structure, and (c) macroscopic image of deposited rabbit 76
Fig. 5.6 (a) Gradient-based TSP tool path, (b) deposited 3D structure of pawn, and its (c) macroscopic image; (d) Separation of 3D parts by bending substrate, and (e) separated 3D component 77
Fig. 5.7 Schematic diagram of conventional electroplating setup 78
Fig. 5.8 (a) Coating by conventional method and (b) macroscopic image of coating 78
Fig. 5.9 Raster tool path for coating by SJED technique 79
Fig. 5.10 (a) Coating by SJED method and (b) macroscopic image of coating 79
Fig. 5.11 FESEM images of coating by (a) conventional and (b) SJED methods 80
Fig. 5.12 (a) 3D and (b) 2D profilometer images of coating by conventional method 81
Fig. 5.13 (a) 3D and (b) 2D profilometer images of coating by SJED method 81
Fig. 5.14 Traction force Vs. stroke length plots for SJED and conventional coatings 82
Fig. 5.15 Microhardness indentation of coatings fabricated by (a) conventional and (b) SJED methods 83

Fig. A1.1 Method of electrodeposition by (a) conventional and (b) SJED processes 89
Fig. A1.2 Experimental setup of SJED process 91

TH-3378_196103004

Fig. A1.3 Combined effect of (a) scanning speed and applied voltage, (b) frequency and applied voltage, and (c) frequency and scanning speed on layer height............................96
Fig. A1.4 Combined effect of (a) scanning speed and applied voltage, (b) frequency and applied voltage, and (c) frequency and scanning speed on layer width............................97
Fig. A1.5 (a) Deposited bead, (b) 3D and (c) 2D profile images of deposited bead at 3.54 V applied voltage, 297 kHz frequency of current, and 80 mm/min scanning speed.......100
Fig. A1.6 (a) Deposited multi-bead, (b) 3D and (c) 2D profile images at d= 0.55w 101
Fig. A1.7 (a) Deposited multi-bead, (b) 3D and (c) 2D profile images at d= 0.50w 101
Fig. A1.8 (a) Deposited multi-bead, (b) 3D and (c) 2D profile images at d= 0.45w 101

Fig. A2.1 Localized electrochemical deposition (LED) experimental setup and input & output process variables...106
Fig. A2.2 Cross-sectional view of LED tool CAD model..107
Fig. A2.3 Effect of (a) applied voltage, (b) inter-electrode gap, (c) frequency, and (d) scanning speed on layer height and width 112
Fig. A2.4 (a) Optical microscopic image of deposited single layer at 5V applied voltage, 100 kHz frequency, 10 μm IEG, and 1 μm/s scanning speed; (b) 3D and (c) 2D optical profilometer images of deposited single layer...113
Fig. A2.5 Combined effect of (a) IEG and applied voltage, (b) frequency and applied voltage, (c) frequency and IEG, (d) scanning speed and IEG, (e) scanning speed and frequency, and (f) scanning speed and applied voltage on layer height.........................115
Fig. A2.6 Combined effect of (a) applied voltage and IEG, (b) IEG and scanning speed, (c) IEG and frequency, (d) applied voltage and frequency, (e) applied voltage and scanning speed, and (f) frequency and scanning speed on layer width 117
Fig. A2.7 Optimization graph of Layer height and width 118
Fig. A2.8 Optical microscopy and 3D optical profilometer images of deposited (a) single and (b) double layers; Layer height measurement from 2D profilometer images of (c) single and (d) double layers..119
Fig. A2.9 A 3D circular ring deposited over a brass substrate at optimum process parameter condition 121
Fig. A2.10 Surface characterization of deposited 3D circular ring through (a) field emission scanning electron microscopy (FESEM) and (b) energy dispersive X-ray (EDX) analysis 121

TH-3378_196103004

List of Tables

Table 2.1 Development of LECD process considering various aspects 14

Table 2.2 Development of the SJED considering several aspects 19

Table 2.3 List of target materials with electrolyte solution and additive agents in SJED25

Table 4.1 Electrolyte bath composition...42

Table 4.2 Process parameters and their ranges 43

Table 4.3 Process parameters and their ranges 57

Table A1.1 Process variables and their levels..92

Table A1.2 Statistical design of experiments with corresponding responses 92

Table A1.3 ANOVA for layer height..94

Table A1.4 ANOVA for layer width...94

Table A1.5 Optimization study and range of input process parameters with weightage..98

Table A1.6 Validation of predicted results from DOE with experimental results............99

Table A2.1 Process parameters and their levels..108

Table A2.2 Statistical design of experiments with responses 108

Table A2.3 ANOVA for layer height...112

Table A2.4 ANOVA for layer width..113

Table A2.5 Optimization study and range of input process parameters with weightage 118

Table A2.6 Validation of predicted results from DOE model with experiments............120

TH-3378_196103004

NOMENCLATURES

V	Applied voltage (V)
R_a	Average surface roughness
d	Center distance
h_c	Cup height
Z	Electrochemical equivalent constant
f	Frequency
F	Faraday's constant of electrolysis (C/mol)
h	Layer height (µm)
w	Layer width (µm)
S_S	Scanning speed (mm/min)
h_v	Valley height

Acronyms

AM	Additive manufacturing
ANOVA	Analysis of variance
H_3BO_3	Boric acid
CNC	Computer numerical control
$CuSO_4$	Copper sulfate
DI	Deionized water
DOE	Design of experiment
DMM	Digital multimeter
ECM	Electrochemical Machining
EDS	Energy-Dispersive X-Ray Spectroscopy
EMM	Electrochemical Micromachining
ECD	Electrochemical deposition
FEA	Finite element analysis
FESEM	Field emission scanning electron microscope
FFF	Fused filament fabrication
FOM	Flat-top overlapping model
HCl	Hydrochloric acid
H_2SO_4	Sulfuric acid

TH-3378_196103004

IEG	Interelectrode Gap
LECD	Localized electrochemical deposition
$NiCl_2.6H_2O$	Nickel chloride
$Ni.SO_4$	Nickel sulfate
PBF	Powder bed fusion
RSM	Response surface methodology
SiC	Silicon carbide
SJED	Selective jet electrodeposition

TH-3378_196103004

Chapter 1 Introduction

Additive Manufacturing (AM) has revolutionized traditional manufacturing processes by introducing a generative approach. In contrast to subtractive manufacturing, where the material is removed from a workpiece to achieve the desired shape, AM involves selectively and strategically adding material layer by layer to create the final component. Initially developed for rapid prototyping, AM has evolved into a comprehensive manufacturing process capable of series production for functional components [1], [2]. ASTM (American Society for Testing and Materials) categorizes AM techniques into seven categories. However, these categories serve as broad terms, encompassing multiple variants of each technique. AM includes diverse methods, each tailored to specific applications and material requirements. The AM process sequence can be broadly divided into three main phases: pre-processing, processing, and post-processing, as depicted in Fig. 1.1. Each phase plays a crucial role in ensuring the successful and efficient production of components through AM.

Additive Manufacturing (AM) involves pre-processing, where a CAD model is tessellated and sliced. Contour information and toolpaths are extracted. Processing follows, fabricating the part layer by layer using the chosen AM technique. Post-processing enhances surface and mechanical properties. AM extends to part repair, surface coating, micro-manufacturing, and fabricating functionally graded materials (FGMs).

Each AM process is tailored to specific requirements, and for the micro-manufacturing of metallic parts, powder bed fusion (PBF) and selective jet-based electrodeposition prove to be valuable techniques. However, it's important to note that PBF has several limitations, including powder size, temperature gradient, and residual stress stemming from temperature gradient variations. Therefore, the focus of this study revolves around the selective jet-based electrodeposition technique, recognized for its atom-by-atom deposition process conducted at room temperature. This method stands out as a prominent and optimal choice in micro-manufacturing. Regarding the historical development of 3D micromanufacturing from electrodeposition, its roots are commonly traced back to the study of Hunter et al. [3]. However, constructing structures in the form of coating exclusively from electrolytes through various electrodeposition processes has much earlier origins [4].

TH-3378_196103004

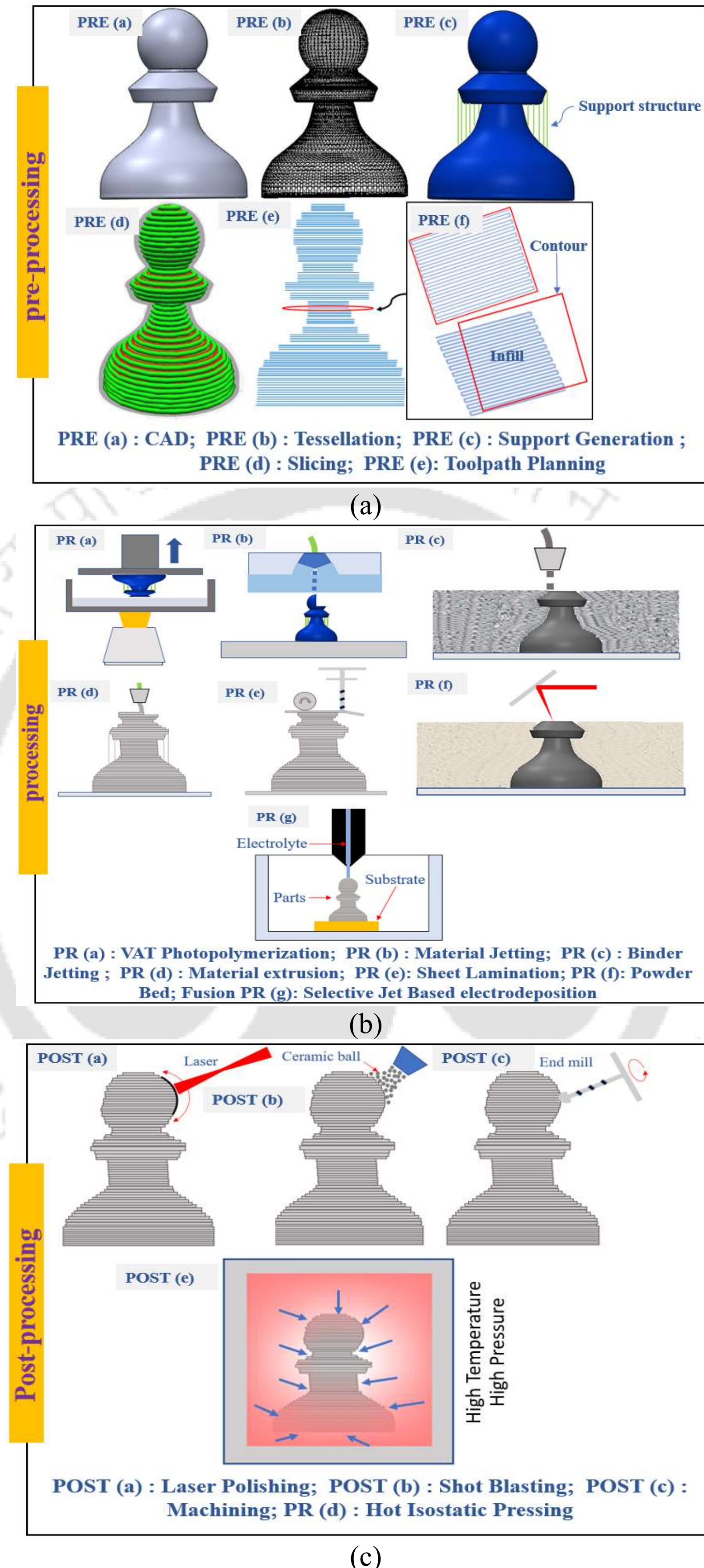

Fig. 1.1 (a) Process sequence for additive manufacturing with pre-processing, (b) AM Classification, and (c) few post-processing techniques for quality improvement of AM parts

The enhancement of any technology necessitates a comprehensive understanding of its constituent subsystems. Improving the efficiency of each of these subsystems directly correlates with an overall boost in the efficiency of the entire technology. AM serves as an excellent illustration of this concept. Although conceptualized in the 1960s [5], AM has experienced significant growth only in the current decade. A contributing factor to this delayed advancement is the absence of supporting peripherals that form the framework for this technology.

The essential supporting technologies, called peripherals, encompass high-performance computing, enhanced CAD handling software, and improved economic electronics [6]. While the ideas and insights presented in the literature review specifically relate to selective jet electrodeposition (SJED), it is noteworthy that they can be extrapolated to other AM technologies.

1.1 Electrochemical deposition-based micro additive manufacturing

The fundamental support for various high-tech micro-sized products, such as electronic packaging components, precision machinery, miniature aerospace devices, and microelectromechanical systems (MEMS), often lies in the precision metal microstructure and micro-components that enable and drive their functionality. As a result, the cost-effective production of these metal micro-geometries has been the subject of extensive research over the last few years. Various metal microfabrication techniques have been developed, encompassing mechanical micromachining techniques such as micro-milling, micro-turning, and micro-drilling [7]. Additionally, high-energy beam methods like laser beam, electron beam, and ion beam micromachining have been explored [8], [9]. Further, micro-electrical discharge micromachining (micro-EDM) [10] and micro-electrochemical machining (micro-ECM) [11] are among the established techniques in this field. Nonetheless, these micromachining techniques generate micro-geometries through subtractive manufacturing processes, imposing significant limitations on material selection and achievable complex geometric shapes. For instance, fabricating difficult-to-machine materials at the micrometer and nanometer scales using mechanical machining methods proves exceptionally difficult. High-energy beam-driven processes, while effective, frequently result in defects such as recast layers, micro-cracks, micro-voids, and distortions in the machined micro-components. Additive micro-manufacturing (micro-AM) represents an alternative approach, creating micro-geometries

TH-3378_196103004

through the layer-by-layer joining of deposited materials. This method offers exceptional free-forming and rapid prototyping capabilities, effectively mitigating the constraints associated with subtractive manufacturing techniques, as mentioned earlier.

The predominant micro-AM techniques in use are typically propelled by high-energy beams, including electron/laser beam selective melting and sintering (direct energy deposition (DED) and Powder bed fusion (PBF)). However, it has been demonstrated that micro-geometries produced by high-energy beam-driven micro-AM methods often exhibit significant thermal and stress-induced distortions in shape and a considerable presence of voids and crack defects, rendering them unacceptable. This is primarily attributed to the fact that the formation of these micro-geometries necessitates rapid and drastic temperature changes, along with rapid phase transitions occurring within a concise timeframe. Hence, thermally-driven micro-AM techniques prove insufficient for achieving high-quality metal micro-geometries. Therefore, non-thermal or alternative approaches are sought for this purpose.

Electrochemical deposition (ECD) is a low-temperature material deposition process where metal-based coatings and components are meticulously formed atom-by-atom within a low or moderate-temperature aqueous electrolyte environment (typically below 70°C) [12]. This method facilitates the production of precision micro-geometries characterized by notably low internal stress and minimal internal defects, such as voids and cracks. Electrochemical Deposition (ECD) can be categorized into two main types: mask-based ECD and maskless ECD, depending on whether a through mask is employed in the process.

Micro-metal electrochemical additive manufacturing (micro-MEAM) is an unconventional fabrication method that utilizes the electrochemical deposition (ECD) mechanism in a specific form to additively manufacture metal geometries at a dimensional scale below the micrometer level. Micro-MEAM based on the traditional mask-based Electrochemical Deposition has been extensively adopted for manufacturing two-dimensional (2D) and quasi-three-dimensional (quasi-3D or 2.5D) large-scale precision micro-sized metallic geometries. This process involves the inverse duplication of photoresist through-masks that are patterned lithographically. Recently, micro-MEAM has garnered increasing attention for its notable potential advantages in manufacturing intricate three-dimensional (3D) precision micro-geometries that are void-free, crack-free, and boast an excellent surface finish. Furthermore, it has become more advanced in the form of Micro-Additive Manufacturing (micro-AM) without using through-masks. The mask-based micro-MEAM holds a distinct advantage in manufacturing high-accuracy and high-surface-quality two-dimensional (2D) micro-geometries.

TH-3378_196103004

Conversely, maskless micro-MEAM demonstrates significant competitiveness in producing freeform micro- and nanoscale geometries characterized by minimal micro-voids and micro-crack defects. Typical micro-MEAM techniques mainly encompass through-mask electroplating like the LIGA process, instant masking (IM) plating, electrochemical fabrication (EFAB), localized electrodeposition (LECD), and selective jet electrodeposition (SJED), as shown in Fig. 1.2. Localized electrodeposition is a micro AM process used to fabricate the metallic parts in an atom-by-atom manner. Since the process occurs at room temperature, negligible residual stress is produced in the printed parts. The resolution of the deposited parts is high because of the atomic level deposition.

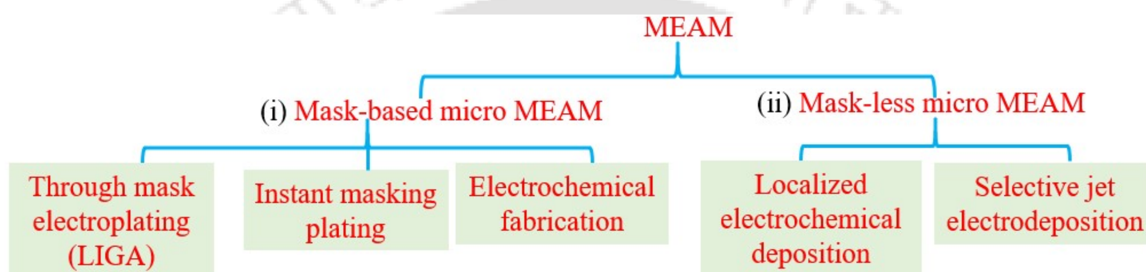

Fig. 1.2 Flow chart of micro-manufacturing process based on material removal

1.1.1 Mask-based micro MEAM

In the mask-based electrochemical deposition (ECD) process, an electrically insulating photoresist through-mask is essential to unveil and define the regions where deposition is intended. In simpler terms, mask-based ECD can be seen as a metal duplication process. In this process, metal features and components are obtained by replicating the shape of the pattern through a mask. This is achieved by reversely electrochemically filling metal material into the photoresist molds, resulting in the desired metal structures.

1.1.1.1 Through-mask electroplating (LIGA)

Li et al. [13] reviewed a mask-based hybrid electrodeposition process called LIGA to fabricate micro-geometries with ultrahigh aspect ratios. LIGA is an acronym derived from the German terms Lithografie (i.e., lithography), Galvanoformung (i.e., electroforming), and Abformung (i.e., molding). In this context, electroforming refers to the through-mask electroplating. The crucial step in the LIGA process is that it necessitates specially prepared ultrahigh aspect ratio (HAR) through-masks. Unlike conventional photoresist through-masks, typically prepared with an ultraviolet light source, the through-masks used in the electroforming step of LIGA are

TH-3378_196103004

crafted from ultra-thick polymethyl methacrylate (PMMA) photoresist, with a thickness of several millimeters. These specialized through-masks are produced using an ultra-high-energy X-ray synchrotron radiation source, significantly raising the overall cost of the LIGA process. Additionally, these processes entail the utilization of hazardous chemicals for etching the masks, thereby increasing the overall complexity and posing potential environmental risks associated with the manufacturing process.

1.1.1.2 Instant masking plating

Unlike through-mask electroplating, where the through-mask is fixed to the cathode during electrodeposition, instant masking (IM) plating, as introduced by Cohen et al. [13], is a process in which the through-mask is affixed to the anode. The schematic diagram of this process is illustrated in Fig. 1.3. In IM plating, electrodeposition occurs exclusively when the through-mask (instant mask) is closely attached to the cathodic substrate. To maintain a relatively favorable electrochemical reaction environment, the anode must be periodically lifted from the cathode and synchronized with a power-off operation. This allows for the electrolyte's renewal and the electrolytic products' removal. Compared to through-mask electroplating, IM plating is more straightforward and more cost-effective because the through-mask is reused, eliminating the need for repeated preparations of through-masks.

In theory, micro-MEAM based on IM plating offers flexible manufacturing capabilities, as the anode tool with the reusable through mask can be moved freely. However, it faces at least two inherent drawbacks that need resolution before widespread acceptance. First, achieving consistent and precise alignment of the anode-mask assembly with previously formed structures is challenging, potentially leading to interruptions in the electrodeposition process. Another drawback is that the deposition rate must be minimal due to the significantly reduced current density allowed in a nearly closed reaction space formed by the closely approached through-mask and cathode. Additionally, the need for numerous non-deposition intervals to repeatedly lift the anode contributes to the low efficiency of IM plating.

TH-3378_196103004

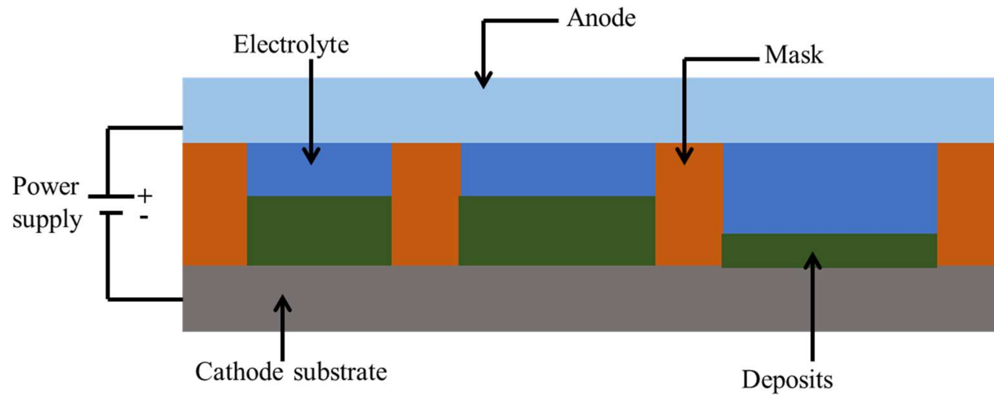

Fig. 1.3 Instant masking (IM) plating process

1.1.1.3 Electrochemical fabrication

Electrochemical fabrication (EFAB) was proposed by Cohen et al. [14], [15], representing the combination and repetition of three primary operating steps. The main operating steps in EFAB involve the pattern deposition of the structural metal, planarization, and blanket deposition of the sacrificial metal. This hybrid technique initiates the deposition of the first layer of the sacrificial metal on a blank substrate, followed by the deposition of the first layer of the structural metal. In EFAB, the operational steps involve: (1) depositing a base metal layer (i.e., structural or sacrificial) on a cathode substrate using IM plating; (2) adding a new metal layer on the existing one, with the type depending on the first layer (sacrificial or structural); (3) planarizing both layers to the same level using processes like micro-milling or precision grinding; (4) repeating these steps until the desired number of structural layers is achieved; (5) removing sacrificial layers to form the final solid geometry. In theory, EFAB can fabricate micro-geometries of arbitrary shapes. Cohen et al. [16] demonstrated the favorable manufacturing capacities of EFAB by successfully producing various high-accuracy metallic medical instruments, including tissue approximation clips, reciprocating tools, tissue saws, tissue approximation devices, and hydraulically operated forceps.

While EFAB offers advantages, challenges also persist. Micro-stepped surfaces can form due to difficulties in accurately aligning metal layers, complicating post-treatment. Delamination issues arise from weak inter-layer adhesion, intensified by intermittent deposition and planarization, forming oxidation layers. Additionally, the differing materials of sacrificial and structural layers pose challenges for inter-layer bonding. Addressing these concerns can enhance EFAB's efficacy.

1.1.2 Mask-less micro MEAM

TH-3378_196103004

Maskless electrochemical deposition is conducted without a through mask on the cathode. As a result, the limitation of mass transportation is not a highly concerning issue. Some mask-less micro MEAM processes are discussed below.

1.1.2.1 Localized electrochemical deposition

The localized electrochemical deposition (LECD) process is a typical mask-less micro-MEAM, as initially reported by Madden and Hunter in 1995 [3]. This technique employs an ultrafine inert anode tip to generate a highly localized electric field, inducing electrodeposition at the cathode and enabling the additive formation of microscale and nanoscale 3D features, as schematically shown in Fig. 1.4. In LECD, both the anode and cathode are submerged in the electrolyte with a constant small interelectrode gap (IEG) (generally 5–100 μm). The anode is precisely moved spatially with respect to the cathode surface (i.e., deposited metal) following pre-designed paths. Simultaneously, metal electrodeposition takes place in a localized area directly beneath the anode tip, resulting in the formation of 3D microstructures. The attainable minimum dimension in LECD is strongly influenced by the degree of localization during the electrodeposition process, primarily determined by the geometrical shape, size, and spatial movement of the anode tip, as well as the size of the interelectrode gap (IEG).

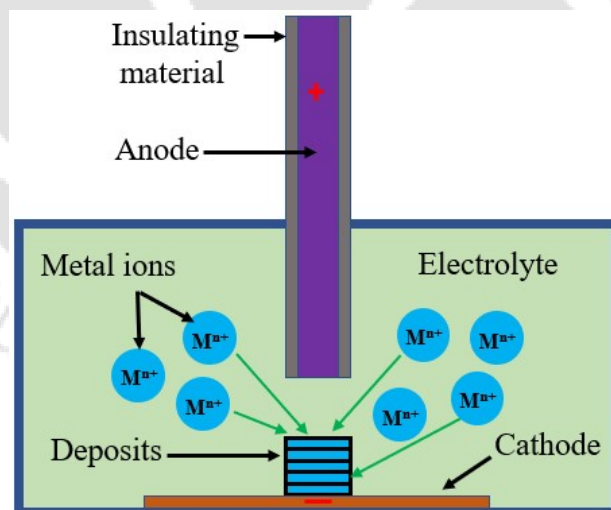

Fig. 1.4 Schematic diagram of localized electrochemical deposition

LECD has demonstrated its ability to create unique micro-sized features, as various researchers have shown. Jansson et al. [17] fabricated an ultra-high aspect ratio (AR up to 200) ultrafine nickel micro-column (height: 600 μm, diameter: 3 μm). Seol et al. [18] achieved a complex 3D polypyrene microstructure using LECD. LECD has demonstrated its effectiveness

TH-3378_196103004

in manufacturing complex 3D micro-scaled solid geometries, typically constructed using circular-section freestanding wires. Nevertheless, the fabrication of complex 3D features with noncircular cross-sectional profiles still presents several challenges. Additionally, because LECD employs static electrolytes during deposition, there is an ion deficiency between the tool and substrate. The vigorous generation of bubbles during deposition further contributes to nonuniform deposition.

1.1.2.2 Selective jet electrodeposition

Selective Jet Electrodeposition (SJED), introduced by Zimmerman [19], is another notable mask-less micro-MEAM process. In contrast to LECD, SJED utilizes an impinging anodic electrolyte jet, instead of a solid ultrafine anode, as its anode tool to selectively deposit metal at the cathode. SJED is characterized by a significantly high deposition rate, reaching up to 1 mm/h. This is achieved by employing considerably high current densities (typically several hundred A/dm^2), which result from using a high-speed electrolyte jet ejected from a nozzle connected to the positive pole of the power supply and applied to the cathode. Therefore, SJED also called the Jet ECD, is consistently regarded as a high-speed ECAM process. Its schematic diagram is illustrated in Fig. 1.5.

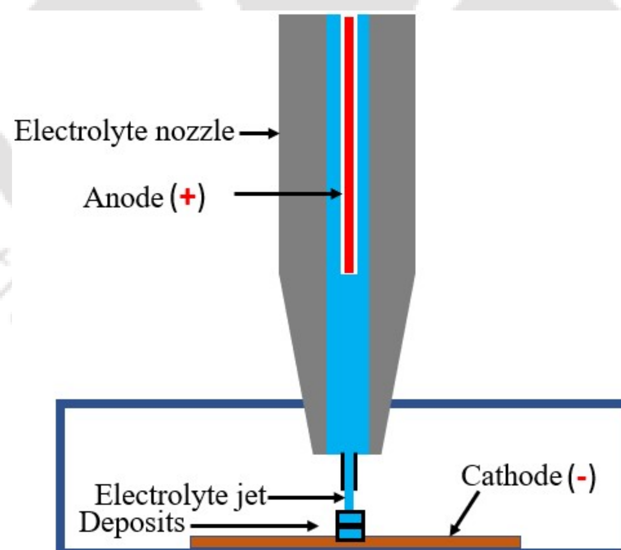

Fig. 1.5 Schematic diagram of selective jet electrodeposition process

During SJED, highly localized deposition can be maintained at the cathode due to a significantly large electrolyte velocity difference between the jet-impinging area and other areas (i.e., around the jet-impinging area) on the cathode [20], [21]. In theory, compared to other maskless micro-MEAM processes, SJED demonstrates more significant potential in

TH-3378_196103004

additive manufacturing of freeform solid micro-geometries because the anode can be moved more freely and quickly at a considerably larger distance (several millimeters to several centimeters) from the cathode.

1.2 Motivation for present work

Micro-fabrication is crucial for the discussed fabrication processes, which demand economical, efficient, and environment-friendly methods. While thermal-based micromanufacturing processes (i.e., PBF, DED, etc.) exist, they generally result in nonuniform deposition, high internal stress, and poor aspect ratios due to powder size, laser beam size, and thermal gradients on the deposited surface. Therefore, non-thermal processes are sought to fabricate products that are uniform and have a high aspect ratio.

ECD-based additive manufacturing processes offer viable alternatives for fabricating miniature components. Various ECD-based micromanufacturing processes, categorized into mask-based and mask-less processes, are available. Mask-based processes, including LIGA, Instant masking, and EFAB, can produce complex features with high aspect ratios. However, these processes are often costly due to the requirement of masks and etching. Also, the used chemicals are not environmentally friendly.

Mask-less electrochemical deposition (ECD) based additive manufacturing techniques provide another alternative that eliminates the need for a mask. This approach showcases its capabilities in micromanufacturing in terms of cost-effectiveness and eco-friendliness. The primary objective of this project is to address the challenges of true 3D microparts fabrication by utilizing maskless ECD with the help of toolpath strategy that facilitates close-loop continuous deposition with a minimal number of turns. Single and multi-bead optimization is tested for defect and void-free fabrication. As a part of this work, an indigenously developed SJED platform was utilized to test the viability of the proposed method and toolpath strategy.

1.3 Objectives of present thesis

The proposed research in the present thesis uses a mask-less electrochemical deposition (ECD) process to fabricate surface microfeatures. The key objectives of the present study are outlined as follows:

- Design and development of an experimental setup for the selective jet electrodeposition (SJED) process, which includes subcomponents like a mechanical controller, power supply, tool positioning unit, nozzle unit, and machining chamber.

TH-3378_196103004

- To optimize the input process parameters for optimal productivity and dimensional accuracy of the components.
- Utilization of the developed setup to deposit various materials like Ni and Cu, conducting a thorough parametric study to understand the effects of different factors on the deposition process.
- Toolpath planning for area filling using continuous and closed-loop deposition through traveling salesman problem (TSP) based toolpath.
- To develop a method for separating the deposited parts, especially nickel and copper from the substrate.
- Surface integrity analysis includes surface roughness, surface morphology, surface profile, and tribological properties on products fabricated by the SJED process.
- To study applications such as coating and microfabrication using the developed method.

1.4 Organization of thesis

The present thesis is organized into six chapters, including an appendix with references. The steps involved in additive manufacturing are discussed in **Chapter 1**. The introduction to the various metallic micro-additive manufacturing processes based on the electrodeposition principle is discussed in this chapter. The mask-based and maskless electrodeposition-based micro-additive manufacturing processes are discussed in detail. Further, the motivation behind the present research is discussed while comparing the other micro-depositions along with their limitations.

The literature review of different maskless micro-additive manufacturing processes for complex fabrication is thoroughly presented in **Chapter 2.** Also, two maskless micro-additive manufacturing processes, namely localized electrodeposition (LED) and selective electrodeposition (SJED), are discussed along with their mechanism of working principle. Also, the literature survey related to different metallic deposition processes with their experimental setup and material deposition modeling are discussed.

In **Chapter 3**, the design and development of an experimental setup for SJED-based electrodeposition process for the fabrication of 3D parts is discussed. Computer-aided process planning (CAPP) for the deposition of nickel and copper and further separation of the substrate from both deposited materials are discussed.

In **Chapter 4,** an experimental study corresponding to nickel and copper depositions is conducted for single and multi-bead deposition. Further, the deposited materials are characterized

TH-3378_196103004

on both single and multi-bead depositions for both metals. Further, the multi-bead analysis for generating the flatter surface condition is performed experimentally by varying the center distance between the adjacent beads. Multi-bead analysis is essential for obtaining uniform and void-free deposited surfaces. Furthermore, a toolpath analysis is also performed to determine the effect of the number of turns on the tool path on surface quality.

Chapter 5 discusses several applications of the developed SJED process by fabricating different microparts with the help of the developed toolpath strategies. The deposited materials with nickel and copper show the ability of the SJED process to manufacture microparts. Furthermore, the application of SJED in fabricating thick coating is also discussed and compared with the conventional coating method.

Discussion about the conclusions and critical findings of the present study with the future scope is presented in **Chapter 6**.

Appendix 1 discusses the parametric investigation of the developed setup which is performed with the help of response surface methodology.

Appendix 2 discusses the development of the localized electrochemical deposition setup. Parametric investigation to find the optimized input parameters is performed for the deposition of nickel. Feasibility test by depositing a circular ring is performed with the help of the developed setup.

TH-3378_196103004

Chapter 2 Literature survey

2.1 Introduction

This section undertakes a comprehensive literature review of mask-less micro-MEAM processes, primarily focusing on the development of experimental setup, micro-manufacturing, process parameters, and applications intending to address challenges in micro-manufacturing. The present section discusses two maskless processes: localized electrochemical deposition (LECD) and selective jet electrodeposition (SJED). This section is further divided into several sub-sections. In subsection 2.1.1, a detailed study is performed to develop the experimental setup of LECD. The components and their resolution, suitable for micromanufacturing, have been presented. Subsection 2.1.2 includes thorough research about the significant process parameters to achieve the required precision in the LECD process. Subsection 2.1.3 presents a detailed study of the various processes for the microfabrication of components. In subsection 2.1.4, a summary of the literature on LECD is presented.

In subsection 2.1.5, a detailed study is performed to develop the experimental setup of SJED. In subsection 2.1.6, the principle of electrodeposition by the SJED process is presented. In subsection 2.1.7, a detailed study of the kinetics of the micro-deposition for SJED is discussed. In subsections 2.1.8, the influence of the process parameters is presented. In section 2.1.9, microfabrication by utilizing the SJED process is discussed. Section 2.1.10 discusses the characteristics of the as-deposited microparts by SJED are discussed. In section 2.1.11, the applications and current problems & challenges of SJED have been presented.

2.1.1 Development of LECD experimental setup

Considering the importance of LECD, researchers from various research laboratories, research institutes, and universities previously attempted to develop the LECD setup, considering several aspects of the process, as shown in Table 2.1. The LECD experimental setup must fulfill individuals' requirements while performing experiments to understand the process better. With the wide application of this process in various fields in recent years, there is an urgent need for a commercial LECD setup suitable for fabricating microfeatures. Progress in developing experimental setups has been reviewed in detail in this section.

TH-3378_196103004

Hunter et al. [3] developed the first LECD experimental setup to fabricate a microstructure to understand its feasibility. The developed LECD setup mainly consisted of several components: a mechanical machining unit, an electrolyte flow system, a power supply, and a control unit. All these sub-components were integrated so that the developed experimental setup could perform fundamental research in LECD, fulfilling the requirements of micromanufacturing objectives like the precise movement of axes, power supply, etc. Several experiments were also conducted at different process parameter conditions to understand the capabilities of the developed setup.

Table 2.1 Development of LECD process considering various aspects

Type	Research aspect	Development trends of LECD
Theoretical development	Setup development	Said [22], 2003; Said [23], 2003; Brant et al. [24], 2015; Kamraj et al. [25], 2018; Volgin et al. [26], 2018
Process condition optimization	Process parameter optimization	Muller et al. [27], 2000; Lin et al. [28], 2008; Wang et al. [29], 2019; Yeo et al. [30], 2000; Said [31],2004; Lin et al. [32], 2010
	Development of control methods	Seol et al. [33], 2005; Ciou et al. [34], 2016; Lin et al. [35], 2005; Chen et al. [36], 2005
Modified LECD process	Applied rotating anode tip	Yeo et al. [37], 2001
	Applied ultrasonic vibration	Yeo et al. [38], 2002
	Picosecond laser-assisted	Wu et al. [39], 2021
Potential application development	Micromachine	Madden et al. [3], 1996
	Microelectronics	Giar et al. [40], 2000
	Medical field	Yeo et al. [37], 2001
	Sensor	Lin et al. [28], 2008; Tseng et al. [41], 2014
	Microelectrode	Habib et al. [42], 2009; Habib et al. [43], 2016

Kamraj et al. [25] developed an LECD setup consisting of a pulse power supply unit. The authors performed preliminary experiments to ensure the feasibility of the developed setup and investigated the influence of deposition parameters on deposition accuracy. The manufacturing process involves creating three-dimensional free-hanging structures, each with a height and overhang of approximately 600 µm, to demonstrate and establish the capability of the process.

Said [44] developed an LECD setup to find the effect of tool withdrawal speed on the deposition quality. The impact of the relative velocities between the tip and deposit surface is examined through experimental investigations into deposit characteristics. Three distinct

TH-3378_196103004

cases are considered: when the tip withdrawal is slower than, roughly equal to, and faster than the deposition rate. Optimal outcomes are achieved when the tip withdrawal rate is approximately equal to the deposition rate.

Habib et al. [43] developed an LECD experimental setup; their study introduces an innovative method for manufacturing electrodes with intricate cross-sections, utilizing a mask made of non-conductive material. The process involves placing the mask between the anode and cathode, both submerged in a mixed electrolyte comprising copper sulfate, 1.0M sulfuric acid, and an additive agent (i.e., thiourea at a concentration of 0.04 g/l). Copper deposition occurs selectively on the cathode surface by employing ultra-short voltage pulses between the anode and cathode. Notably, the cathode is positioned above the anode with a mask, allowing the deposited electrode to be directly utilized for electrical discharge machining (EDM) or other applications without changing tool orientation.

Daryadel et al. [45], based on their developed LECD experimental setup, reported that the microstructure of metals printed using the microscale localized pulsed electrodeposition (L-PED) process can be controlled in situ during 3D printing. Specifically, the authors demonstrated that by adjusting electrochemical process parameters, the density and orientation of twin boundaries (TBs) can be controlled along with the grain size. The outcomes of in situ scanning electron microscopy (SEM) micro compression experiments on directly 3D-printed micro-pillars reveal that such control over the microstructure directly correlates with the mechanical properties of the printed metal.

2.1.2 Influence of significant process parameters in LECD

A fishbone diagram illustrating the major process parameters of LECD is depicted in Fig. 2.1. Also referred to as the Ishikawa diagram or cause and effect diagram, it highlights the influential LECD process parameters. The following process parameters must be optimally controlled to achieve effective and high-precision fabrication in the micron range,.

- Tool and workpieces like shape, size, surface quality, tool coatings, tool feed rate, surface finish, etc., play a significant role in the surface finish of final fabricated components.
- Electrolyte parameters such as type of electrolyte, its concentration, temperature, flow rate, etc., ensure the electrical circuit's continuation.

TH-3378_196103004

- Electrical parameters such as power supply (continuous or pulse), duty cycle, and frequency provide sufficient potential for anodic dissolution. It also helps to increase the deposition accuracy.
- Mechanical capabilities of the machining setup, such as resolution, rigidity, and the interelectrode gap between the tool and workpiece, help in deposition at the micron level. The CNC machine bed, with a resolution of 0.1 µm in all three axes, provides precise movement of the electrodes.

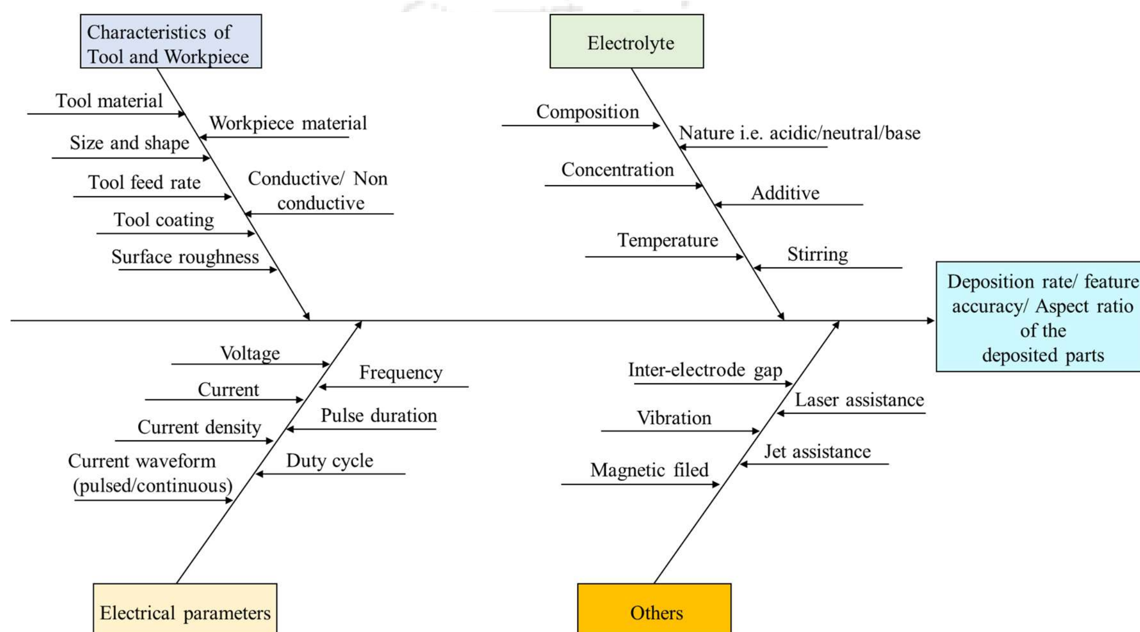

Fig. 2.1 Major process parameters in LECD process

Wang et al. [46] investigated the effect of voltage on the deposition. A change in voltage during experimentation results in varying surface and cross-section morphologies. At 2.4 V, copper pillars exhibited a cylindrical shape with a regular circumference and minimal voids. Increasing the voltage to 2.6 V led to tumor-like deposition, while at 2.8 V, a bifurcate phenomenon with irregular cross-sections and voids occurred. At 3.0 V, copper pillars tend to form dendriform shapes with cross-sections filled with voids and cracks.

Sundaram et al. [47] investigated the effect of inter-electrode gap. They found that the interelectrode gap significantly influences the deposition outcome. A smaller gap leads to the formation of an ion depletion region, causing a potential short circuit. In comparison, a larger gap may result in insufficient current density for effective metal ion migration, causing localized deposition failure.

TH-3378_196103004

Lin et al. [32] aimed for a smooth column surface, uniform cross-section diameter, and compact structure in deposition experiments using pulsed voltages and currents. They found that the duty cycle significantly affects deposition quality by providing sufficient time for metal ions to replenish, ensuring a balance between supply and demand. Increased voltage and duty cycle values led to a significant deterioration in the surface quality of the deposits.

Said [44] experimentally found that the optimal deposition quality was achieved when the tip lift speed was equal to the deposition rate, emphasizing its significance in the process. An adaptive control algorithm that monitors the tip highly enhances the deposition quality.

Kamaraj et al. [48] demonstrated an inverse relationship between scanning speed and layer height in deposition. Faster scanning speed resulted in lower layer height, with a lower limit depending on the gap value, especially when the interelectrode gaps were set to 10 μm and 20 μm.

Jansson et al. [17] discussed enhanced deposition control and improved resolution & surface smoothness in nickel plating solutions by adding ammonia and ammonium formate. A mirror-smooth nickel column, 600 μm tall and 3 μm in diameter, was successfully built at a rate of 4 μm/s. The process demonstrated potential for even higher axial deposition rates and structure diameters as small as 2 μm.

Chan et al. [49] explored the triangular, sine, and square-waved pulse currents during electrodeposition. They found the triangular wave produces a better surface finish while generating a smaller grain size. Different orientation densities of the [1 0 0] fiber texture are observed for different waveforms, attributed to variations in the inhibiting chemical species during the electrodeposition process.

2.1.3 Microfabrication by LECD

For micro-component fabrication, the tool size must be in micron dimension. The specifications required for microtools are micro-dimension, good accuracy, and better surface finish. The process parameters for the deposition should be optimized to get a good aspect ratio of the fabricated parts. Some researchers fabricated the micro components, and the associated challenges are discussed below.

Hunter et al. [3] introduced microfabrication technology that enables the electrodeposition of truly three-dimensional metal structures. Micrometer-scale nickel

TH-3378_196103004

structures, such as a multi-coiled helical spring and a column of 10 μm diameter, have been successfully fabricated. The process involves localized electrodeposition using a sharp-tipped electrode near a substrate, with structures built by strategically moving the electrode. Remarkably, vertical deposition rates of 6 μm/s have been achieved, representing a significant improvement compared to conventional electrodeposition methods.

Wang et al. [46] investigated the surface and cross-sectional morphologies, along with the average deposition rate, of copper columns under varying potential and initial gap conditions. Lower potential (< 2.4 V) resulted in cylinder-shaped columns with few voids, while higher potential (> 2.8 V) led to dendriform-shaped columns with more voids. The average deposition rate is increased with higher potential. For the initial gap, columns were cylinder-shaped with gaps of 10 μm or below and cone-shaped with gaps of 35 μm or above. Larger gaps are correlated with decreased voids and average deposition rates.

In a study conducted by Sundaram et al. [50], localized electrodeposition of nickel pillars was experimentally investigated to assess the influence of pulse frequency, applied voltage, pulsed duty cycle, and the interelectrode gap on deposition diameter and height rate. The research explored the effects of ultra-high frequency during micro-electrochemical additive manufacturing. The findings revealed an elevated deposition height rate with increased pulse frequency, applied voltage, and duty cycle. The interelectrode gap did not significantly affect deposition diameter, but pulse voltage and frequency played a role in determining the average deposition diameter under specific conditions.

Habib et al. [42] introduced a novel method for manufacturing electrodes with complex cross-sections using a non-conductive mask. The mask is positioned between the anode and cathode, immersed in a mixed electrolyte of copper sulfate, 1.0 M sulfuric acid, and an additive agent (0.04 g/l of thiourea). Copper deposition is localized on the cathode surface by employing ultra-short voltage pulses between the anode and cathode. The cathode is strategically placed above the anode and mask, enabling the deposited electrode's direct use for EDM or other applications without altering tool orientation.

2.1.4 Literature summary for LECD

Micro-MEAM technology stands out for its ability to fabricate void-free, crack-free, low-stress microscale and nanoscale geometries. It is categorized into mask-based and maskless micro-MEAM. While mask-based micro-MEAM has diverse industrial applications, it

TH-3378_196103004

struggles with 3D micro-sized solids. Maskless micro-MEAM can form arbitrary solids but is limited in shape diversity. Future advancements in through-mask preparation methods may enhance mask-based micro-MEAM. The ongoing research aims to make maskless micro-MEAM a practical metal micro-AM technique, garnering increasing attention for its promising potential.

2.1.5 Development of SJED Experimental setup

Selective Jet Electrodeposition (SJED) is emerging as a promising technique in microadditive manufacturing. SJED shares similarities with ordinary electrodeposition, but it distinguishes itself through the mass transfer process of the electroplating solution. In ordinary electrodeposition, mass transfer relies on diffusion and electromigration. However, the SJED introduces convection as the predominant mass transfer mechanism, enhancing material transfer efficiency. With its unique fluid dynamics characteristics, this technology mechanically activates the cathode workpiece surface through the high-speed impact of the electroplating solution. This activation leads to a reduction in diffusion layer thickness, finer metal grain structure, and a more densely packed deposition bead. SJED demonstrates a more pronounced grain-refining effect than traditional electrochemical deposition methods. Researchers from diverse institutions and laboratories have actively pursued the development of LECD setups, recognizing the significance of this technology, as depicted in Table 2.2.

Table 2.2 Development of the SJED considering several aspects

Type	Development trends SJED based electrodeposition
Theoretical development	Chin et al. [43], 1978; Hsueh et al. [51], 1985 ; Chen et al. [52], 2000; Rajput et al. [53], 2015; Alkire et al. [54], 1982; Karakus et al. [55], 1994
Process condition optimization	Dover et al. [55], 1996 ; Kunieda et al. [56], 1998; Qiao et al. [57], 2005; Rajput et al. [58], 2014; Jiang et al. [59], 2018; Fan et al. [60], 2019; Wang et al. [61], 2016
Modified SJED techniques	Gutefeld et al. [62], 1983; Wang et al. [63], 2015; Li et al. [64], 2020
Electrochemical printing	Whitaker et al. [64], 2005; Nelson et al. [65], 2008

Wang et al. [66] developed a setup of SJED-based micromanufacturing. This study introduced a novel electrolyte-column localized electrochemical deposition (ECL-ECD) method for the precision manufacturing of 3D micro- and mesoscale solid objects. ECL-

TH-3378_196103004

ECD utilizes a dynamically stable electrolyte column between the electrolyte nozzle (anode) and the cathodic surface, guiding localized metal electrodeposition with controllable movement. This technique successfully produced intricate structures, including curved columnar, U-shaped, Z-shaped, and spiral structures, through various path planning and control strategies. ECL-ECD demonstrated the capability to additively manufacture micrometer-to-millimeter-scale freestanding metal geometries with high accuracy, excellent surface finish, and material compactness.

Kim et al. [67] proposed a novel selective copper metallization technique for diverse materials (i.e., glass, plastic, ceramic) with three main steps: seed layer development using electron beam evaporation, pattern fabrication via jet-circulating electrodeposition, and seed layer removal. The method utilizes the localized circulation of an electrolyte jet through concentric nozzles for rapid and selective electrodeposition.

Rajput et al. [58] developed an SJED experimental setup. Their experimental results confirmed selective electrodeposition around the impinged spot of the electrolyte jet. Successful fabrication of single-axis features (i.e., pin-like shapes) is achieved, but complex features (e.g., square-shaped parts) exhibit edge effects and geometrical inaccuracies. Non-uniform metal ion distribution at the work surface leads to uneven current distribution.

Wang et al. [68] developed a setup where Nanocrystalline nickel coatings were fabricated through pulse jet electrodeposition on a carbon steel substrate. The impact of average current density on surface morphology, microstructure, average grain size, and microhardness was analyzed using scanning electron microscopy (SEM), X-ray diffractometry (XRD), and microhardness measurement.

2.1.6 Principle of micro-electrodeposition for SJED process

SJED is gaining potential in the field of microadditive manufacturing. The principle of SJED is similar to that of ordinary electrodeposition, but the main difference lies in the mass transfer process of the electroplating solution. Mass transfer occurs primarily through diffusion and electromigration in ordinary electrodeposition, whereas in jet electrodeposition, convection becomes the dominant form of mass transfer [66]. This results in faster material transfer efficiency [69]. Jet electrodeposition technology, with its unique fluid dynamics characteristics, mechanically activates the cathode surface of the workpiece through the high-speed impact of the electroplating solution. This activation reduces diffusion layer thickness, finer metal grain structure, and a more densely packed

TH-3378_196103004

deposition bead. Jet electrochemical deposition exhibits a more pronounced grain refining effect than traditional electrochemical deposition methods [70]. In SJED, the electrolyte jet directly impacts the cathode surface. A wall jet, referred to as the relatively thin electrolyte radial layer, develops at a distance from the impingement zone, as illustrated in Fig. 2.2. The wall jet's electrical resistance is comparably higher than that of the direct impingement region due to its thin nature. Consequently, negligible or no deposition occurs compared to the direct impingement zone [67], [71]. For precise metal deposition in micro part manufacturing, the anode (nozzle) is precisely positioned in a specified orientation relative to the substrate. The elevated liquid flow velocity in jet electrochemical deposition leads to pronounced turbulence within the electrolyte, resulting in a notable reduction of bubble formation that typically occurs during the hydrogen evolution process on the substrate's surface [66]. This action improves the bonding between the deposited layer and the substrate [72].

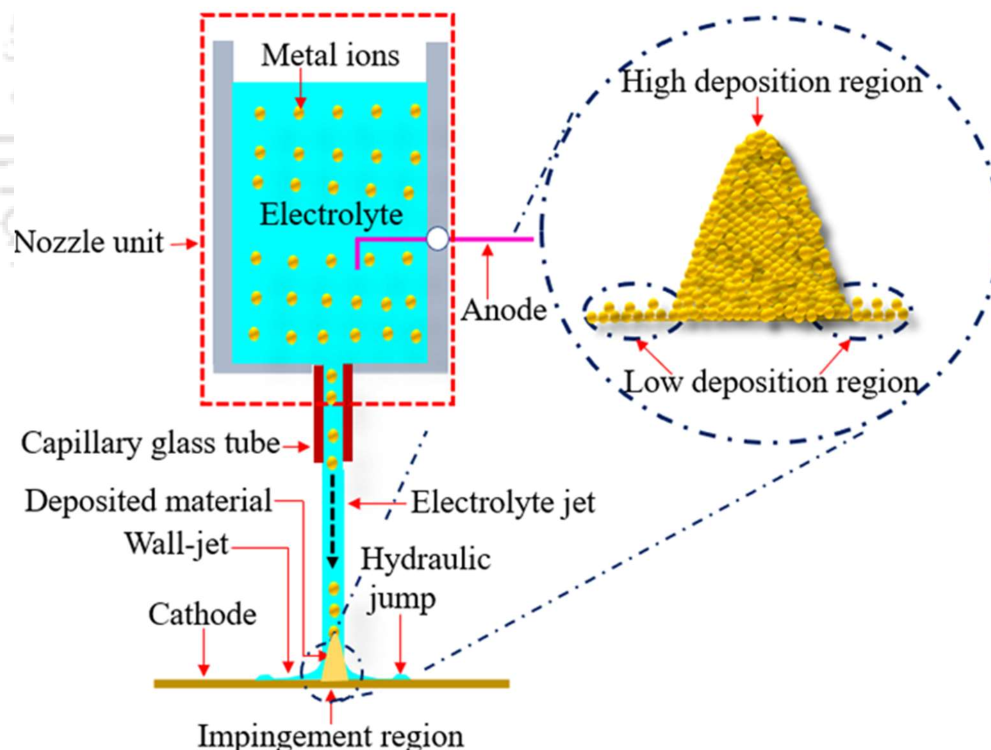

Fig. 2.2 Interaction of jet with substrate

2.1.7 Kinetics of micro-electrodeposition for SJED process

The electrochemical process is a direct function or is proportional to the electric charge passed. The material deposition rate is a function of current density (ɽ, in $mA.cm^{-2}$). Each

metal has a material density (ρ, in $g.cm^{-3}$) and electrochemical equivalent (*Z*) (also called proportionality constant), which relates deposition to current density. The linear growth rate and mass deposition rate are computed by the below relationships (Eqs. (2.1) and (2.2)).

$$\text{Linear growth rate} = 3.6 \times 10^4 \times \frac{Z \times CE \times ɽ}{\rho} \quad (2.1)$$

$$\text{Mass flow rate } (\dot{m}) = \frac{I \times M}{F \times Z} \quad (2.2)$$

Where *CE* represents the current efficiency. The electrochemical equivalent (*Z*) can be calculated as

$$Z = \frac{M}{n \times F} \quad (2.3)$$

F denotes Faraday's constant with a value of approximately 96,485 $Cmol^{-1}$. *n* signifies the number of electrons involved in the electrochemical process, and *M* represents the molar weight of the metal. The upper limit of the material deposition rate is controlled by factors such as mass diffusion or transportation and the presence of metal ion species on the cathode surface. The symbol *I* represents the current in milliamperes (mA). *A* denotes the exposed area (A, cm^2) for electroplating and is calculated using Eq. (2.4).

$$I = ɽ \times A \quad (2.4)$$

The SJED process is regulated by potential rather than current, making it advantageous when dealing with a continuously changing plated area. The conventional model, proposed by John Alfred Valentine Butler and Max Volmer, predicts the electrode current density (ɽ) using the Erdey–Grúz–Volmer equation, commonly referred to as the Butler–Volmer equation [73] (Eq.(2.5)).

$$ɽ = ɽ_0 \left[e^{\left(\frac{-F\alpha\eta}{RT}\right)} - e^{\left(\frac{(1-\alpha)-F\eta}{RT}\right)} \right] \quad (2.5)$$

Where, ɽ represents the current density of the electrode, $ɽ_0$ is the exchange current density, *R* denotes reaction rate, *T* denotes absolute temperature, and α represents the transfer

TH-3378_196103004

coefficient. In the Nernst equation (Eq. (2.6)), η is termed the activation potential, representing the difference between the electrode potential (E) and the equilibrium potential (E_{eq}). Mathematically, it is written as

$$\eta = E - E_{eq} \tag{2.6}$$

The SJED process, which is marked by irreversibility and a substantial cathodic overpotential compared to the anodic potential, the equation proposed by Butler–Volmer simplifies to the Tafel equation, initially introduced by Julius Tafel as follows (Eqs. (2.7), (2.8), and (2.9)):

$$\eta = a + b \log ɼ \tag{2.7}$$

$$a = \frac{2.3RT}{\alpha F} \log ɼ_0 \tag{2.8}$$

$$b = -\frac{2.3RT}{\alpha F} \tag{2.9}$$

For a single jet or nozzle system, the expression for the Tafel equation is given by Eq. (2.10):

$$\eta = S \times \log\left(\frac{ɼ}{ɼ_0}\right) \tag{2.10}$$

Where ɼ represents current density (in A/m^2), and S is the Tafel slope of the Tafel diagram, which is obtained by measuring experimentally. However, theoretically, it can also be computed by Eq. (2.11).

$$S = \frac{KT}{e\alpha} \tag{2.11}$$

Where K is the Boltzmann constant, which relates the average kinetic energy of a particle to absolute temperature, T, e is the elementary charge, and α is the charge transfer coefficient. From Eqs. (2.2), (2.4), and (2.6), the mass flow rate can be written as

$$\text{Mass flow rate } (\dot{m}) = \frac{\mathrm{i}_0 \left[e^{\left(\frac{-F\alpha(E-E_{eq})}{RT}\right)} - e^{\left(\frac{(1-\alpha)F(E-E_{eq})}{RT}\right)} \right] AM}{FZ} \tag{2.12}$$

Eq. (2.12) is the governing equation for a mass flow rate for high-speed jet electrodeposition.

2.1.8 Major process parameters in SJED

Selective jet electrodeposition is a microfabrication technique that involves depositing metal selectively onto a substrate using an electrolyte jet. The process parameters for selective jet electrodeposition are critical in controlling the deposition and achieving desired results. Some of the influencing process parameters for SJED are discussed below.

2.1.8.1 Effect of electrolyte composition

The composition of the electrolyte solution and the addition of additive agents significantly influence the electrodeposition process. Electrolyte concentration and composition are critical factors affecting the quality of the deposited surface. Different concentrations determine the flow of metal ions and impact polarization current. Additional agents, either organic or inorganic, play a crucial role in enhancing surface quality. Table 2.3 summarizes the solutions and additional agents used in the literature. Lin et al. [32] studied ion migration during deposition, estimating local copper ion concentration and supply through large-scale transport using potential measurements. Plating current and copper ion mass transfer rate were evaluated. Voltage and duty cycle control local concentration, impacting surface morphology and internal structure. Columns with different morphologies were prepared depending on the concentration of copper ions in the bath. A smooth nickel micron column was produced in a copper ion-free citrate solution. Varying copper ion concentrations resulted in Ni/Cu alloy microcolumns with diverse morphologies [59]. The presence of additive agents influenced the electrolytic reduction process mechanism and the microstructure of the deposited copper, yielding smooth, fine-grained, and microcrystalline deposits. A small amount of additive agents (< 0.05 g/L), such as a 0.04 g/L thiourea solution, was adequate to induce significant changes in the deposition form. The presence of thiourea enhanced the appearance of the copper pillars, resulting in improved grain deposition [17]. Pané et al. [74] studied with different additive agents. They

TH-3378_196103004

demonstrated a reduction in porosity and surface roughness when saccharin additives were introduced into the solution.

Table 2.3 List of target materials with electrolyte solution and additive agents in SJED

Reference	Material	Chemicals (concentration)	Additive agents	Applied voltage
Seol et al. [33]	Cu	$CuSO_4$ $5H_2O$ (1.05 M)	H_2SO_4 (0.8 M)	4.5 V/10 V
Madden et al. [3]	Ni	$Ni(SO_3NH_2)_2$ (450 g/L)	H_3BO_3 (30 g/L)	4.5–5V
Li [75]	Cu	$CuSO_4$ $5H_2O$(250 g/L)	H_2SO_4 (75 g/L)	3 V
Thornell [76]	Ni	$NiSO_4$ (1 M)	NH_3(2M), $HCOONH_4$	4-5V
Chang [77]	Ni	$NiSO_4$ (330 kg/m^3), $NiCl_2$ $6H_2O$ (45 kg/m^3)	H_3BO_3 (37 g/L)	3.2-4.6V
Nelson [78]	Cu	$CuSO_4$ $5H_2O$(0.1M)	H_2SO_4 (0.001M)	
Wang [29]	Cu	$CuSO_4$ $5H_2O$(100g/L)	H_2SO_4 (58.8 g/L)	3.1-3.9V
El-Giar [40]	Cu	$CuSO_4$ $5H_2O$ (250 g/L) and $CuSO_4$ $5H_2O$ (180 g/L)	H_2SO_4 (75g/L) thiourea (0.04 g/L) and H_2SO_4 (75g/L) chloride ion (80mg/L)	2.0-6.0 V
Sundaram [79]	Ni	$NiSO_4$ (240 g/L), NiCl (45 g/L)	H_3BO_3 (37 g/L)	4-5V
Lin [59]	Ni–Cu	Nickel sulfate (0.2 M), copper sulfate (0.0004-0.012M)	Sodium citrate (0.3M) and sodium chloride (0.003M)	3.8 V, 4V, 4.2V, and 4.4V
Sundaram [80]	Ni–Cu	Nickel sulfate (150 g/L) & copper sulfate (2g/L) and nickel sulfate (102g/L) & copper sulfate (4g/L)	H_3BO_3 (30g/L) and sodium citrate (71g/L)	4V/5V
Luca [81]	Cu	$CuSO_4$ $5H_2O$ (1.05M)	H_2SO_4 (0.8M)	-0.7V
Wang [82]	Au	$HAuCl_4$ (5Mm), $K_4Fe(CN)_6$(5mM)	H_2SO_4 (0.1M), K_2SO_4 (0.1M)	3-5V
Hu [83]	Pt	0.05 M $CuSO_4$ and H_2PtCl_6		0.2V

2.1.8.2 Effect of applied voltage

Chang et al. [84] investigated that below 3.56 V resulted in smooth, fully compacted columns, while voltage above 3.56 V leads to rough surfaces and distorted transverse structures. Voltage changes influence both the internal structure and topography of copper deposits, resulting in various surface structures such as rough surfaces, hollow copper tubes, cratered top pillars, flat-top copper columns, and domed-top copper columns. The simulation study [85] also resulted in the formation of a rough surface with a higher voltage application.

TH-3378_196103004

Chang et al. [84] determined a threshold voltage of 3.56±0.01 V for effective deposition. Operating at a voltage below this threshold resulted in smooth-surfaced columns with circular internal lateral compaction, while the voltage above this threshold led to rough surfaces and distorted circular lateral structures with porosity at the center. In recent research by Kamaraj et al. [25], a voltage threshold was identified at 2 V, marking the onset of the limiting current region, where voltage became a crucial parameter determining current density. The applied voltage significantly influences the electric field distribution between the poles, leading to various morphologies of copper deposition based on different forms of electric field distribution on the cathode surface [76]. As the voltage varied from 4.5 to 10.0 V with a fixed gap distance (L=5 μm), the electric field strength sharply increased at the microelectrode's edge, enhancing electrochemical deposition below the edge. The electric field distribution changed with the control voltage, aligning with the observed growth results [86]. The literature review indicates that the change in voltage influences the electric field distribution, impacting metal ion distribution and, consequently, deposition quality.

2.1.8.3 Effect of duty cycle

Two types of power supplies are used in an electrochemical deposition: DC (direct current) and pulsed power supply. DC considers only the applied voltage magnitude, while pulsed power supply considers both magnitude and duty cycle. The duty cycle significantly influences deposition quality by providing sufficient time for metal ions to replenish. Lin et al. [32] studied pulsed voltages and currents in LECD. They found that the lower voltage (2.8 V) and duty cycle (0.1) produce the best deposition quality. Increasing voltage and duty cycle degraded deposited surface quality [32]. The study by Yang et al. [59] demonstrated that pulsing in SJED allows control over the morphological characteristics of the deposited material. A decrease in the duty ratio led to forming a cubical Cu_2O film, transitioning into spherical particles. However, the authors did not provide information on the effect of the electrode gap. Kim et al. [87] observed that the current density and duty ratio are crucial in controlling nuclei formation and dendritic growth. It's important to note that mechanical properties such as ductility and malleability depend on grain size and shape. The higher current intensity was found to increase density by enhancing the deposition rate. Increasing current intensity leads to greater density by boosting the deposition rate. However, the dominant factor is the pulse on time or active time (i.e.,

TH-3378_196103004

duration for which electrodeposition is performed). Other influential parameters include voltage and current density, as observed by Bolzán et al. [88].

2.1.8.4 Effect of electrolyte gap

This section provides a brief overview of the impact of the interelectrode gap on localized electrodeposition. The size of the interelectrode gap emerged as a crucial factor determining the success of the deposition process. A smaller interelectrode gap was associated with forming an ion depletion region, potentially causing a short circuit between the anode and cathode. In contrast, a larger interelectrode gap resulted in inadequate current density in the interpolar region, hindering the migration of metal ions and leading to localized deposition failure [47]. A very small interelectrode gap could lead to undesired short circuits when metal ion deposition efficiency exceeds the anode's vertical movement speed. Additionally, it hindered ion mass transfer and influenced ion diffusion and migration, causing uneven deposition with fully depleted ion regions [89].

In the proposed Jet-based deposition technique, electrolyte flow characteristics were experimentally analyzed. At 12.3 kPa pressure, a hydrodynamically stable electrolyte column (over 70 mm) was formed without observable oscillations. Reduced pressure led to instability, with a gradually shortened column's effective length. At 1.4 kPa, the electrolyte column became significantly unstable, dissociating into droplets. However, at 12.3 kPa, the electrolyte column was considerably stable, maintaining laminar flow. The stable electrolyte column flow was verified by the in-situ electrodeposition method, demonstrating good flow stability under various inter-electrode gaps [66].

2.1.8.5 Effect of nozzle speed

The nozzle withdrawing and scanning speeds are crucial in electrodeposition. Excessive withdrawing speed leads to bamboo-like structures or deposition failure, while low speed causes a short circuit. Scanning speed determines layer thickness, affecting the print rate and accuracy. The movement relies on micromotion platform performance, influencing deposition. Electrode speeds must match the deposition growth rate. Scanning speed inversely correlates with layer height, impacting deposit height and quality.

The scanning speed in jet electrodeposition influences coating growth and morphology. At 200 mm/min scanning speed, coatings exhibit large cellular structures with clear boundaries. Increasing speed to 400 mm/min reduces grain size, and at 600 mm/min,

TH-3378_196103004

a uniform, smooth, and compact structure emerges. Grain size remains similar beyond 600 mm/min, but defects like cracks appear. Slower speeds allow longer current action, promoting larger grain growth. Faster speed limits deposition, resulting in smaller grains. Extremely high speeds disrupt the flow field, reducing fluid stability and causing surface defects. Optimal scanning speed enhances coating quality [90]. Tests at varying scanning speeds showed that coating thickness followed a trend of increasing and then decreasing with higher speeds, aligning with numerical solution results. Uniform and smooth thickness were observed at low speeds, while higher speeds led to lower thickness uniformity [90]. The hardness initially increases and then decreases with the rise in scanning speed [91].

2.1.9 Microfabrication by SJED

The feasibility of additively manufactured 3D complex structures and components with SJED was examined. U-shaped and spiral structures were successfully formed with high precision, smooth surfaces, and satisfactory geometric accuracy [66]. The results confirmed the excellent ability of SJED to precisely manufacture 3D complex structures, indicating promising engineering application potential. Wang et al. [63] introduced a grinding-assisted template-based Jet ECD method to improve forming accuracy and surface quality. SJED technique is utilized for the fabrication of complex copper film-patterns with enhanced electrical and mechanical properties. The resulting copper film-patterns exhibit significantly improved electrical (resistivity 1.84 μΩm) and mechanical (hardness 905 MPa) properties compared to traditional electrodeposition methods [92].

2.1.10 Characterization of deposited microparts by SJED

SJED achieved rapid deposition rates and improved material characteristics. Other methods, such as ultrasonic jet-assisted electrodeposition, laser-assisted SJED, and mask-electrodeposition, are also been developed. This section will explore the advancements in individual characteristics.

2.1.10.1 Homogeneity and density

Uneven deposition, addressed by Kasper [93] and Tobias et al. [94] due to electrode resistance causing uneven current density in the impingement zone, is a crucial consideration for material homogeneity. Volgin et al. [95] focused on achieving homogeneous deposition over the entire surface, including edges. SJED offers denser

TH-3378_196103004

deposition than conventional electrodeposition, as demonstrated by Unveroglu et al. [96]. High-speed electrolytes, multiple passes, and a redox potential of -1.95 V contribute to the homogenous electrodeposition with low voids and smaller particle sizes, enabling mass production of smaller parts and thin-layer coatings. The density increases with longer deposition times, forming dendroid structures [97].

2.1.10.2 Thickness

The deposited material thickness in electroplating ranges from microns to millimeters, depending on the technique and active electrodeposition time. Cu^{++} abundance promotes rapid electrolysis in a controlled environment. Alebrahim et al. [98] demonstrated that increasing pH values on the higher side enhances ion transfer rates, and thickness rises subsequently. Gelchinski et al. [99] concluded that increasing power density increases deposition thickness. They discovered a 0.05 mm diameter metallic nozzle capable of depositing material at a speed of 12 mm/s, significantly reducing voids and improving density. The electrodeposited gold specimen exhibited characteristics within the range of soft gold. Rajput et al. [100] analyzed the scanning electron microscope images. They concluded that the thickness of the target material (e.g., copper) increases with an increase in the potential difference between the electrodes. Babaei et al. [101] optimized electrochemical operative parameters for Au-Cu deposition. Their findings indicated that the thickness of the electrodeposited layer decreases when the pulse off-time is too short.

2.1.10.3 Surface roughness

The SJED process is noted to provide a smoother surface than conventional DC electrodeposition. Baral et al. [102] observed that adding selenium (Se) to an electrolyte, such as copper sulfate solution, has been shown to increase surface roughness and irregularities in morphological characteristics. The impact is most significant at 60°C, leading to roughness attributed to substrate material inhomogeneity, intricate geometry, and localized electrodeposition rate. Shen et al. [103] introduced the rotating interlacing method as a novel approach in jet electrodeposition to minimize surface roughness and enhance the adhesive strength of NdFeB.

TH-3378_196103004

2.1.10.4 Porosity

Porous metallic parts, with pore sizes ranging from 1–10 µm, find applications in bearings and self-lubrication due to their unique mechanical properties and lightweight. Factors influencing porosity include grain growth, electrochemical kinetics, and nucleation. A higher duty ratio and applied potential result in less porosity in pulse electrodeposition. Porosity can be desirable for self-lubrication, and porous structures exhibit increased ductility compared to solid counterparts of the same material. Kamaraj et al. [104] experimentally found that less porous localized deposition can be obtained by increasing the applied potential.

2.1.10.5 Grain fineness

In SJED, short pulsing intervals lead to fine grain structures, resulting in improved mechanical properties but potentially less dimensional accuracy than laser and LIGA techniques. The coarse grain growth is avoided with short pulsing times, and fine grains smaller than a micron can be obtained. Prolonged pulsing beyond 10 seconds may lead to dendroid structures in long-term electrolysis processes [105]. Finer grains in a material tend to adopt a spherical shape, creating interstitial spaces between adjacent grains. The grain size indirectly influences the porosity of the material [106]. Adding aluminum oxide fine particles to the electrolyte refines the grain microstructure and significantly improves the mechanical characteristics of the deposited surface of the composite [107].

2.1.10.6 Shape accuracy

SJED can be used for micro metallic interconnects with two-dimensional features, neglecting thickness. It offers improved accuracy in part shape compared to conventional DC electrodeposition for industry-grade applications. The presence of inorganic salts in electrolytes enhances the ion transfer rate of copper ions. However, improper electrodeposition in the impingement region can lead to edge effects and separation of cylindrical structures [53].

2.1.11 Literature summary for SJED

Electrodeposition has evolved significantly, transitioning from electroplating single metals to alloy ions and composites. SJED is a recent technique that has seen fewer experiments than traditional electrodeposition. While conventional methods have focused on single

TH-3378_196103004

metals, SJED has expanded to deposit metal composites in metal matrices for composite MEMS features. The technique allows for rapid single-step thin-layer electrodeposition with high precision, enabling the deposition of agitated ions on various substrates, including plastics and composites. Researchers are exploring factors such as catalytic agents, electrolyte pH, optimum pulse-on time, and substrate pre-processing to enhance the technology. SJED applications extend beyond semiconductor and metallic interconnects, including corrosion protection, photovoltaic applications, and coatings for ceramics and conductive polymers, offering alternatives to precious metals.

2.2 Scope of research

Research on micropart fabrication using toolpath techniques is limited, providing opportunities to optimize toolpaths for precise dimensions, geometries, and surface finishes. Additionally, bead analysis, particularly regarding height, width, and surface morphology, remains underexplored and is necessary for understanding deposition quality and achieving void-free coatings. Multi-bead analysis is also critical in evaluating deposition quality on flat surfaces, necessitating input parameter optimization for uniform and defect-free layers.

2.3 Research contribution

An economic selective jet electrodeposition setup capable of fabricating microparts has been developed in the present thesis. TSP-based toolpath analysis is done using the optimized parameters. Single bead is analyzed in terms of layer height, width, and surface morphology. Multibead analysis is carried out to obtain the flat surface between the two adjacent beads. With the help of the TSP-based toolpath, gradient-based microstructures are deposited and further separated from the substrate. The application of the SJED process in terms of coating is also performed. It is observed that the thick coating developed with SJED has better mechanical properties than the conventional electroplating process.

TH-3378_196103004

Chapter 3 Development of SJED process for micro-additive manufacturing

3.1 Introduction

CAPP, which stands for Computer-Aided Process Planning, plays a crucial role in the Selective Jet Electrodeposition (SJED) process. In SJED, CAPP involves using computer-based tools and systems to plan and optimize the manufacturing processes related to electrodeposition. This includes planning the sequence of operations, selecting suitable parameters, and optimizing the overall production process for efficiency and quality in the context of SJED. CAPP helps streamline the planning and execution of electrodeposition tasks in SJED, contributing to improved precision and control in the manufacturing process. This chapter explains the experimental setup and the entire process planning, including substrate preparation, deposition, and separation of micro-deposited parts.

3.2 SJED setup

Fig. 3.1 explains the different components and their functions within the SJED setup. The entire experimental setup of SJED can be categorized into three major systems: nozzle unit, CNC controller unit, and power supply unit, as shown in Fig. 3.4.

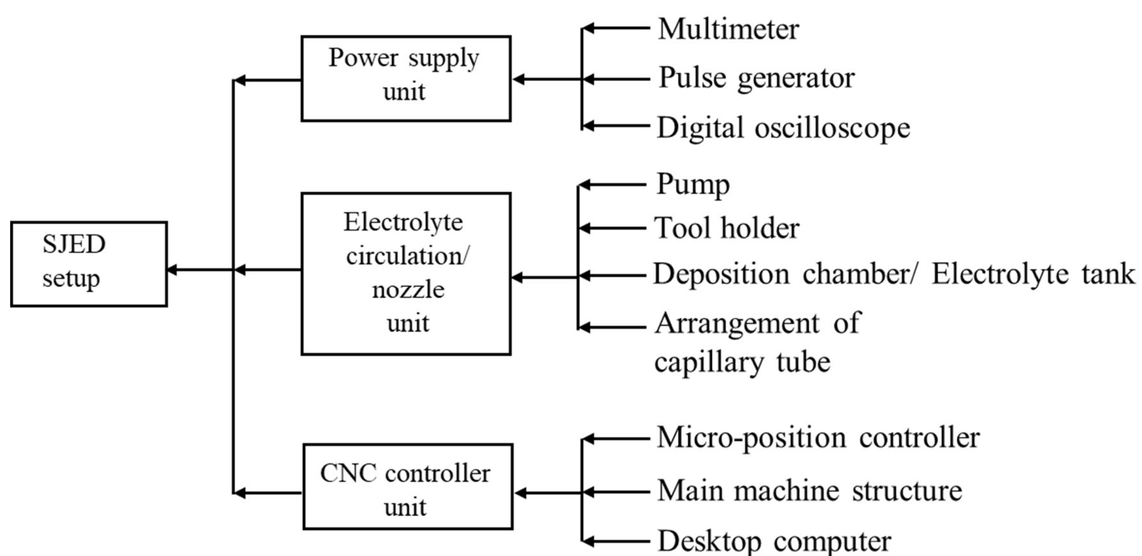

Fig. 3.1 Different subsystems of developed SJED setup

TH-3378_196103004

3.2.1 Power supply unit

In SJED, the deposition initiates when a potential is applied between the tool and the workpiece using a power supply unit. Typically, direct current (DC) power is employed by the power supply unit. In the SJED process, the tool is connected to the power supply's positive terminal (i.e., anode), while the workpiece is connected to the negative terminal (i.e., cathode). DC power in SJED offers two options: constant DC and pulse DC. In constant DC, the potential amplitude remains fixed throughout the process. In pulse DC, the amplitude varies during the process, with distinct on-time (t_{on}) and off-time (t_{off}) intervals in a repeating cycle. During t_{on}, deposition occurs as an electrochemical reaction takes place with maximum potential amplitude. Conversely, the potential amplitude is minimal or near zero during toff, and no reaction occurs. This off-time is essential for replenishing fresh electrolytes between inter-electrode gaps (IEG). The power supply unit mainly consists of the DC power source, function generator, and digital oscilloscope. The DC power source is the instrument used to supply the potential difference between the electrodes. The present study uses the DC power source (DOA 75 V– 4A DC power supply made by Matsusada Inc.). In this power source, the function generator is not built-in. Thus, an external function generator (Make-Rigol, Model-DG4062) is utilized to generate pulse frequency. It has the provision to change the different pulses like sine, square, triangle waves, etc., duty cycle, and frequency. In the present study, a square wave is utilized for SJED, as the amplitude of the potential remains constant. A digital oscilloscope (Make-Scientech, Model-402) with a bandwidth of 70 MHz and a sampling rate of 1GSa/s is attached in parallel between the electrodes to visualize the pulses and their variation between the electrodes. A sample of pulse images on an oscilloscope is depicted in Fig. 3.2. Increasing the pulse power frequency from 100 kHz to 500 kHz results in observable pulse distortion. The power unit system consists of a digital multimeter (DMM) connected in series between the anode and substrate, capable of measuring the current in the µA range. A sample of wave images on a DMM is depicted in Fig. 3.3.

TH-3378_196103004

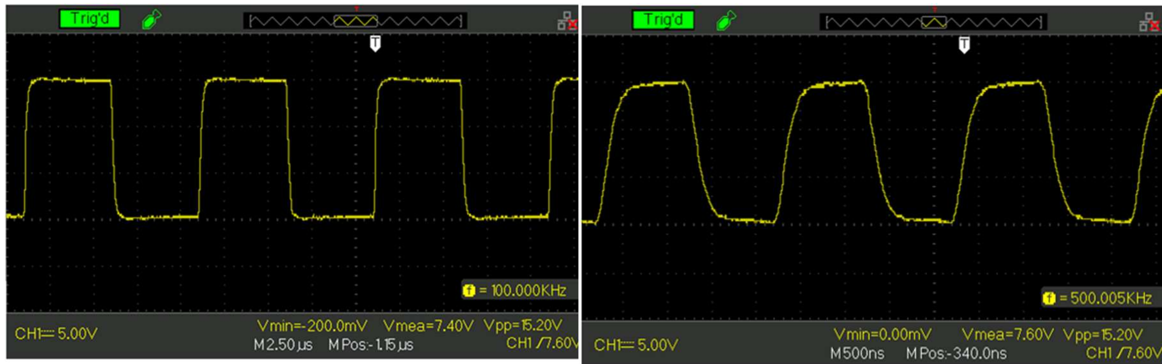

(a) (b)

Fig. 3.2 Pulse condition (a) 100 kHz and (b) 500 kHz

(a) (b)

Fig. 3.3 Wave images captured by DMM at (a) 3V and (b) 5V

3.2.2 Electrolyte circulation and nozzle unit

The intricate details of the electrolyte circulation and nozzle unit system, a critical component in the overall setup, are discussed in this section. The system is comprised of carefully engineered components, including the nozzle, anode (i.e., platinum wire), pump, and capillary tube. The nozzle, the heart of the system, is meticulously designed to include essential features such as an inlet, anode, and outlet. Each component serves a specific purpose in facilitating controlled electrolyte delivery. The nozzle fabrication is accomplished using the fused filament fabrication (FFF) additive manufacturing technique. This section delves into the advantages and intricacies of employing FFF, emphasizing precision and reliability in the manufacturing process. The capillary tube, with an inner diameter of 250 and 500 µm, plays a crucial role in the system's fluid dynamics. The tight integration of the capillary tube with the nozzle outlet is required to enhance the efficiency of electrolyte delivery. An essential component, the platinum wire anode, is strategically inserted through a dedicated passage in the nozzle. These design considerations are crucial to ensure the optimal alignment and functionality of the inserted anode. The inlet of the nozzle is seamlessly connected to the electrolyte supply and circulation system. The

TH-3378_196103004

electrolyte circulation system maintains a steady flow rate by utilizing an electrolyte tank, a submersible pump with an 80W power rating (shown in Fig. 3.5 (a)), and both inlet and outlet pipes, as shown in Fig. 3.4. A tool holder, crucial for the stability and ease of assembly and disassembly, is fabricated using the FFF technique. It ensures the secure integration of the nozzle unit components.

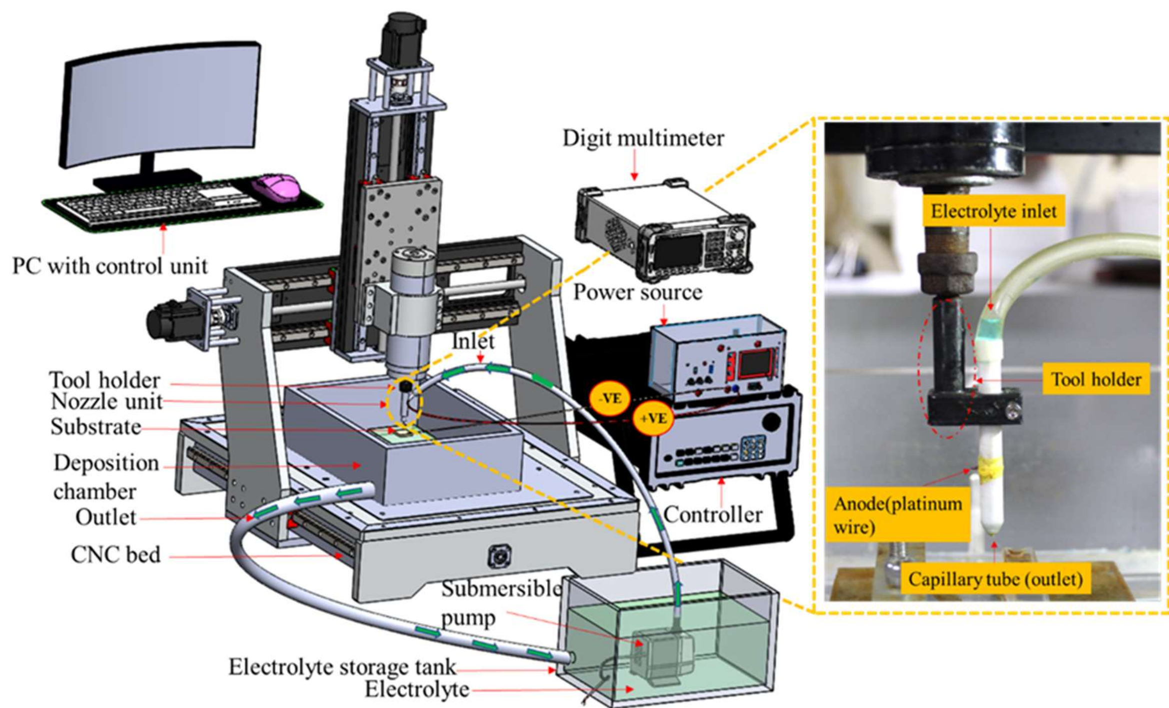

Fig. 3.4 Selective jet electrodeposition (SJED) experimental setup

(a) (b)

Fig. 3.5 (a) Submersible pump and (b) deposition chamber of SJED setup

The deposition chamber (Fig. 3.5(b)) is made of perspex material as it is filled with electrolyte. Perspex is a non-conductive material and does not react with the electrolyte.

TH-3378_196103004

The fixture for the workpiece is made to hold the workpiece and, at the same time, provide a power supply to it, as shown in Fig. 3.5 (b). The complete workpiece fixture is fabricated with perspex and fixed to the electrolyte container. A hole with a tap of 6 mm is made on the perspex sheet to hold and supply power to the workpiece. A gap is maintained between the workpiece and the bolts to avoid any loss of charge, as these bolts are conductive (Fig. 3.5 (b)). The bolts (1 to 4) do not contact the workpiece; only bolt 5 is connected to the workpiece to provide power supply.

3.2.3 CNC control unit

The precise movement of the tool and workpiece in micromachining is achieved with the help of a CNC machine. The present study uses a CNC (make-Holmarc) gantry stage with three axes in XYZ directions, as shown in Fig. 3.6. The motorized XYZ gantry stage comprises aluminum alloy and steel with black anodized finishing. The configuration of the gantry, the Z-axis, which is fixed to the Y-axis, moves over a fixed platform. The length and width of this platform covered by Z-movement are limited to traverse in the X and Y axes. The Y-axis is placed over the X-axis, and the guide rail has a recirculating ball bearing. The maximum load-carrying capacity for the X and Y axes is 20 kg, whereas for the Z-axis it is 5 kg. The maximum speed for the movement of the X and Y axes is 16 m/sec, and for the Z-axis, it is 4 m/sec, with a resolution of 0.1 μm in all three axes. The X, Y, and Z axes are placed over three lead screws individually, as shown in Fig. 3.6

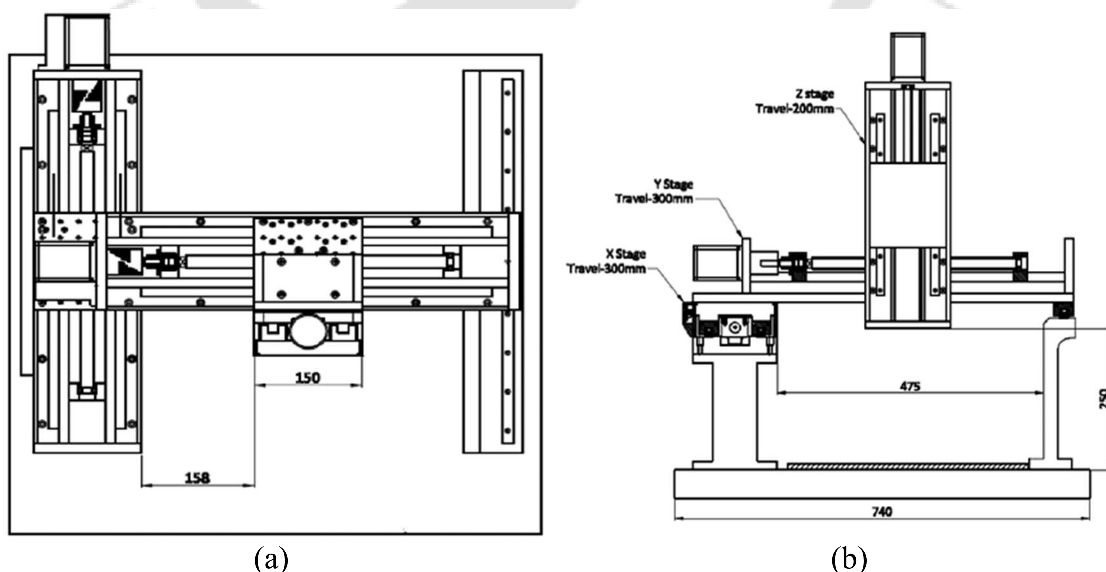

(a) (b)

Fig. 3.6 XYZ gantry stage (a) top and (b) front view

TH-3378_196103004

The precise coordination of the three axes is carefully orchestrated by a microcontroller connected to a computer running with Mach3 software, as illustrated in Fig. 3.7(a). The microcontroller establishes connections with the stepper motors responsible for governing the movement of all three axes. A specialized G-code is generated using Mach3 software, and this code is subsequently transmitted to the respective stepper motors, ensuring precise and controlled motion. A spindle (Fig. 3.7 (b)) is mounted on the z-axis, and the nozzle is fixed with the spindle through a collet.

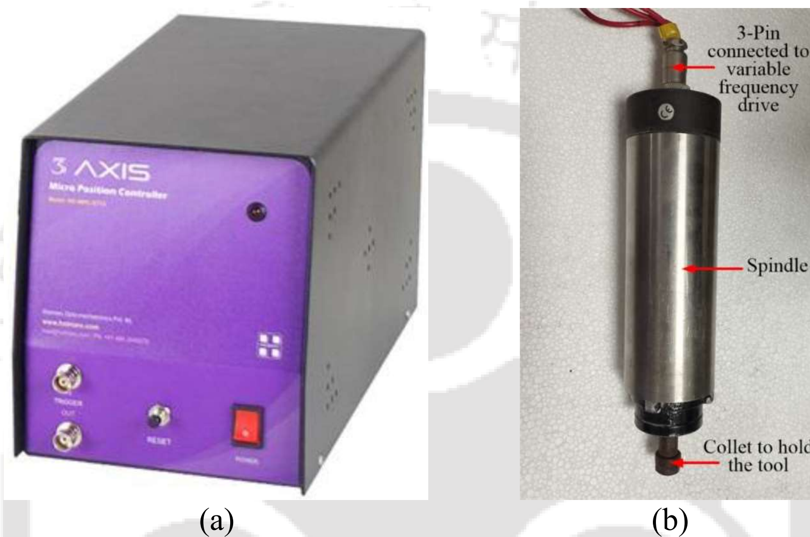

(a) (b)

Fig. 3.7 (a) Micro position controller and (b) spindle to rotate microtool

3.3 Computer-aided process planning for SJED process

This section explains the entire SJED process, including substrate preparation, deposition, and the separation of micro-deposited parts. Due to the strong interfacial metallurgical bond between the parts and the substrate, conventional mechanical separation methods become challenging, as they may cause breakage or deformation of the micro parts. A unique process is developed to address this issue, as shown in Fig. 3.8, which involves three sub-processes: pre-process, in-process, and post-process. This study considers two metals, nickel and copper, for deposition. For nickel deposition, Field's metal, an eutectic alloy with a melting point of 62°C, serves as the sacrificial material. However, due to its high reactivity with copper, Field's metal cannot be used for copper deposition. Consequently, a different substrate, SUS-304 steel, is chosen for copper depositing.

TH-3378_196103004

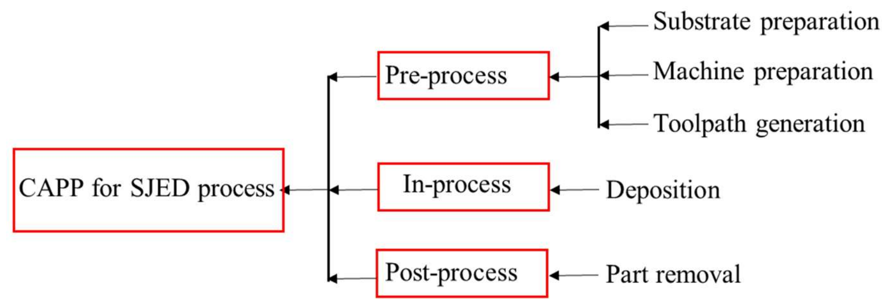

Fig. 3.8 Different subprocesses for CAPP of SJED-based deposition

3.3.1 CAPP for nickel-based SJED process

The pre-process consists of three sections: substrate preparation, machine preparation, and tool path generation, as shown in Fig. 3.9. Substrate preparation involves four steps: mold preparation, pouring of field metal, solidification of Field's metal, and flipping of the solidified mold. Fields metal, which is a eutectic alloy of bismuth (32.5%), indium (51%), and tin (16.5%) with a melting point of 62°C, is poured into a square hollow mold (20×20× 5 mm^3). The mold is placed on a cleaned glass plate. After solidification, the mold is separated from the glass plate by manually applying a horizontal force. The separated mold is then flipped to expose the side in contact with the glass plate, providing a mirror-like finished structure without further polishing. The surface roughness of the fabricated substrate is measured to be 0.128 µm.

Machine preparation involves substrate mounting, generating the electrolyte jet using a pump, and connecting all the machine parts to the power supply unit while setting the appropriate process parameters. Tool path generation is achieved through four steps: CAD design of the component, slicing, tool path generation, and generation of the respective numeric control (NC) file.

During the in-process phase, the deposition is initiated following an algorithm to achieve the desired height of the deposited parts. Finally, the post-process involves four steps: mechanical testing of the parts, melting the substrate, collecting the deposited parts, and assembling the separated micro parts at the desired location. In the post-process, the melting of the substrate is accomplished by placing the substrate (on which the deposition was performed) inside a jar filled with hot water at 90°C. Since the melting point of Fields metal is 62°C, it starts melting and collects at the bottom of the jar, while the printed micro-part remains in its original undistorted form, allowing for easy separation. The collected Field's metal can be reused, making the process economical.

TH-3378_196103004

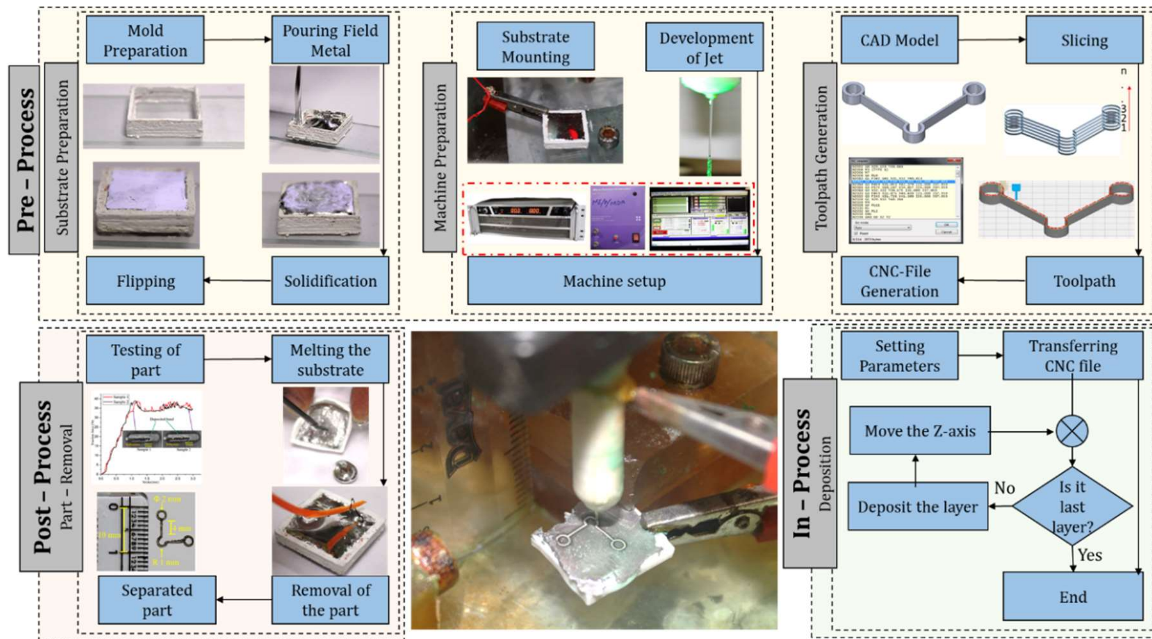

Fig. 3.9 Steps involved in separating deposited micro parts

3.3.2 CAPP for copper-based SJED process

The process for fabricating micro-deposited parts for nickel deposition explained previously is the same for copper deposition except for substrate preparation and removal. The electrolyte used for the copper deposition is highly reactive with the Field's metal. Hence, a novel substrate removal method is developed for copper deposition using SUS-304 steel as initial substrate material with 0.05 mm thickness, as shown in Fig. 3.10. This choice of substrate thickness (i.e., 0.05 mm) allows for the substrate (SUS-304 steel) to make it bend after deposition, facilitating the easy separation of the deposited structure as shown in Fig. 3.11. However, stainless steel is highly corrosion-resistant due to the presence of a significant amount of chromium. Hence, it does not allow electrodeposition, especially at lower voltage. Therefore, the substrate is initially treated with concentrated HCl acid. After 10 minutes of treatment, the outer surface becomes deficient in chromium, making it suitable for the deposition process at lower voltage.

TH-3378_196103004

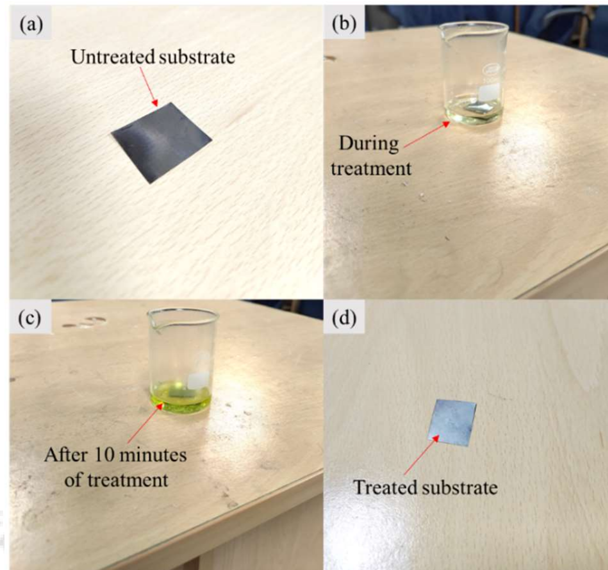

Fig. 3.10 Substrate preparation for copper-based deposition (a) untreated substrate, (b) during treatment, (c) after 10 minutes of treatment, and (d) treated substrate

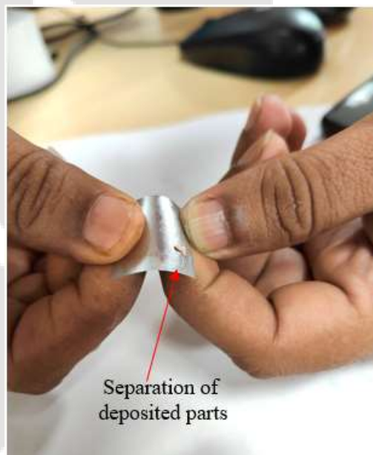

Fig. 3.11 Separation of deposited parts

3.4 Summary

This chapter presents the development of an experimental setup for SJED. The experimental setup consists of sub-systems: the power supply unit, electrolyte circulation and nozzle unit, and the CNC controller for precise movement. The pulse DC power supply is attached with a digital oscilloscope to monitor the pulse power. The workpiece holding device and the electrolyte container are fabricated with Perspex, as they are non-reactive and non-conductive to the electrolytes. The precise movement of the tool and workpiece is achieved using a CNC controller. This chapter discusses the CAPP for nickel and copper depositions. The substrate preparation methods for nickel and copper depositions are developed to remove the deposited microparts easily.

TH-3378_196103004

Chapter 4 Parametric investigation and toolpath strategies for SJED process

4.1 Introduction

Selective Jet Electrodeposition (SJED) is an emerging AM technology that enables the production of metallic components at the nano and micro scales. In the SJED process, a jet of electrolytes is facilitated between the nozzle and substrate. The deposition on the substrate takes place in an atom-by-atom manner. Conducting a parametric investigation is crucial for attaining an optimized set of process parameters. This ensures the production of uniform components devoid of voids and exhibits dimensional accuracy. The SJED process is utilized to micro-fabricate 3D complex components layer-by-layer. Therefore, determining the geometry of individual weld beads and overlapping multiple beads is essential for attaining superior surface quality and dimensional accuracy while manufacturing the fabricated parts.

The present chapter studies the effect of input process parameters (i.e., applied voltage, scanning speed, and nozzle diameter) on the deposition profile while depositing multilayered single beads. The optimized set of parameters, ensuring uniform bead geometry, is the foundation for multi-bead optimization. The process involves determining the most suitable center distance between two adjacent beads to achieve a flat surface condition, an aspect obtained through experimental analysis. Two metals, nickel and copper, are considered for the present investigation. By establishing the optimized center distance between adjacent beads, various tool path strategies are examined in the analysis. The goal is to observe how the number of turns in the toolpath influences the surface roughness and dimensional accuracy of the deposited parts. The above investigation for nickel and copper depositions is discussed in the following sub-sections.

4.2 Nickel deposition through SJED process

In this section, the selection of material and the tool for nickel electrodeposition has been discussed. The details about the process parameters for the deposition of a uniform single multilayer bead and the characteristics of the deposited bead have been explained. The experimental analysis for achieving a flat surface condition through multi-bead deposition

TH-3378_196103004

has been conducted successfully. The optimized center distance between adjacent beads has been determined through experimentation.

4.2.1 Materials and method

The nickel electrodeposition process commonly utilizes a Watt's bath as the electrolyte, which consists of various constituents outlined in Table 4.1. In this electrolytic solution, nickel sulfate serves as the primary source of ions for the deposition. At the same time, nickel chloride contributes to nickel ions and enhances the conductivity of the solution. Boric acid is incorporated in specific proportions to maintain a pH of 4.5 [68]. Several additives play essential roles in the process; Saccharin sodium acts as a brightener and coating agent, and sodium dodecyl sulfate acts as a cathode surfactant, reducing the interfacial tension between the electrode and the electroplating solution. This surfactant prevents the adherence of hydrogen formed during the process to the cathode's surface, thus minimizing the occurrence of pinholes and irregularities [108].

Table 4.1 Electrolyte bath composition

Chemicals	Amount (g/L)	purpose
Nickel sulfate ($NiSO_4.6H_2O$)	260 g/L	Ni source
Nickel chloride ($NiCl_2.6H_2O$)	40 g/L	Conductivity
Boric acid (H_3BO_3)	40 g/L	Buffer
Sodium dodecyl sulfate	0.1 g/L	Surfactant
Saccharin sodium	2 g/L	Brightener

The substrate, functioning as the cathode, is composed of Fields metal with a melting point of 62°C. The process involves depositing a bead of 224 layers, each with a fixed length of 3 mm. The initial electrolyte column height from the nozzle tip to the substrate surface of 2 mm is considered for each experiment. After the deposition of each layer, a constant upward movement of 0.5 µm is provided in the z-direction. The layer height and width of the deposited beads are determined using a non-contact profilometer. Surface morphology analysis of each deposit is conducted using the field emission scanning electron microscope (FESEM) images.

It is important to note that all measurements in this study are conducted while the deposited micro-parts remain attached to the substrate (Field's metal). This approach is adopted to minimize potential errors that may arise while handling the micron-scale structures separately, as they are susceptible to bending or distortion during measurements.

TH-3378_196103004

By keeping the micro-parts intact with the substrate, more accurate and reliable measurements can be obtained.

4.2.2 Process parameters

In conventional electrodeposition, several process parameters influence the efficiency and effectiveness of the electrodeposition process. However, layer height and width of the deposition are significantly influenced by the applied voltage, frequency of current, inter-electrode gap, and scanning speed [109]. Various process parameters significantly influence the deposition rate and the morphology of the deposited material in SJED, as illustrated in Fig. 4.1. In the present study, the effect of applied voltage, scanning speed, and nozzle diameter are analyzed on total layer height, width, and morphology of the deposited structure. Furthermore, the effect of the nozzle opening diameter on the stable column length of the electrolyte is also analyzed. The range of process parameters used for the present study is shown in Table 4.2.

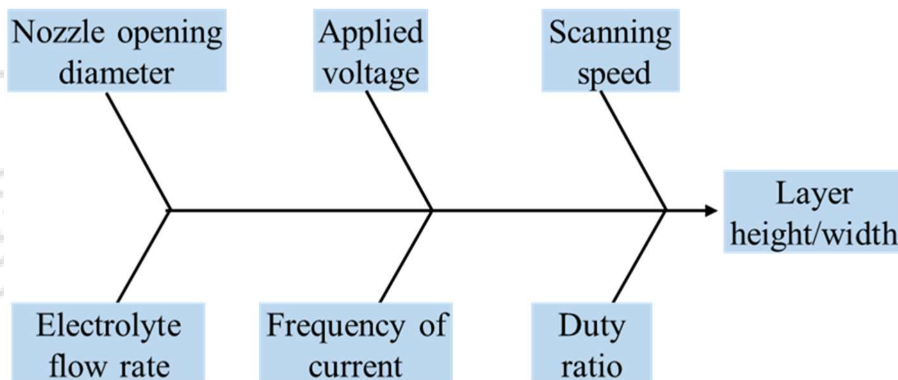

Fig. 4.1 Process parameters of SJED process with responses

Table 4.2 Process parameters and their ranges

Parameters	Ranges
Internal diameter of nozzle (μm)	250, 500
Electrolyte flow rate (ml/sec)	0.25
Initial jet distance from substrate surface (mm)	2
Applied voltage (V)	10, 15, 20
Scanning speed (mm/min)	60, 80, 100

4.2.3 Influence of process parameters on deposition profile/morphology

TH-3378_196103004

This section discusses the influence of various deposition parameters on critical aspects such as deposition height, width, and overall morphology of the deposited structure.

4.2.3.1 Effect of nozzle diameter on electrolyte column length

An experimental analysis of the flow characteristics of electrolyte was conducted to ensure a stable and consistent electrolyte column length in the proposed SJED process. A constant flow rate of 0.25 ml/sec is used for each experiment facilitated by a submersible pump.

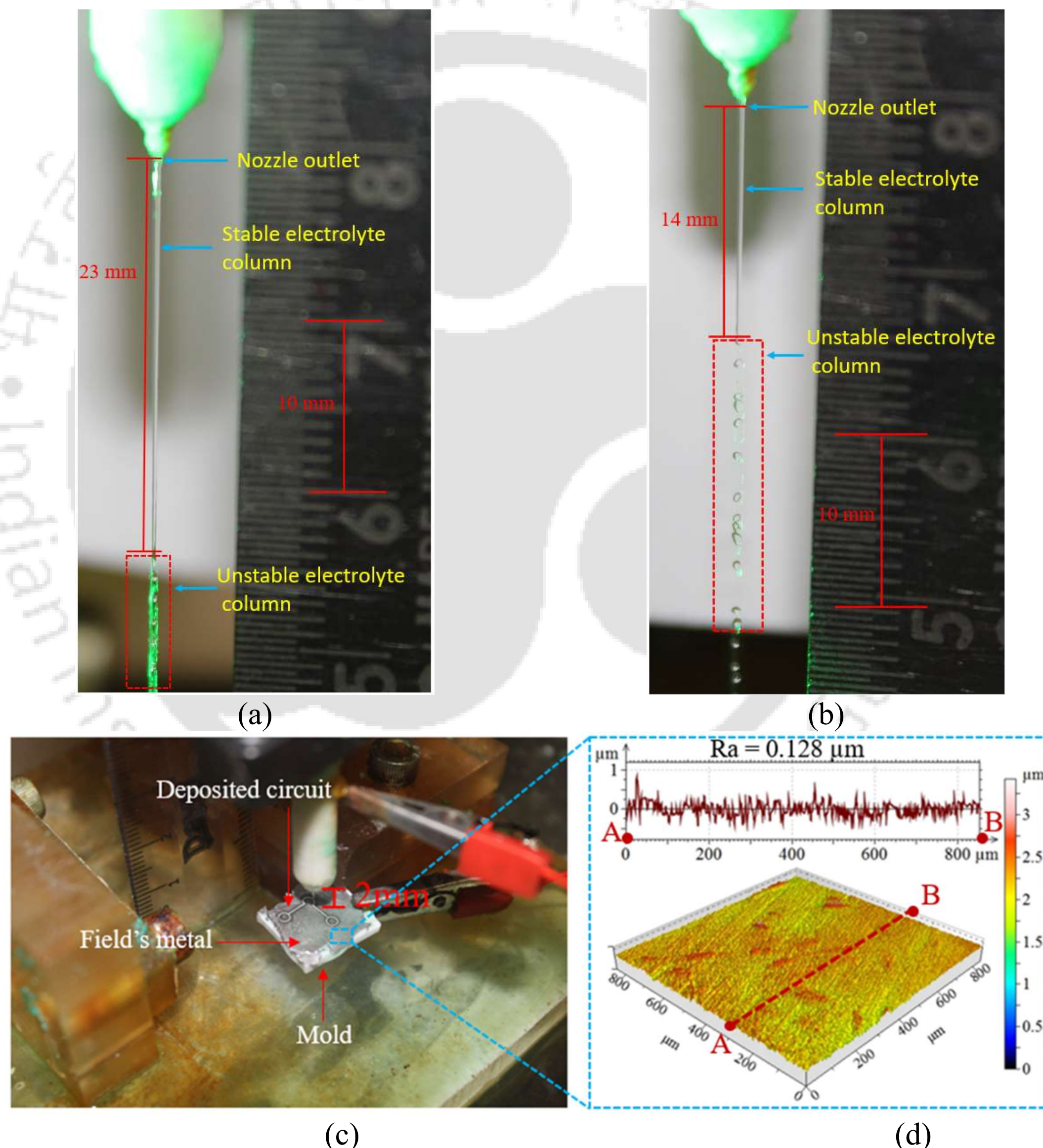

Fig. 4.2 Electrolyte columns formed with nozzle diameters of (a) 250 µm and (b) 500 µm; (c) Deposition process on substrate surface at 2 mm distance below nozzle, and (d) measured surface roughness of substrate surface

TH-3378_196103004

Experimentally, the stable electrolyte column lengths corresponding to 250 μm and 500 μm nozzle diameters are measured to be 23 mm and 14 mm, respectively, as shown in Fig. 4.2(a) and Fig. 4.2(b). The stable electrolyte column length is found to be getting reduced with increased nozzle diameter due to the reduction of the jet's outlet velocity. Experimental observations indicate that no oscillation phenomena are observed at the interface between electrolyte and air up to a certain stable column length. However, beyond this stable column length, the electrolyte column becomes unstable, leading to the dissociation of the column into tiny droplets. This instability and dissociation of the electrolyte column can be attributed to various factors, including fluid dynamics, surface tension effects, and interactions between the electrolyte and air. As the column length exceeds the stable range, the forces acting on the electrolyte become unbalanced, causing disturbances and breaking the column into droplets [66]. Hence, the region beyond the stable column length is avoided while maintaining a controlled deposition process. Therefore, all experiments are conducted with an initial electrolyte column distance of 2 mm from the substrate surface to enhance interaction and localization, as shown in Fig. 4.2(c). The surface roughness of the prepared substrate (Section 3.3.1) is 0.128 μm as shown in Fig. 4.2(d), hence further polishing is not required.

4.2.3.2 Effect of nozzle diameter on layer height and width

To observe the effect of the nozzle opening diameter, two different nozzles with specific opening diameters of 250 and 500 μm were fabricated using a capillary glass tube. The depositions corresponding to nozzle diameters of 250 and 500 μm are performed by depositing a 3 mm length long bead with 224 layers, as shown in Fig. 4.11(a) and Fig. 4.3 (a), respectively. Both depositions' applied voltage and scanning speed are kept fixed at 15 V and 80 mm/min, respectively. The deposition width and total height corresponding to 500 μm nozzle diameter are measured as 850 μm and 8.70 μm, respectively, as shown in Fig. 4.3(b). For 250 μm nozzle diameter, the total layer height and width are 28.6 μm and 570 μm, respectively, as shown in Fig. 4.11(c). It is concluded from the above analysis that the total layer height decreases and layer width increases while the nozzle diameter increases. It is because when the nozzle diameter of the jet is increased, the reaction area also increases, causing the width to expand and the total layer height to decrease. The surface corresponding to the 500 μm diameter nozzle is found to be more uniform than the 250 μm as shown in the 3D profilometer images of the deposits (Fig. 4.3(b) and Fig.

TH-3378_196103004

4.11(b)). Since the objective of the present study is to obtain the lower deposition width, the nozzle with 250 µm opening diameter is selected for further study. These observations show that the deposition width can be decreased using a smaller nozzle diameter based on the requirement.

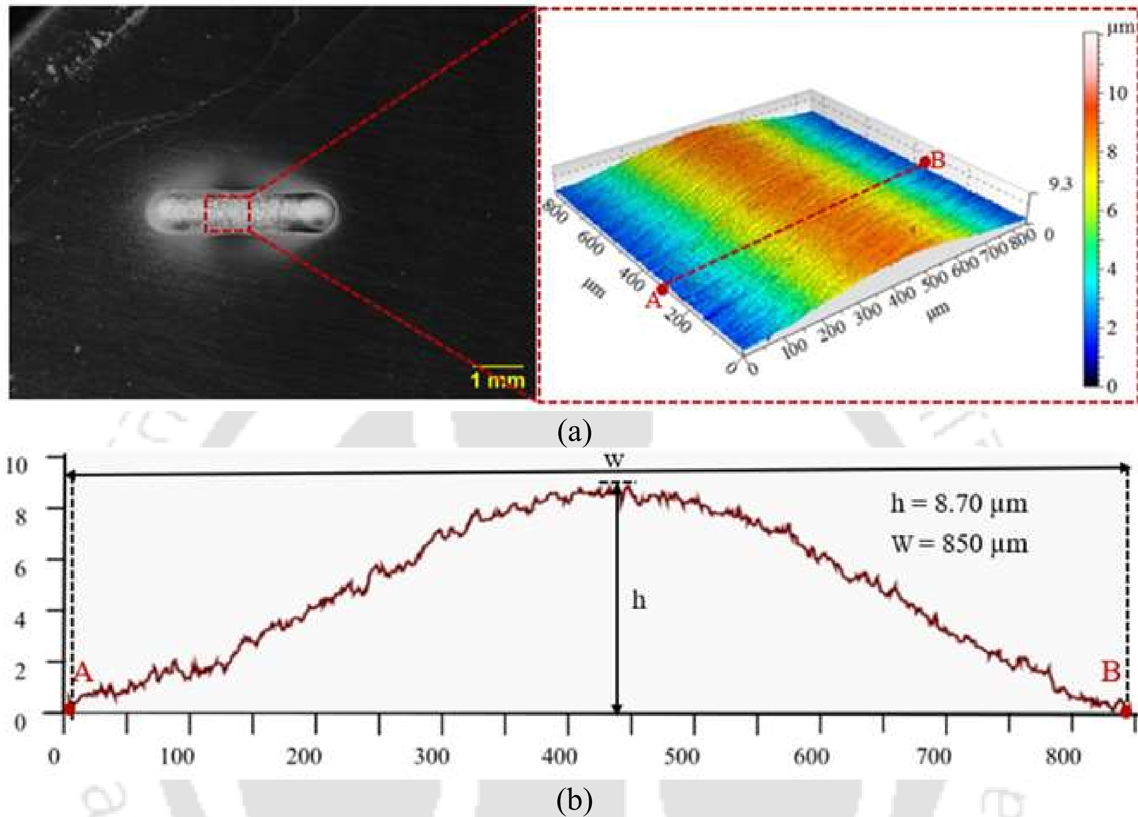

Fig. 4.3 (a) Deposited bead and 3D morphology at a particular location, and (b) 2D profilometer image at 15 V and 80 mm/min scanning speed with 500 µm nozzle diameter

4.2.3.3 Effect of applied voltage on layer height and width

The effect of applied voltage on the total layer height (h) and width (w) is investigated by depositing a 3 mm long bead with 224 layers. The experiments are conducted with a fixed scanning speed of 100 mm/min, while the applied voltage is varied between 10 V and 20 V. The deposited beads corresponding to 10 V, 15 V, and 20 V are shown in Fig. 4.4(a), Fig. 4.5(a), and Fig. 4.6(a), respectively. The deposited beads' total layer height and width corresponding to 10 V, 15 V, and 20 V are shown in Fig. 4.4(d), Fig. 4.5(d), and Fig. 4.6(d), respectively. It is found that the total layer height and width increase with increased voltage. Also, for every 5 V rise in applied voltage, the total layer height nearly increases by 10 µm, while the layer width increases by almost 100 µm, as depicted in Fig. 4.8(a). It is because the current density value increases with the increment in applied voltage (Fig.

TH-3378_196103004

4.7(d)); hence, the deposition rate also increases, causing an increment in total layer height and width. At the time of power-on, the initial current is measured using a digital multimeter connected in series between the substrate and the anode. The measured current values corresponding to 10 V, 15 V, and 20 V are shown in Fig. 4.7(a), Fig. 4.7(b), and Fig. 4.7(c), respectively. It is observed that the value of the current increases with an increase in voltage. The increased applied voltage also leads to an increase in the size of the nodules [68], [71], as observed in the FESEM images of the deposited bead surfaces (Fig. 4.4(c), Fig. 4.5(c), and Fig. 4.6(c)). In addition, a rise in voltage causes the entire deposited layer to grow in a cellular manner, which is followed by larger grain size, increased surface roughness, decreased density, and worsened surface flatness, as observed in the surface morphology analysis by 3D profilometer (Fig. 4.4(b), Fig. 4.5(b), and Fig. 4.6(b)). At higher voltage, the concentration polarization phenomenon becomes more significant. Hence, the deposition process is primarily controlled by diffusion, and the reactive ions are more likely to reach and deposit onto small surface protrusions [68].

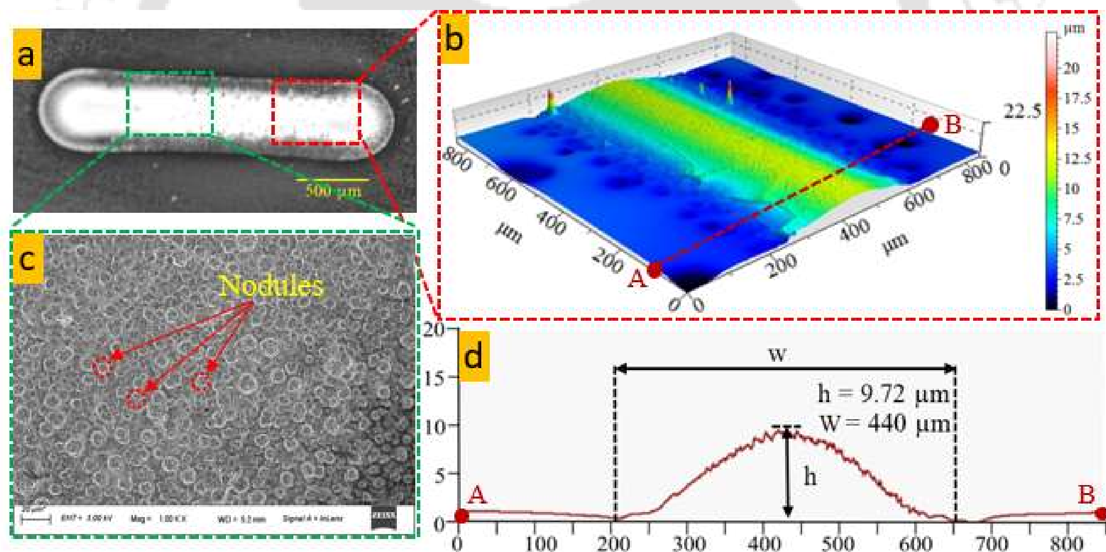

Fig. 4.4 (a) Deposited bead and its (b) 3D morphology, (c) FESEM image at a particular location, and (d) 2D profilometer image at 10 V applied voltage and 100 mm/min scanning speed

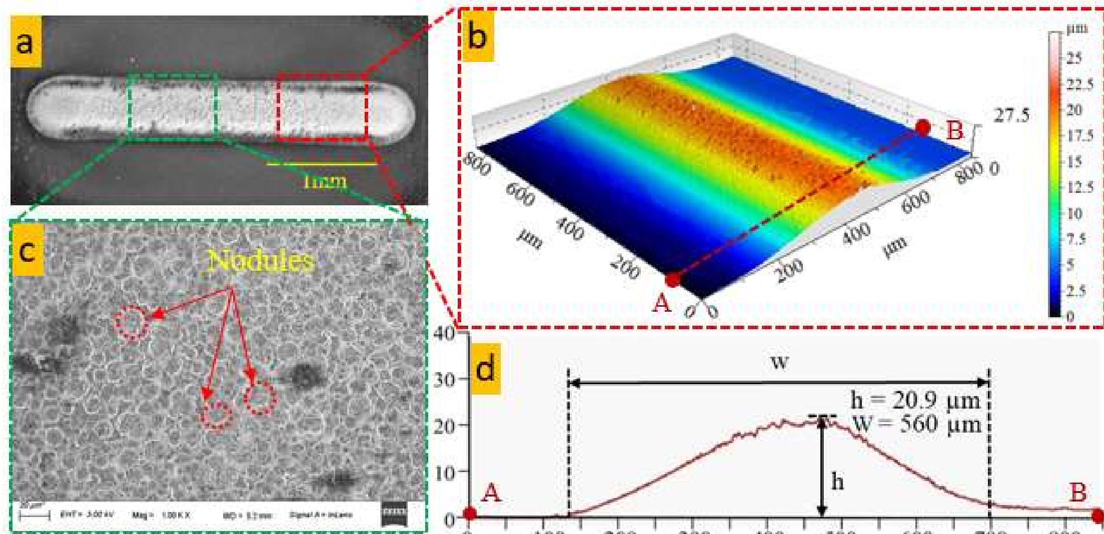

Fig. 4.5 (a) Deposited bead and its (b) 3D morphology, (c) FESEM image at a particular location, and (d) 2D profilometer image at 15 V applied voltage and 100 mm/min scanning speed

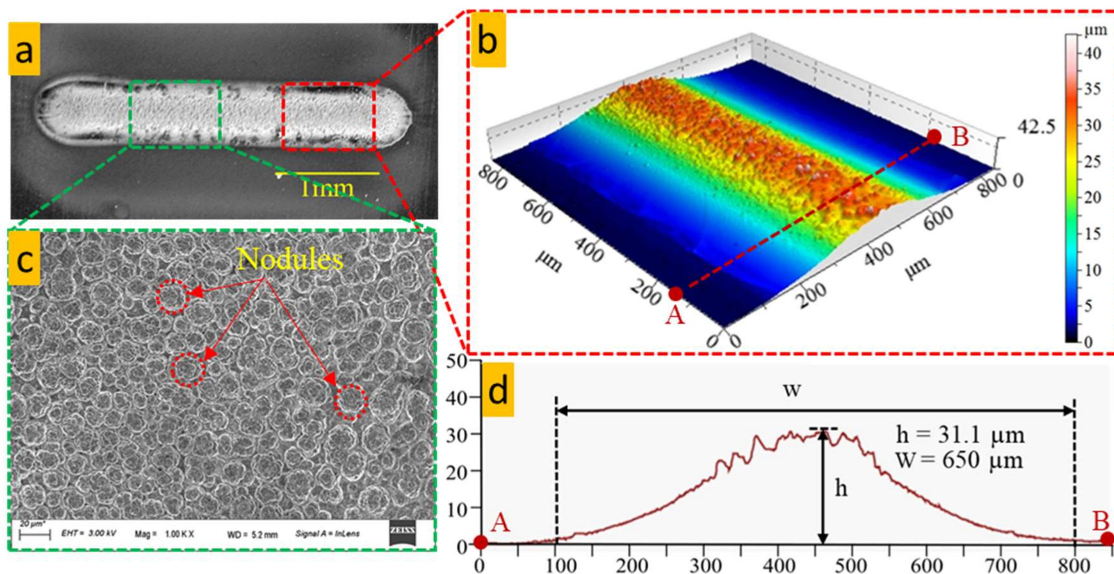

Fig. 4.6 (a) Deposited bead and its (b) 3D morphology, (c) FESEM image at a particular location, and (d) 2D profilometer image at 20 V applied voltage and 100 mm/min scanning speed

TH-3378_196103004

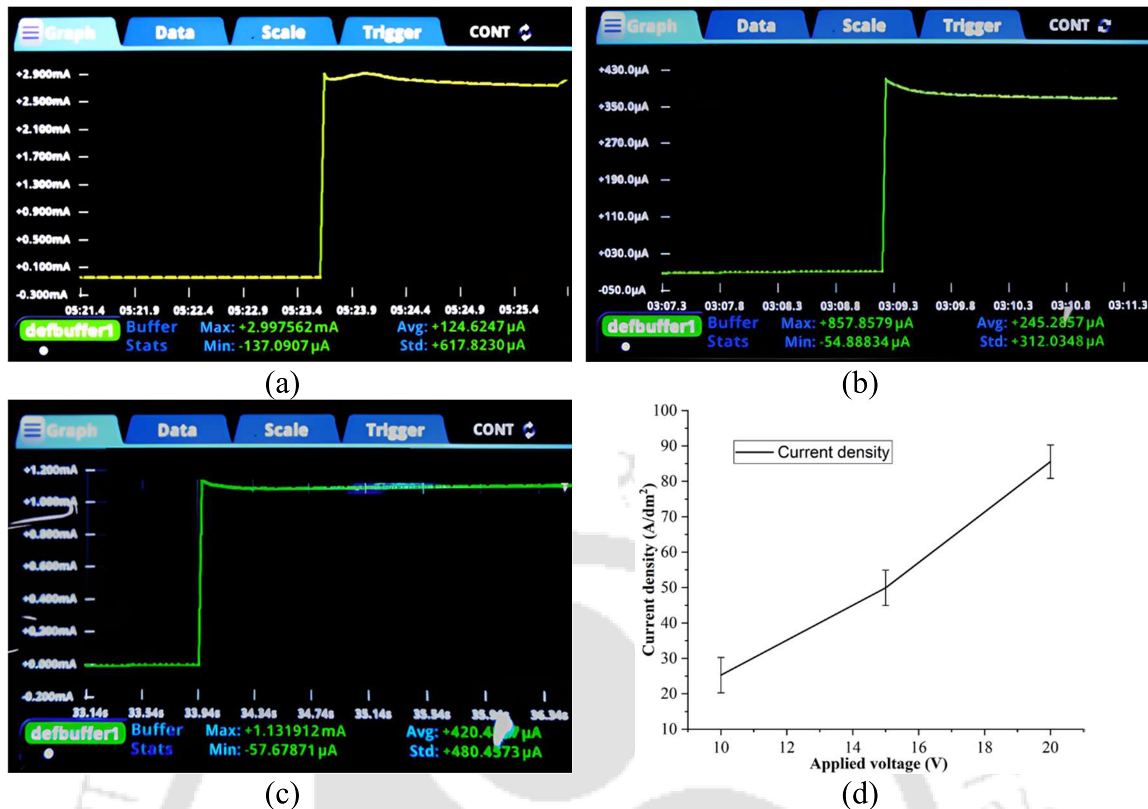

Fig. 4.7 Initial measured value of current at (a) 10 V, (b) 15 V, (c) 20 V applied voltage; (d) Current density measured at different applied voltages

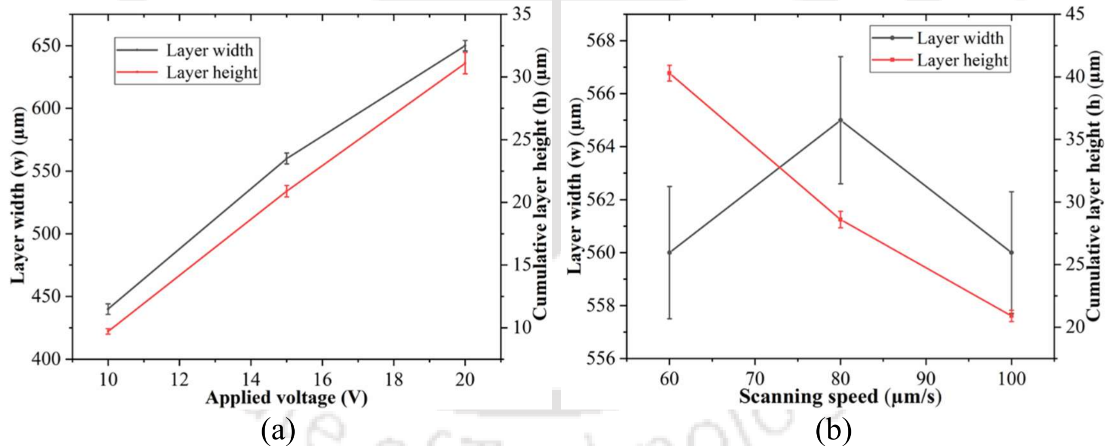

Fig. 4.8 Effect of (a) applied voltage and (b) scanning speed on total layer height and width

The above analysis can be observed clearly when a 3D structure of 3 mm height is deposited corresponding to each above-discussed parameter, as shown in Fig. 4.9(a), Fig. 4.9(b), and Fig. 4.9(c). It is found that above 15V applied voltage (Fig. 4.9(c)), instead of a wall formation, a series of pillars of different shapes are deposited. As the voltage increases, the size of the nodules also increases. The small protrusions from the previous layer experience less electrical resistance as the electrolyte jet becomes shorter.

Consequently, these protrusions grow at a faster rate than other nodules, leading to the formation of pillars.

From the above discussion, it is observed that a minimum value of deposition voltage should be chosen for smooth deposition and lower layer width. It is also noticed that the total layer height also starts decreasing by nearly 10 µm for each 5 V reduction in applied voltage, leading to a lesser production rate. Therefore, an applied voltage of 15V is selected for further investigation as it provides intermediate results between the cases with 10 V and 20 V.

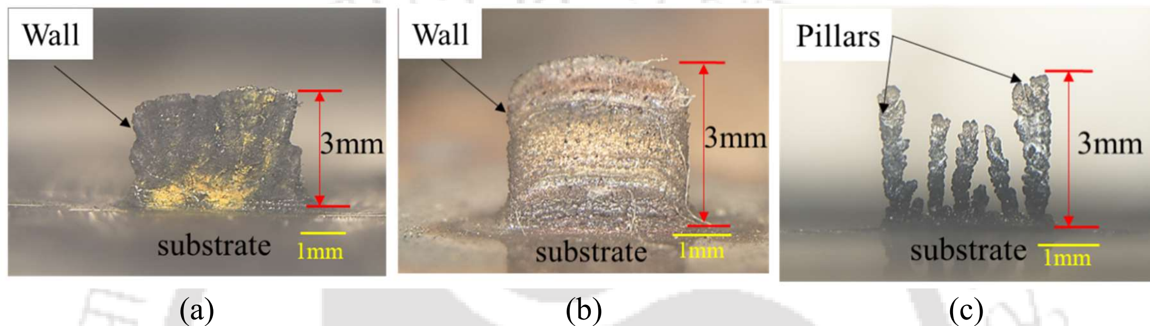

(a) (b) (c)

Fig. 4.9 Deposited 3D structures at (a) 10 V, (b) 15 V, and (c) 20 V applied voltages with 100 mm/min scanning speed

4.2.3.4 Effect of scanning speed on layer height and width

The effect of scanning speed on total layer height (h) and width (w) is studied by depositing a 3 mm bead with 224 layers. The experiments are conducted with a fixed applied voltage of 15 V, while the scanning speed is varied between 60 to 100 mm/min. The deposited beads corresponding to 60, 80, and 100 mm/min are shown in Fig. 4.10(a), Fig. 4.11(a), and Fig. 4.5(a), respectively. The deposited beads' total layer heights and widths correspond to 60, 80, and 100 mm/min scanning speeds are shown in Fig. 4.10(d), Fig. 4.11(d), and Fig. 4.5(d), respectively. It is observed that the variation in layer widths of the depositions is almost negligible with increased scanning speed. However, it is observed that as the scanning speed increases, the layer height decreases. This can be attributed to the reduced reaction time between the electrolyte jet and the substrate for the same deposition layer at higher scanning speeds. For each 20 mm/min increase in scanning speed, there is a decrease of approximately 10 µm in the total layer heights, as shown in Fig. 4.8(b).

The increased scanning speed also leads to a decrease in the size of the nodule [90], as observed in the FESEM images of the deposited bead surfaces (Fig. 4.10(c), Fig. 4.11(c), and Fig. 4.5(c)). At lower scanning speeds, the longer current duration at a particular

TH-3378_196103004

position beneath the jet allows for the full growth of grains, resulting in larger and more distinct cellular structures with clear boundaries. As the scanning speed increases, the reduced current action time limits grain growth, resulting in smaller grains. Additionally, the increased number of scanning areas at higher scanning speed promotes grain refinement, leading to lower surface roughness, as observed in surface morphology images by a 3D profilometer (Fig. 4.10(b), Fig. 4.11(b), and Fig. 4.5(b)).

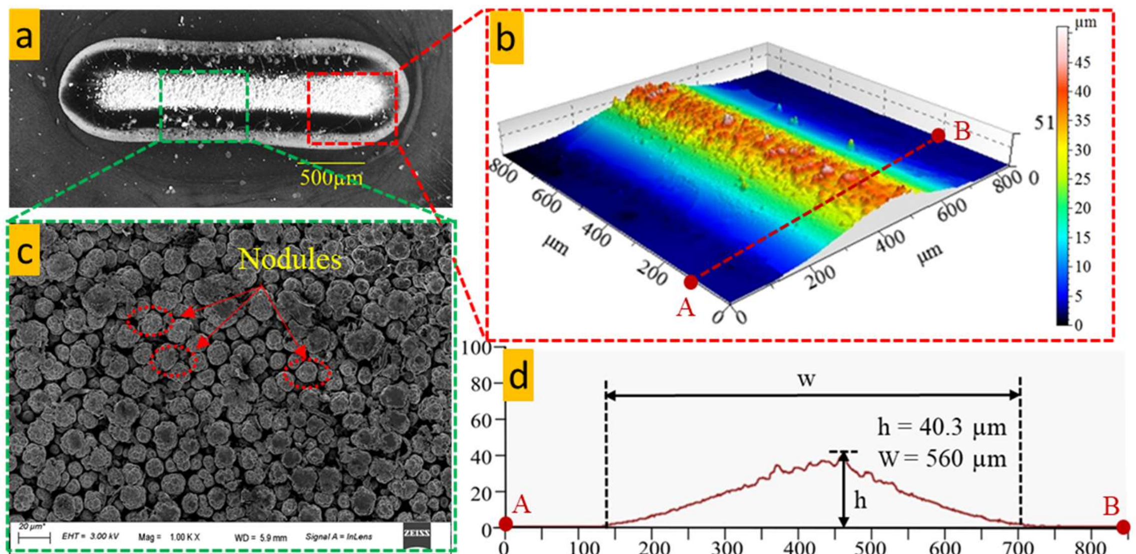

Fig. 4.10 (a) Deposited bead and its (b) 3D morphology, (c) FESEM image at a particular location, and (d) 2D profilometer image at 60 mm/min scanning speed for 15 V applied voltage

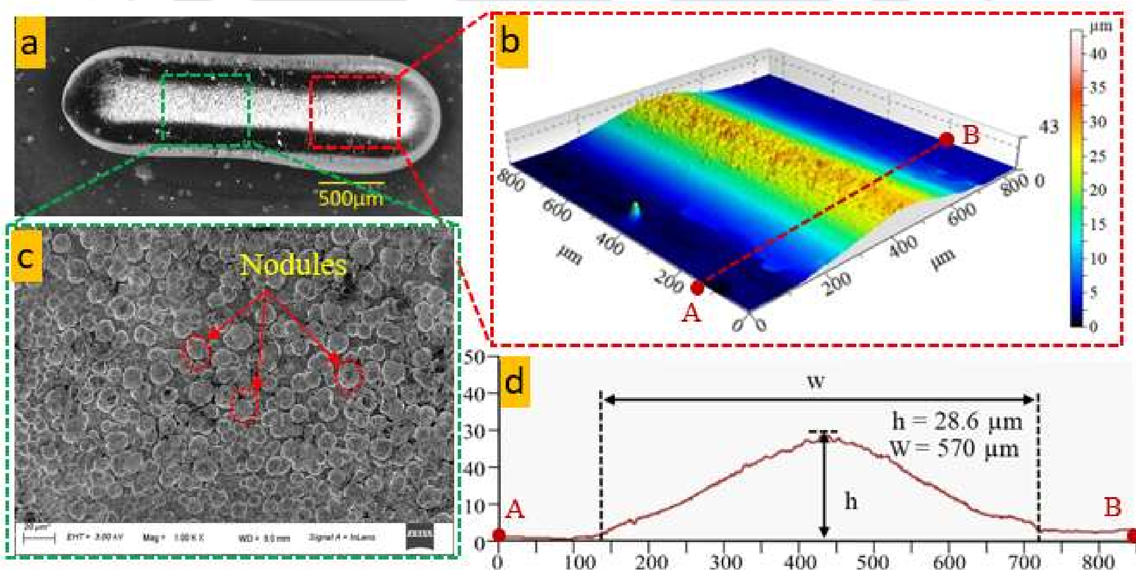

Fig. 4.11 (a) Deposited bead and its (b) 3D morphology, (c) FESEM image at a particular location, and (d) 2D profilometer image at 80 mm/min scanning speed for 15 V applied voltage

TH-3378_196103004

The above analysis can be observed clearly when a 3D structure of 3 mm height is deposited corresponding to each above-discussed parameter, as shown in Fig. 4.12(a), Fig. 4.12(b), and Fig. 4.9(b). It was found that with a scanning speed below 80 mm/min, instead of a wall formation, a series of pillars of different shapes were deposited due to the abovementioned reasons. From the above discussion, it can be concluded that the higher scanning speed gives uniform surface morphology; hence, for further study, the scanning speed of 100 mm/min is selected.

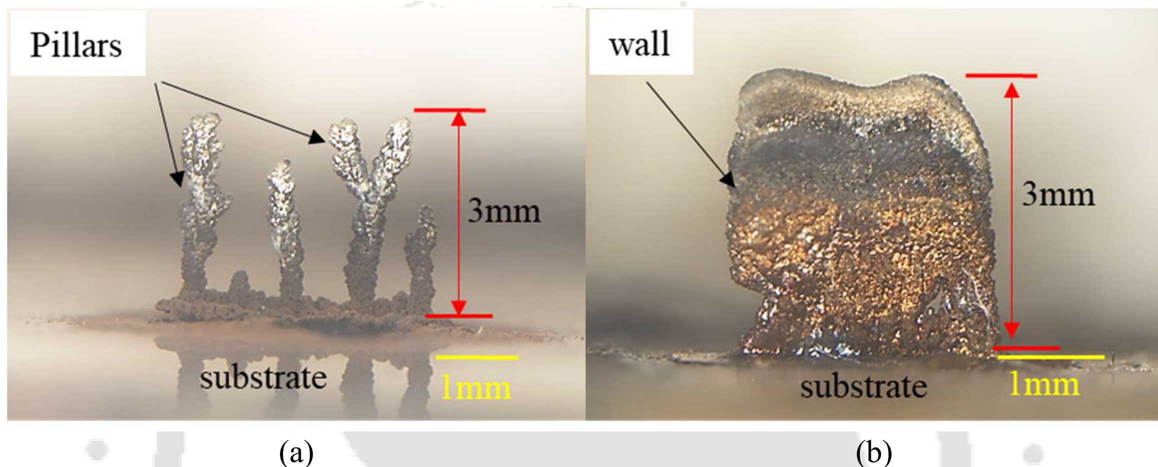

(a) (b)

Fig. 4.12 Deposited 3D structures at (a) 60 and (b) 80 mm/min scanning speeds with 15V applied voltage

4.2.3.5 Surface characterization of deposit

The microhardness and energy-dispersive X-ray (EDX) characterization of the deposited wall (Fig. 4.9(b), fabricated at 15 V applied voltage and 100 mm/min scanning speed) are conducted. A Vickers microhardness tester (HVS-1000A) with a load of 300 N and a dwell time of 20 seconds is utilized to perform the microhardness test. The space between two indentations was kept at least 2.5 times higher than the diagonal size of the indented spot to avoid residual stress affecting the measurement of nearby indentations, as shown in Fig. 4.13(a). The average microhardness value of the wall is found to be 416 HV. Fig. 4.13(b) displays the EDX analysis result of the deposited wall. Nickel is present in the highest concentration (91.24%), followed by carbon (6.34%) and oxygen (2.42%). The presence of small amounts of carbon and oxygen is due to their absorption from the environment.

Further, the adhesion resistance of the deposited structure is measured with a scratch tester on two multilayer beads (i.e., sample 1 and 2) deposited on the substrates (i.e., Field's metal) at 15V applied voltage and 100 mm/min scanning speed along the direction of the deposit, as shown in Fig. 4.14. The scratch length (i.e., stroke) of 3 mm and the scratch

TH-3378_196103004

speed of 30 mm/min are considered on two samples to check the results' repeatability using an indenter with a conical tip with a radius of 200 µm and cone angle of 120°. A constant normal load of 100 N is applied for all tests [110], [111]. The variation of the traction force with the stroke length is depicted in Fig. 4.14 for samples 1 and 2. The critical load for delaminating the bead from the substrate is nearly 34 N for both samples. It shows a high strength of adhesion between the bead and substrate. Hence, applying mechanical load to remove the parts from the Field's metal can break or deform the printed parts. Therefore, a novel method for separating micro parts from the substrate is developed in the present study, as described previously in Section 3.3.1.

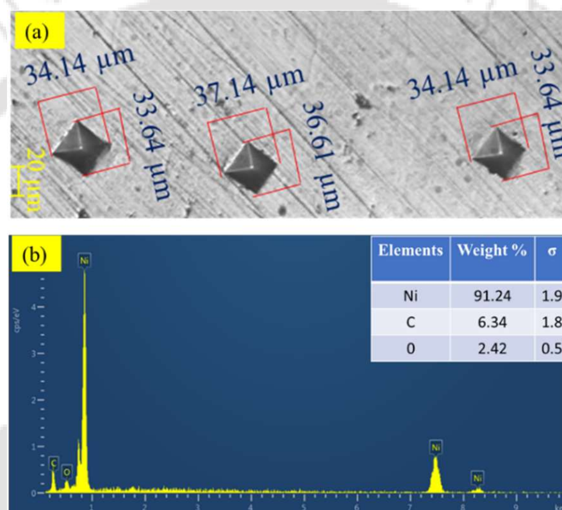

Fig. 4.13 Surface characterization (a) microhardness and (b) EDX analyses of deposited wall (Fig. 4.9(b), fabricated at 15 V applied voltage and 100 mm/min scanning speed)

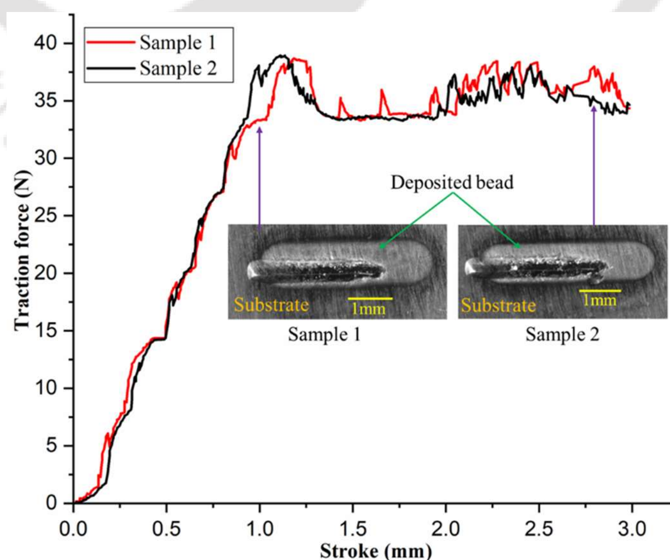

Fig. 4.14 Variation of traction force with stroke on samples 1 and 2 during scratch test

TH-3378_196103004

4.2.4 Multi-bead analysis

The previous discussion is mainly focused on making single beads. However, it did not fully explain the dynamics of material interaction when numerous beads overlapped during the deposition process. In order to optimize the deposition process and achieve the desired surface quality and dimensional accuracy, it is critical to comprehend how these overlapping beads behave. In wire-arc additive manufacturing (WAAM), a model known as a flat-top overlapping model (FOM) [112], [113] is useful in the present context. This model aims to explain how the overlapping of individual beads is related to the quality of the resulting surface. In the present model, a single bead is characterized by its height (h) and width (w), while the adjacent beads have a center distance (d) between them, as depicted in Fig. 4.15. This model considers both valley and overlapping areas between adjacent beads. When the center distance (d) exceeds the width of a single bead (w), there is no overlap between the adjacent beads. However, as the center distance decreases than single bead width (w), the overlapping area increases, and the valley area decreases. At a specific center distance, the overlapping area becomes equal to the valley area, achieving an optimal flat plane surface. If the center distance continues to decrease beyond this point, it leads to an excessive overlap, causing an increase in the thickness of the deposited layer and surface roughness.

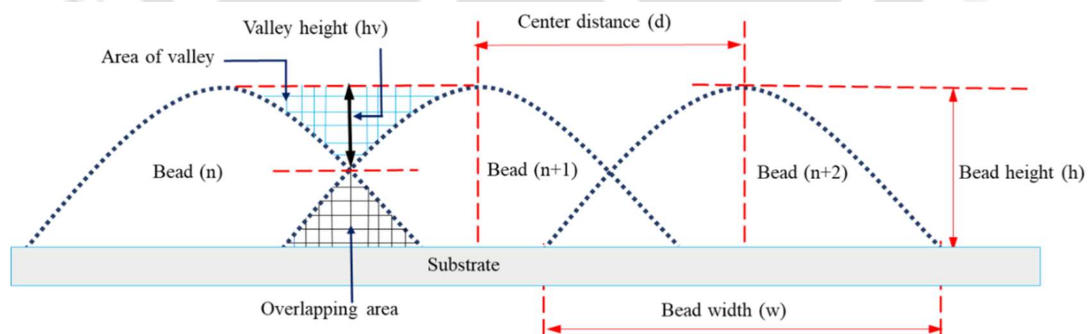

Fig. 4.15 Multi-bead profile of deposits

Due to the limited literature on optimizing multi-bead deposition of the SJED process, it is necessary to prioritize precise control over the spacing between adjacent beads, which is essential for achieving the desired standards of surface quality and surface finish throughout the deposition process. Here, the height of the valley (hv) between adjacent beads is considered an additional criterion for assessing the flatness of multi-bead depositions. A lower valley height indicates a flatter surface. The primary goal of the

TH-3378_196103004

present study is to experimentally achieve a flat surface by reducing the valley height through controlled adjustments in the center distance (d) between the adjacent beads.

The experimentally obtained multilayer single bead profiles (at 10, 15, and 20 V applied voltages and 100 mm/min scanning speed) are curve fitted as shown in Fig. 4.16(a), Fig. 4.16(b), and Fig. 4.16(c), respectively and are found to be parabolic having goodness of fit values (R^2) of 0.98, 0.93, and 0.84. Among all three curve-fitted profiles (Fig. 4.16), the parabolic profile (Fig. 4.16(a)) obtained at 10V applied voltage exhibits the highest goodness of fit. Hence, this profile is chosen for further study of multi-bead optimization as it offers superior dimensional accuracy, even though it results in a lower total layer height. Hence, further multi-bead investigations are conducted at 10 V applied voltage and 100 mm/min scanning speed.

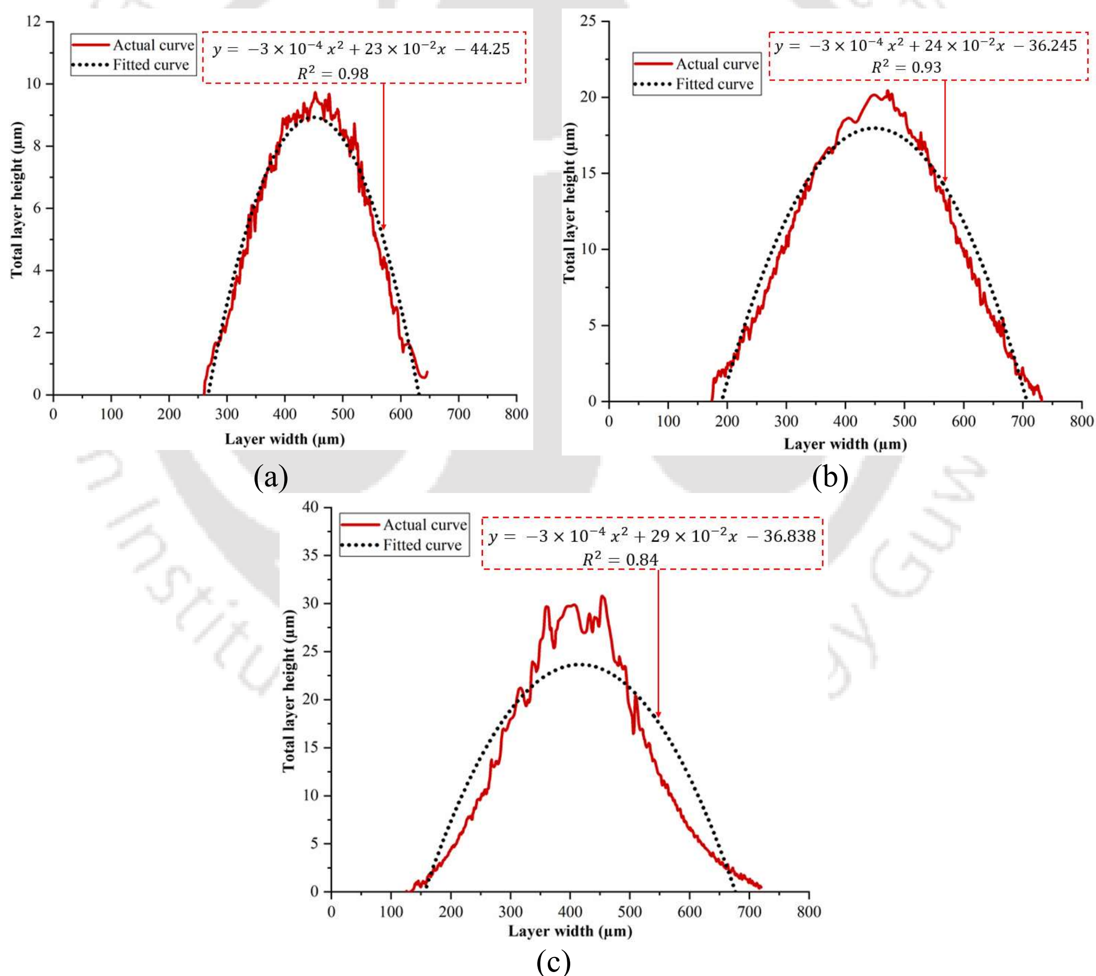

Fig. 4.16 2D profilometer images with fitted curves for (a) 10 V, (b) 15 V, and (c) 20 V applied voltages and 100 mm/min scanning speed

Experiments are conducted considering the overlapping of bead profiles for different center distances (d) in the multi-bead deposition process. Three specific cases were studied

TH-3378_196103004

with center distances of d = 0.70w, d = 0.60w, and d = 0.50w. The corresponding valley heights (hv) of 7.2 μm, 3.3 μm, and 0 μm, respectively, are obtained. Valley height measurements were conducted using 2D profile analysis obtained from a non-contact optical profilometer. The deposited multi-beads, corresponding to the maximum valley height of 7.2 μm at d = 0.70w and the minimum valley height of '0' μm at d = 0.50w, are illustrated in Fig. 4.17(c) and Fig. 4.18(c), respectively. The 3D profile images of these depositions are shown in Fig. 4.17(b) and Fig. 4.18(b), respectively. Based on the analysis of the 2D profile images (Fig. 4.17(c) and Fig. 4.18(c)), it is observed that as the center distance (d) increases, the valley height (hv) also increases. Additionally, when the center distance is set to d = 0.5w, it is considered flat deposition (Fig. 4.18(c)), resulting in a '0' μm valley height, indicating a uniform and flat surface. Based on the above analysis, a center distance of d = 0.5w is chosen for further depositions, which maximizes dimensional accuracy and minimizes voids during the deposition process.

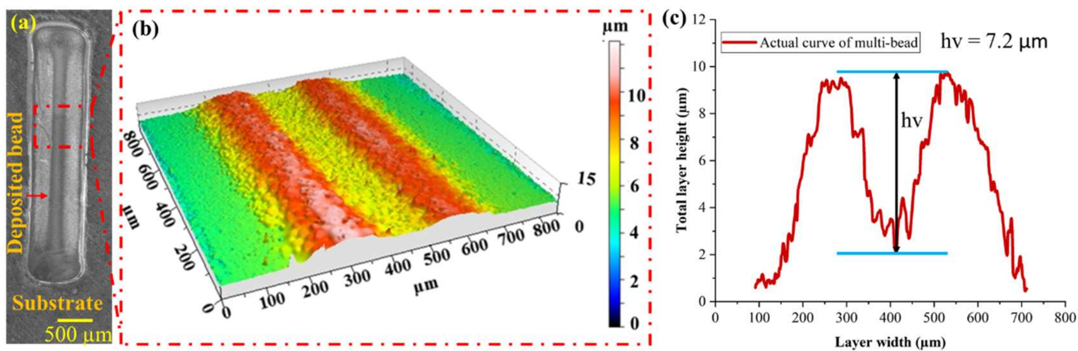

Fig. 4.17 (a) Deposited multi-bead; (b) 3D and (c) 2D profile images at d = 0.7w

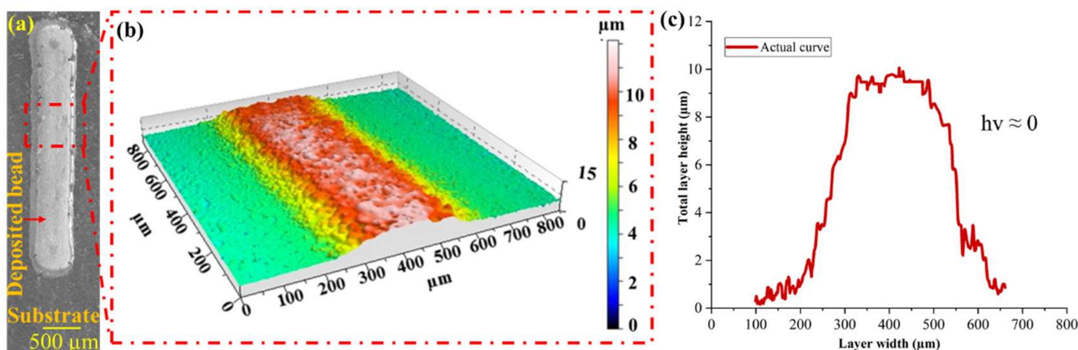

Fig. 4.18 (a) Deposited multi-bead; (b) 3D and (c) 2D profile images at d = 0.5w

4.3 Copper deposition through SJED process

TH-3378_196103004

In this section, the selection of material and the tool for electrodeposition of copper has been discussed. The details about the process parameters for the deposition of a uniform single multilayer bead and the analysis to be performed for the deposited bead have been explained. The experimental analysis for achieving a flat surface condition through multi-bead deposition has been conducted successfully. The optimized center distance between adjacent beads has been determined through experimentation.

4.3.1 Materials and method

The electrolyte used for the deposition of copper typically consists of copper sulfate pentahydrate ($CuSO_4.5H_2O$) at a concentration of 250 g/L and sulfuric acid (H_2SO_4) at a concentration of 75 g/L, dissolved in one liter of distilled water [40]. Each cathode, or substrate, is prepared from a brass sheet having dimensions 20 × 20 × 2 mm^3. The substrate is prepared through a wet grinding process using successive grades of silicon carbide paper, starting with 240 grit, then 400 grit, and finally 1000 grit. The substrates were further polished using a diamond polishing paste, followed by alumina.

4.3.2 Process parameters

The process parameters for this study were determined through a combination of preliminary experiments and a comprehensive literature review. The input variables considered in this study are applied voltage and horizontal scanning speed, as shown in Table 4.3.

Table 4.3 Process parameters and their ranges

Parameters	Ranges
Applied voltage (V)	2.5, 5, 7.5
Scanning speed (mm/min)	100, 125, 150
Nozzle outlet diameter (µm)	250
Standoff distance of jet (mm)	2
Electrolyte flow rate (ml/sec)	0.25

The other parameters, such as nozzle diameter, standoff distance, and electrolyte flow rate, are kept constant. The output responses include total bead height, bead width, and deposition profile. These parameters are crucial for evaluating the quality and dimensional characteristics of the deposited beads. The total bead height refers to the overall thickness of the deposited material, while the bead width represents the lateral extent or width of each

TH-3378_196103004

bead. The deposition profile provides a detailed description of the variation in material distribution across the deposited structure, offering insights into the uniformity and consistency of the deposition process. By analyzing these output responses, one can assess the effectiveness and performance of the electrodeposition process and make informed decisions for process optimization and improvement.

4.3.3 Influence of process parameters on deposition profile/morphology

The influence of various deposition parameters on critical aspects, such as the deposition height, width, and overall morphology of the deposited structure, are discussed below.

4.3.3.1 Impact of process parameters on deposition profile

A series of experiments were conducted to investigate the influence of process parameters on the deposition profile. The study focused on variations in applied voltage and horizontal scanning speed to analyze their impact on the total bead height (h), bead width (w), and overall profile of the deposited structure. In each case, a multilayer bead is deposited. These beads consist of 500 layers with a length of 3 mm. The present study aims to observe and quantify the resulting changes in the deposition profile by systematically changing the process parameters within their predefined range.

In the initial set of experiments, a fixed voltage of 2.5 V was applied, while the scanning speed was varied at 100, 125, and 150 mm/min. Fig. 4.19(a), Fig. 4.20(a), and Fig. 4.21(a) display the deposited beads for scanning speeds of 100, 125, and 150 mm/min, respectively. Fig. 4.19(b), Fig. 4.20(b), and Fig. 4.21(b) represent the 3D profiles of the deposited beads corresponding to the scanning speeds mentioned above. Fig. 4.19(c), Fig. 4.20(c), and Fig. 4.21(c) show the 2D profiles of the deposited beads for the same scanning speeds. The 2D profile images of the beads in Fig. 4.19(c), Fig. 4.20(c), and Fig. 4.21(c) corresponding to scanning speeds of 100, 125, and 150 mm/min, respectively, indicate a decrease in the total bead height as the scanning speed increases. This can be attributed to the reduced reaction time available to deposit metallic ions at higher scanning speeds. With faster scanning speeds, the electrolyte has less time to interact with the substrate, resulting in a lower deposition rate, and, consequently, a thinner bead is formed.

TH-3378_196103004

An insignificant variation in bead width with increased scanning speed is observed. Hence, scanning speed has less influence on deposited bead width than total bead height. Curve fitting analysis was performed on deposited profiles corresponding to 100, 125, and 150 mm/min scanning speed. The analysis revealed that the deposition profiles follow a parabolic shape with high goodness-of-fit, as indicated by R^2 values exceeding 0.97. This shows a strong correlation between the experimental data and the parabolic model, allowing for reliable characterization and prediction of the deposited bead shape.

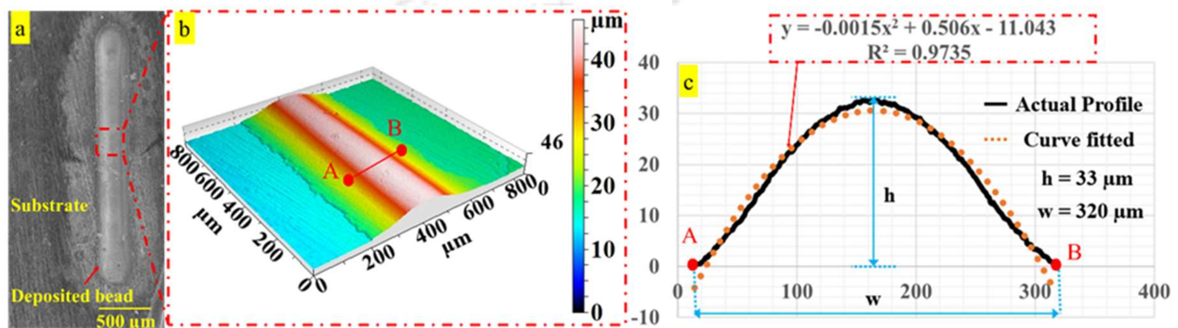

Fig. 4.19 (a) Deposited bead, (b) 3D profile image, and (c) 2D profile image at 100 mm/min scanning speed with 2.5 V applied voltage

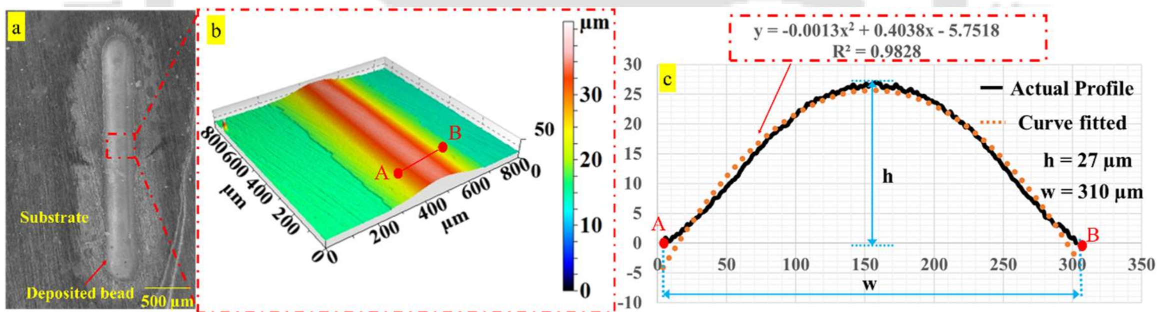

Fig. 4.20 (a) Deposited bead, (b) 3D profile image, and (c) 2D profile image at 125 mm/min scanning speed with 2.5 V applied voltage

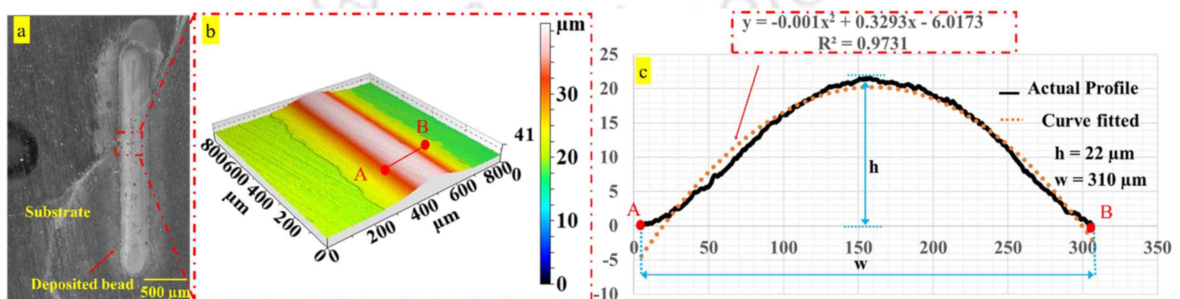

Fig. 4.21 (a) Deposited bead, (b) 3D profile image, and (c) 2D profile image at 150 mm/min scanning speed with 2.5 V applied voltage

The second set of experiments is conducted with a fixed applied voltage of 5 V while varying the scanning speeds, 100, 125, and 150 mm/min, and the deposited beads are shown in Fig. 4.22(a), Fig. 4.23(a), and Fig. 4.24(a), respectively. The corresponding 3D profile images (Fig. 4.22(b), Fig. 4.23(b), and Fig. 4.24(b)) and 2D profile images (Fig. 4.22(c), Fig. 4.23(c), and Fig. 4.24(c)) are shown for these scanning speeds. There is a decrease in the total bead height with increased scanning speed, as observed in Fig. 4.25. This can be attributed to the shorter reaction time and less deposition of metallic ions at higher scanning speeds, as mentioned earlier. The variation in the bead width with the change in scanning speed is insignificant. While comparing the total bead height at the same scanning speed, it's value is lower for 2.5V applied voltage than 5V, as depicted in Fig. 4.25. This indicates that the deposition rate increases with an increase in applied voltage. Also, the curve fitting analysis of the deposited profiles at different scanning speeds (100, 125, and 150 mm/min) was performed, as depicted in Fig. 4.22(c), Fig. 4.23(c), and Fig. 4.24(c), respectively which reveals that the deposition profiles follow a parabolic shape with high goodness-of-fit values exceeding 0.99.

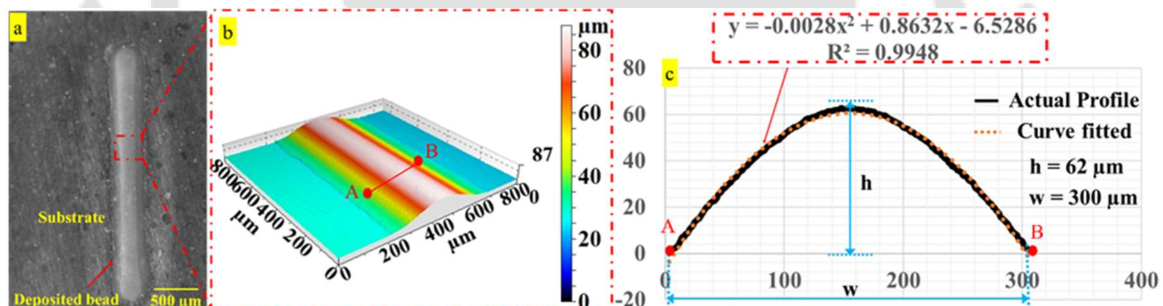

Fig. 4.22 (a) Deposited bead, (b) 3D profile image, and (c) 2D profile image at 100 mm/min scanning speed with 5 V applied voltage

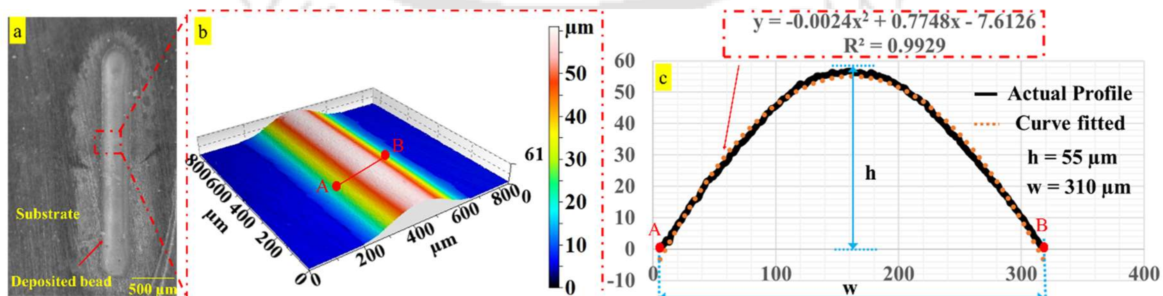

Fig. 4.23 (a) Deposited bead, (b) 3D profile image, and (c) 2D profile image at 125 mm/min scanning speed with 5 V applied voltage

TH-3378_196103004

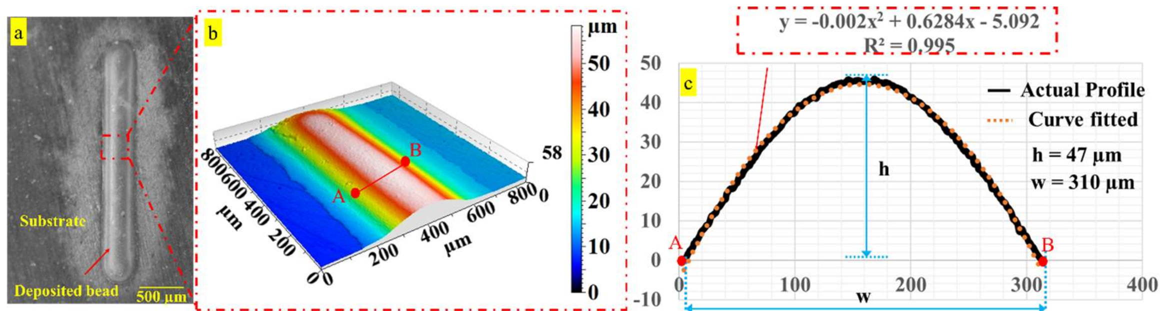

Fig. 4.24 (a) Deposited bead, (b) 3D profile image, and (c) 2D profile image at 150 mm/min scanning speed with 5 V applied voltage

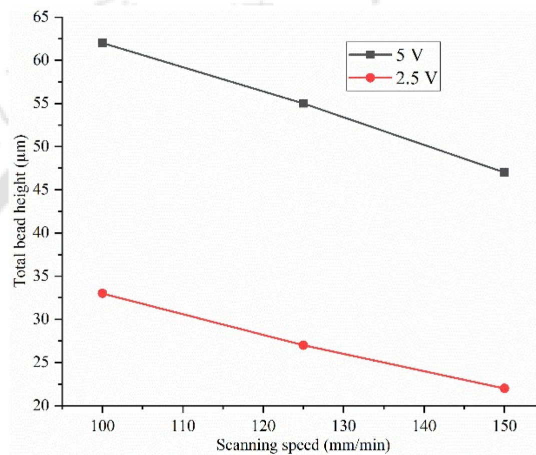

Fig. 4.25 Variation of total bead height with scanning speed at 2.5 V and 5 V

From the above experimentation, it is observed that the total bead height increases with the increased of applied voltage. Hence, the third set of experiments is performed with a fixed applied voltage of 7.5 V while varying the scanning speed (100, 125, and 150 mm/min), and the deposited beads are shown in Fig. 4.26(a), Fig. 4.27(a), and Fig. 4.28(a), respectively. The corresponding 3D profile images are shown in Fig. 4.26(b), Fig. 4.27(b), and Fig. 4.28(b). The corresponding 2D profile images (Fig. 4.26(c), Fig. 4.27(c), and Fig. 4.28(c)) show non-parabolic profiles. The fitted curves of the deposited bead profiles indicate a close fit to a 6th-order polynomial curve. Higher depositions at the sides of the jet than in the middle result in a cup-like structure. Generally, the higher current density is observed at the jet's center than in the middle under higher applied voltage. This intense current density at the jet’s center leads to more vigorous electrochemical reactions and the formation of numerous bubbles, which impede the deposition of metallic ions at the center. As a result, the metal deposition accumulates more at the sides of the jet, forming a cup-like shape. Further, the height of the cup (hc) decreases as the scanning speed increases, as depicted in Fig. 4.26(c), Fig. 4.27(c), and Fig. 4.28(c)) due to the reduced chemical reaction

TH-3378_196103004

time available at a specific point on the substrate surface at higher scanning speed. Also, the bubbles formed during the reaction are more likely to be swept away due to the higher turbulence caused by the faster scanning speed.

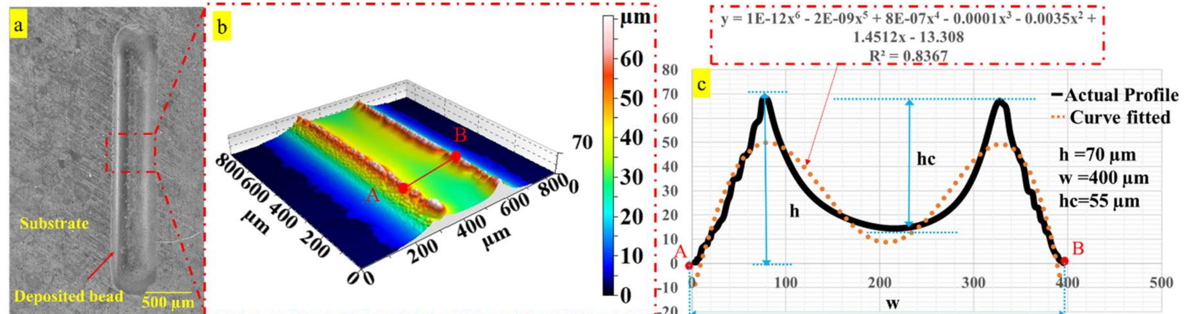

Fig. 4.26 (a) Deposited bead, (b) 3D profile image, and (c) 2D profile image at 100 mm/min scanning speed with 7.5 V applied voltage

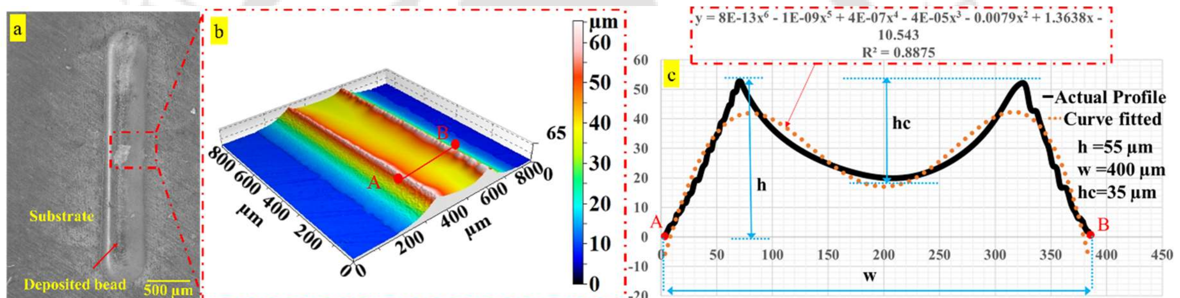

Fig. 4.27 (a) Deposited bead, (b) 3D profile image, and (c) 2D profile image at 125 mm/min scanning speed with 7.5 V applied voltage

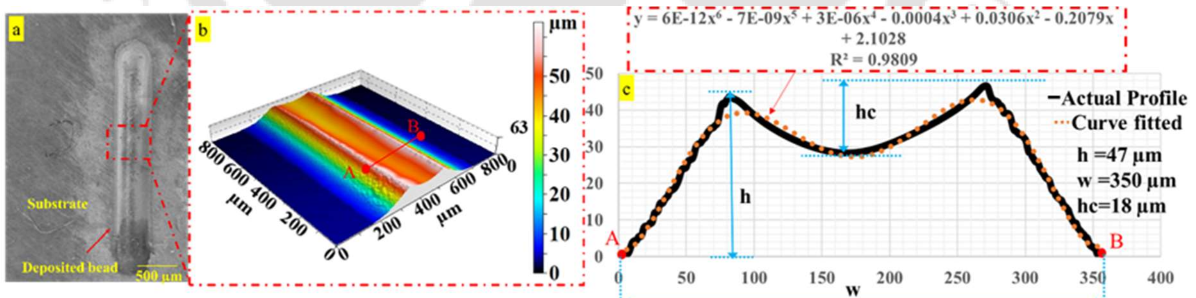

Fig. 4.28 (a) Deposited bead, (b) 3D profile image, and (c) 2D profile image at 150 mm/min scanning speed with 7.5 V applied voltage

Based on the above observations, it can be concluded that an increase in applied voltage leads to an increased deposition height. The deposition profile maintains a parabolic shape up to 5V, indicating a consistent deposition pattern. However, at 7.5 V, the deposition profile undergoes a significant change, deviating from the parabolic shape. This change is attributed to the intense current density and the formation of large bubbles, which affect

the deposition process. These findings highlight the importance of optimizing the deposition parameters, such as voltage and scanning speed, to ensure desired surface quality and dimensional accuracy. Further investigation is recommended to better understand and control the deposition process at higher voltages. The deposited multi-bead at 5V applied voltage and 100 mm/min scanning speed with a bead width (w) of 300 µm, as shown in Fig. 4.22(c), is used for further multi-bead optimization. This parameter configuration has demonstrated a parabolic profile with the highest deposition height among all the parameters studied.

4.3.3.2 Multi-bead optimization

This study focuses on minimizing surface roughness and improving the dimensional accuracy of the deposited beads in SJED. Hence, the cross-sectional profile of the bead becomes a critical factor. Single-bead formation was primarily studied in the previous section and does not explain the behavior of overlapping material in a multi-bead deposition. Understanding the interaction and behavior of multiple beads is essential for optimizing the deposition process and achieving the desired surface quality and dimensional accuracy. The main objective of this study is to achieve a flat surface by experimentally minimizing the height of the valley through adjustments in the center distance (d) between adjacent beads, as already discussed in Fig. 4.15.

Experimental investigations were made on overlapping bead profiles for different center distances (d). Fig. 4.29(a), Fig. 4.30(a), and Fig. 4.31(a) show the deposited multi-bead corresponding to $d = 0.5w$, $d = 0.65w$, and $d = 0.75w$, respectively. The 3D profile images of the same can be depicted in Fig. 4.29(b), Fig. 4.30(b), and Fig. 4.31(b), respectively. After analyzing 2D profile images in Fig. 4.29(c), Fig. 4.30(c), and Fig. 4.31(c), it is observed that the valley height (hv) increases with increased center distance (d).

For further reducing the valley height (hv) in the overlapping bead profiles, additional experiments are conducted considering center distances (d) below 0.5w. The deposited multi-beads for $d = 0.47w$ and $d = 0.45w$ center distances are shown in Fig. 4.32(a) and Fig. 4.33(a), respectively. The 3D profile images of the same are shown in Fig. 4.32(b) and Fig. 4.33(b). Also, the 2D profile images of the same are shown in Fig. 4.32(c) and Fig. 4.33(c), respectively. The center distance of $d = 0.45w$ results in a negligible valley height (hv), thus providing a flat surface.

TH-3378_196103004

A further experiment on multi-bead deposition is conducted considering d = 0.4w. The deposited multi-bead, 3D, and 2D profile images are shown in Fig. 4.34(a), Fig. 4.34(b), and Fig. 4.34(c), respectively. After analyzing the 2D profilometer image (Fig. 4.34(c)), it is observed that the multi-bead profiles (unlike previous cases) merge and form a single bead (i.e., parabolic profile, which is not a desired deposition surface). The height of this merged bead measures 70 μm, which is greater than the height of a single bead at 5V and 100 mm/min, as observed in Fig. 4.22(c). Hence, subsequently, reducing the center distance below 0.45w increases the bead height without improving/damaging the flatness of the deposited bead surface.

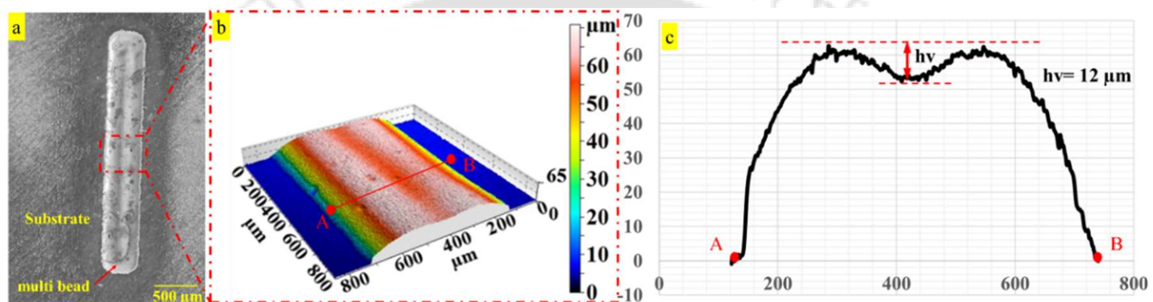

Fig. 4.29 (a) Deposited multi-beads, (b) 3D profile image, and (c) 2D profile image at d = 0.5w

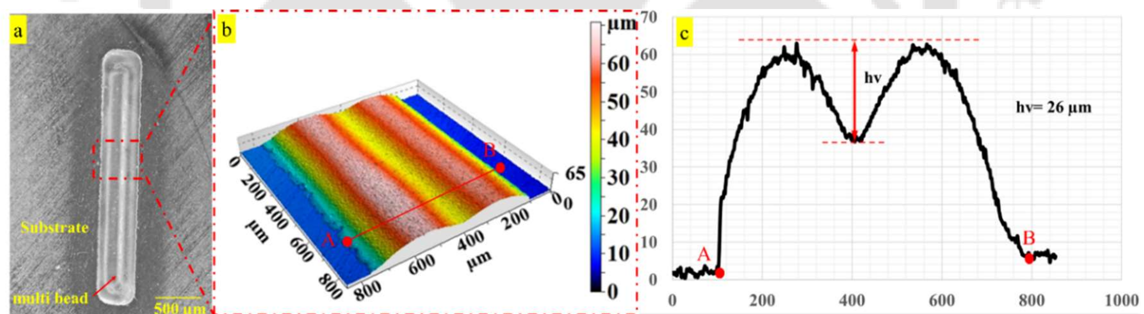

Fig. 4.30 (a) Deposited multi-beads, (b) 3D profile image, and (c) 2D profile image at d = 0.65w

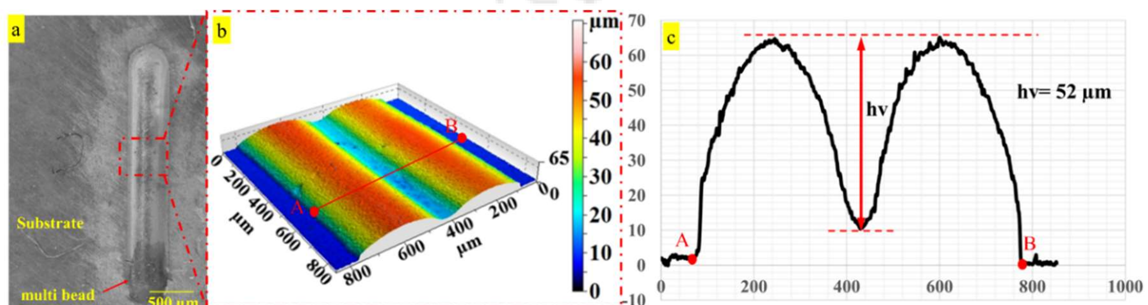

Fig. 4.31 (a) Deposited multi-beads, (b) 3D profile image, and (c) 2D profile image at d = 0.75w

TH-3378_196103004

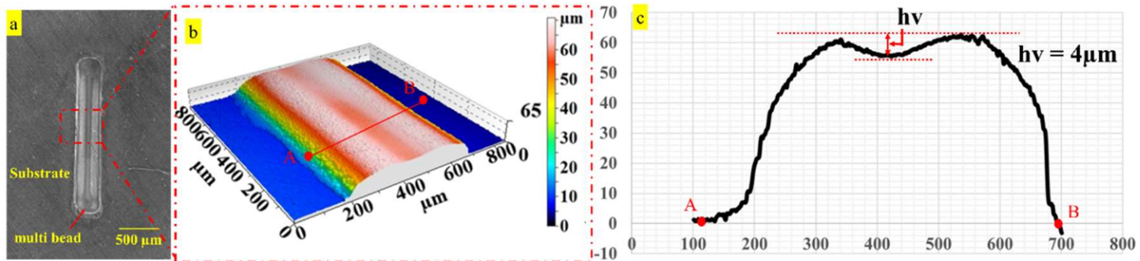

Fig. 4.32 (a) Deposited multi-beads, (b) 3D profile image, and (c) 2D profile image at $d = 0.47w$

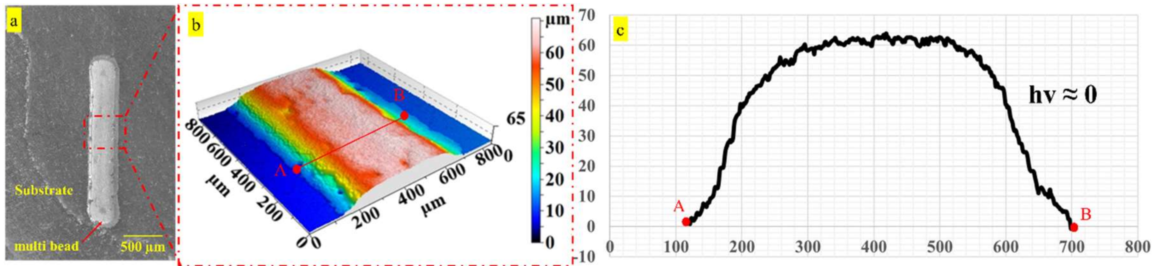

Fig. 4.33 (a) Deposited multi-beads, (b) 3D profile image, and (c) 2D profile image at $d = 0.45w$

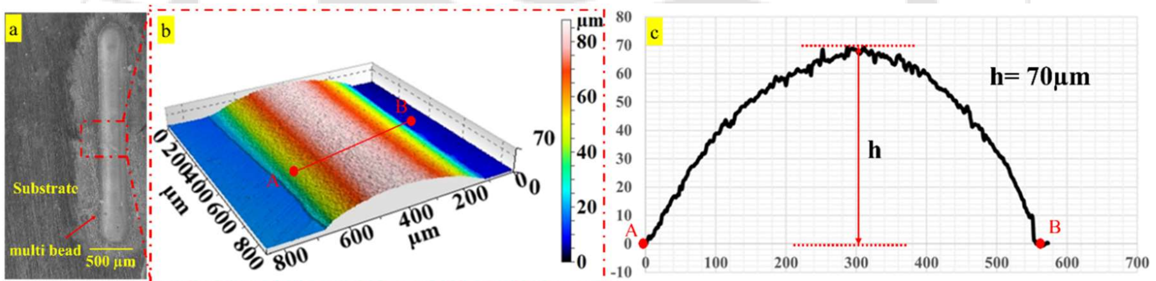

Fig. 4.34 (a) Deposited multi-beads, (b) 3D profile image, and (c) 2D profile image at $d = 0.4w$

Based on the above discussion, it is concluded that a center distance of $d = 0.45w$ provides a negligible valley height (hv), leading to a flatter surface and contributing to a good surface finish. Hence, a center distance of $d = 0.45w$ is selected for further study and tool path planning.

4.3.3.3 Tool path planning

The previous discussion primarily focused on multi-bead optimization, which is relevant to 3D printing. However, when printing a complex 3D part, a tool path strategy is essential. Different tool path strategies can yield varying results in terms of smoothness and dimensional accuracy. Therefore, selecting an appropriate tool path strategy becomes crucial for achieving the desired outcome. This section implements the traveling salesman problem (TSP) tool path algorithm, which can be biased in any user-specified direction. An

TH-3378_196103004

algorithm inspired by the Traveling Salesman Problem (TSP) can create a toolpath that efficiently and precisely fills an area while minimizing retractions and turns [114]. In this study, three different TSP tool path strategies are being explored. Fig. 4.35(a) shows the TSP horizontal biased tool path (84 turns), Fig. 4.35(b) shows the TSP with a circular grid (137 turns), and Fig. 4.35(c) shows the TSP with no biased (150 turns).

A 3×3 mm^2 of the substrate area is deposited corresponding to each tool path to investigate surface smoothness. The deposited areas corresponding to TSP horizontal biased, TSP with circular grid, and TSP with no-biased are shown in Fig. 4.36(a), Fig. 4.37(a), and Fig. 4.38(a), respectively. Based on the analysis in Sections 4.3.3.1 and 4.3.3.2, the selected deposition parameters for each tool path are 5V applied voltage, 100 mm/min scanning speed, and center distance (d) of 0.45w. For each deposited sample, 12 points are considered on the surface of the deposits for measuring surface roughness at two directions, namely transverse direction (i.e., Direction-1) and longitudinal direction (i.e., Direction-2) corresponding to each toolpath.

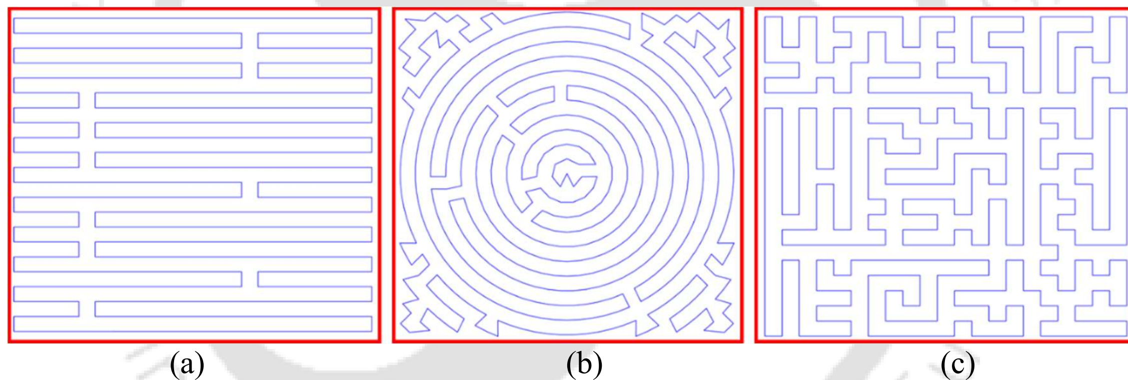

(a) (b) (c)

Fig. 4.35 Tool paths with (a) TSP horizontal biased (84 turns), (b) TSP with circular grid (137 turns), and (c) TSP with no biased (150 turns)

The deposited structure and 3D profilometer image of the deposited surface (3×3 mm^2) corresponding to the TSP horizontal biased toolpath are shown in Fig. 4.36(a) and Fig. 4.36(b), respectively. The surface roughness at considered points in Direction-1 and Direction-2 of the same deposit is shown in Fig. 4.36(c) and Fig. 4.36(d), respectively. The average surface roughness values of the considered points in Directions 1 and 2 are 0.20 and 0.09 μm, respectively, with corresponding standard deviations of 0.10 μm and 0.01 μm, respectively, as shown in Fig. 4.39. Lesser average roughness and standard deviation values are observed in Direction-2 than in Direction-1, as the surface roughness in Direction-2 is less affected by the tool path and number of turns. It can be seen in Fig.

TH-3378_196103004

4.36(d), where surface roughness values are very low with negligible variations in Direction-2, unlike in Direction-1 (Fig. 4.36(c)). The bead is optimized (as discussed in Sections 4.3.3.1 and 4.3.3.2) and other parameters are kept constant. Hence, the deposition in Direction-2 becomes uniform as it mainly follows a straight-line tool path with fewer turns.

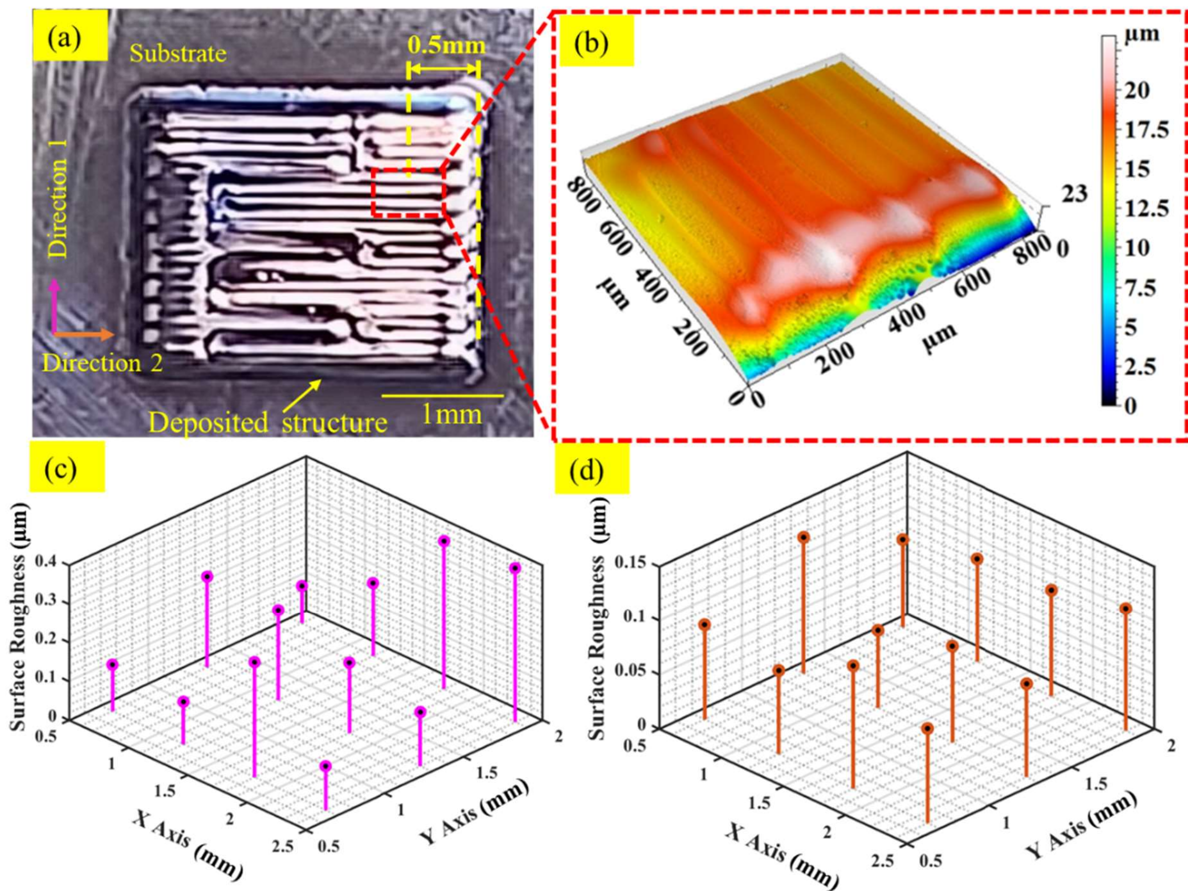

Fig. 4.36 (a) Deposited structure with TSP horizontal biased toolpath, (b) 3D profilometer image, and surface roughness at considered points in (c) Direction-1 and (d) Direction-2

The deposited structure and 3D profilometer images of the deposited surface using the TSP circular grid toolpath are shown in Fig. 4.37(a) and Fig. 4.37(b), respectively. The surface roughness values at the considered points in Direction 1 and 2 on the deposit surfaces are shown in Fig. 4.37(c) and Fig. 4.37(d), respectively. The average surface roughness value of the considered points in Direction-1 measures 0.35 µm and 0.43 µm in Direction-2, with standard deviations of 0.15 µm and 0.18 µm, respectively, as shown in Fig. 4.39. In the previous case (i.e., TSP horizontal biased), the average surface roughness values significantly differed between Directions 1 and 2. However, this difference is insignificant in any of the two directions in the present case, as the tool path is neither

TH-3378_196103004

horizontal nor vertical. Since there are many turns (137 turns) in TSP with circular grid, high surface roughness values are obtained in both Directions 1 and 2.

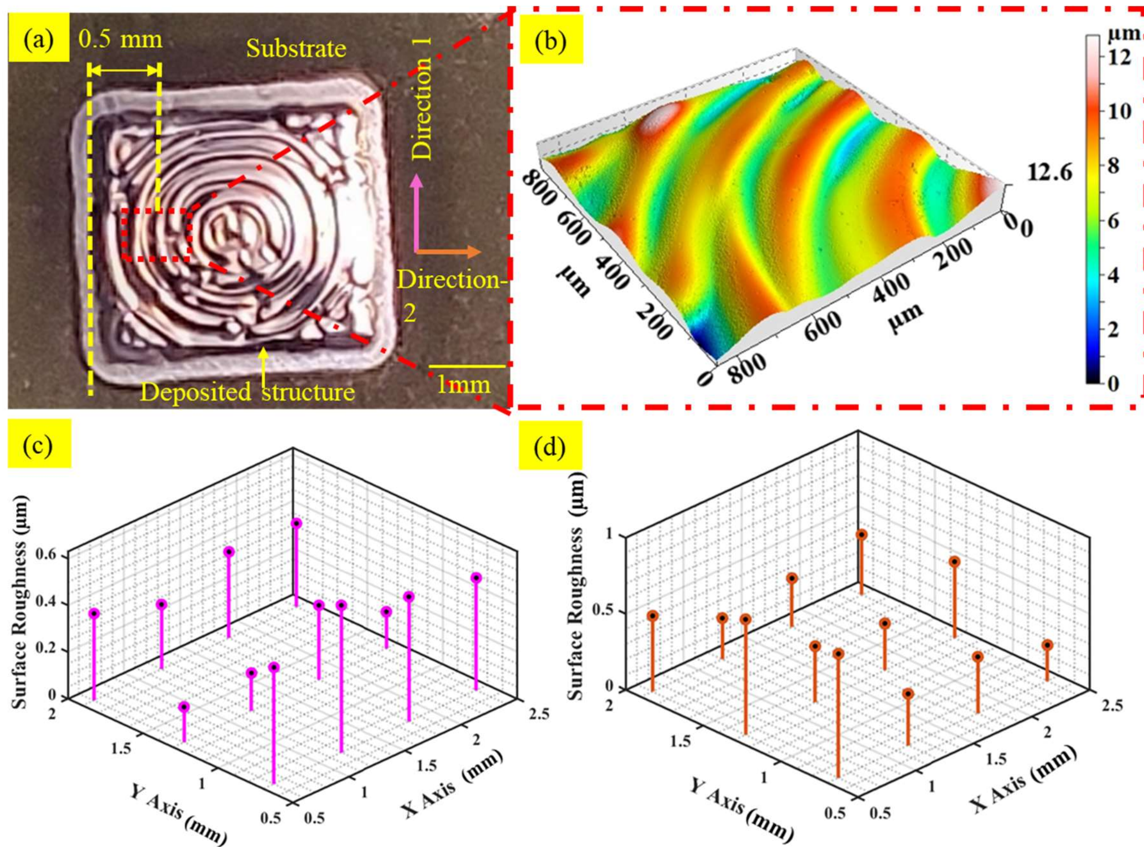

Fig. 4.37 (a) Deposited structure with TSP circular grid toolpath, (b) 3D profilometer image, and surface roughness at considered points in (c) Direction-1 and (d) Direction-2

The deposited structure and 3D profilometer image of the deposited surface corresponding to the TSP with no biased are shown in Fig. 4.38(a) and Fig. 4.38(b), respectively. The surface roughness on the deposited surface at considered points in Directions 1 and 2 are shown in Fig. 4.38(c) and Fig. 4.38(d), respectively, having average surface roughness values of 0.55 µm and 0.56 µm at the considered points with standard deviations of 0.18 µm and 0.17 µm, as shown in Fig. 4.39. Due to the higher number of turns (150) in the present case than in the previous two toolpaths, the highest surface roughness values are observed in both Direction-1 and Direction-2. No significant difference in the average surface roughness values is observed between both directions, as the tool path is not biased in favor of any direction.

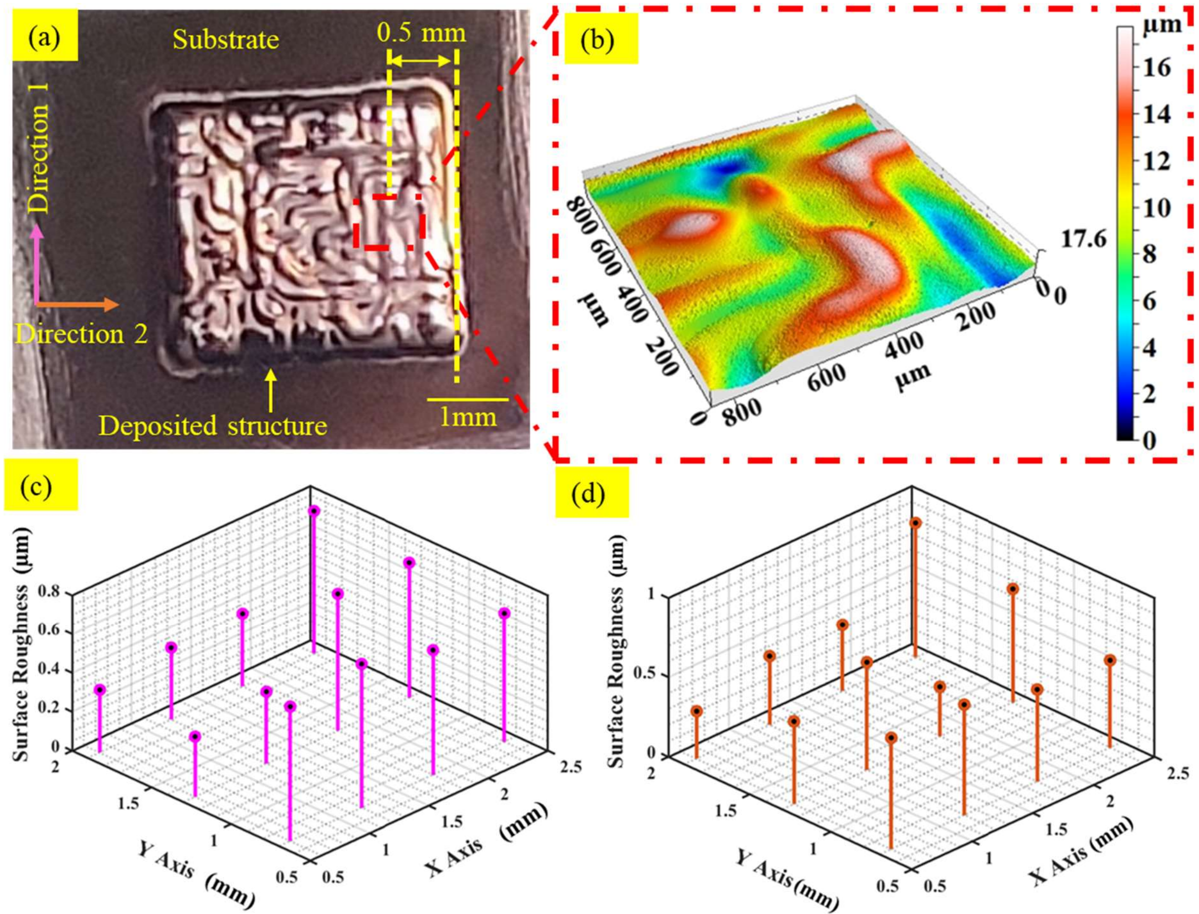

Fig. 4.38 (a) Deposited structure with TSP with no biased toolpath, (b) 3D profilometer image, and surface roughness at considered points in (c) Direction-1 and (d) Direction-2

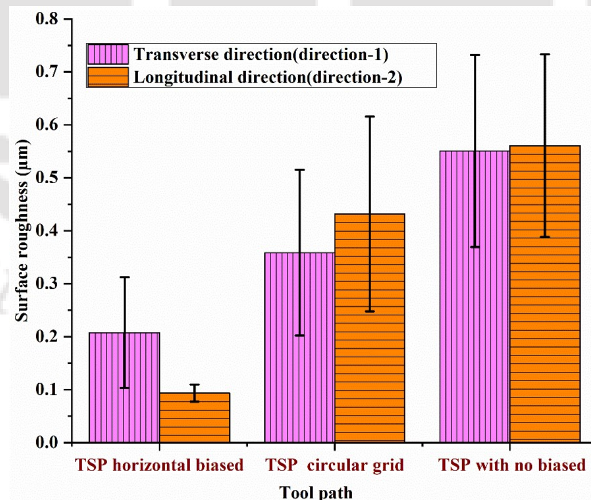

Fig. 4.39 Surface roughness values corresponding to different tool paths

Based on the above observations, it is evident that the TSP horizontal biased toolpath exhibits the lowest average surface roughness, followed by the TSP circular grid and TSP no biased toolpaths. This trend is attributed to the reduced number of turns in the TSP horizontal biased path (84 turns), followed by the TSP circular (137 turns) and TSP no

biased tool paths (150 turns). The presence of more turns in a toolpath can potentially lead to excessive material deposition at corner points. However, it is noteworthy to mention that a relatively small variation in the standard deviation (SD) is observed for each toolpath. This consistency can be attributed to the optimized center distance implemented for deposition for all toolpaths, contributing to a flatter deposited surface.

4.3.3.4 Surface characterization

In this section, the deposited surface is characterized using different methods. The deposited surface fabricated using TSP with no biased toolpath (Fig. 4.38(a)) is considered for the characterization. The FESEM image of the deposited surface morphology is shown in Fig. 4.40(a).

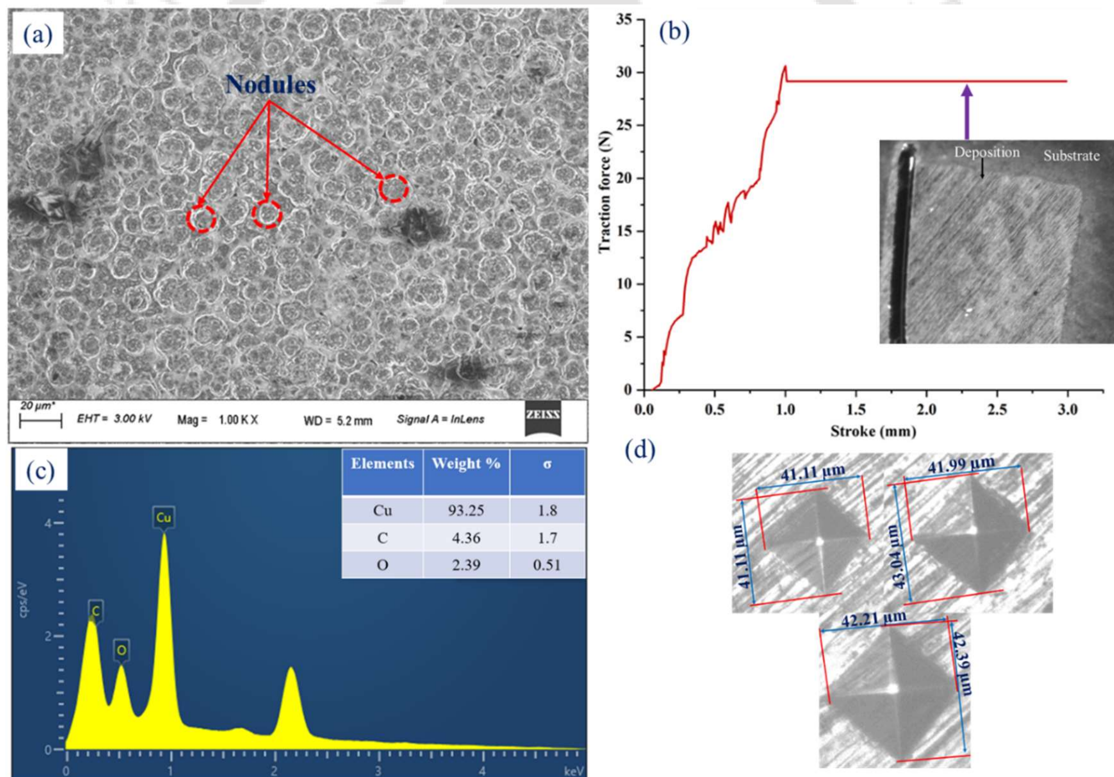

Elements	Weight %	σ
Cu	93.25	1.8
C	4.36	1.7
O	2.39	0.51

Fig. 4.40 (a) Surface morphology, (b) variation of traction force with stroke, (c) EDX analysis, and (d) microhardness of deposited bead

In this figure, the uniformly distributed smaller nodules are visible, indicating the uniformity in the deposited bead. Furthermore, the adhesion resistance of the deposited structure was measured using the scratch tester. The test involved a 3 mm scratch length (stroke) at 30 mm/min speed, with a constant normal load of 100 N. The critical load for delamination of the bead from the substrate is approximately 30 N, as shown in Fig. 4.40(b),

TH-3378_196103004

indicating a strong adhesion between the deposited structure and substrate. Additionally, EDX analysis of the deposited parts, as shown in Fig. 4.40(c), revealed a composition of 93.25% copper, with small amounts of carbon (4.36 %) and oxygen (2.39%). The presence of carbon and oxygen can be attributed to atmospheric conditions. Finally, A Vickers microhardness test was conducted with a 100 N load and a 20-second dwell period, as shown in Fig. 4.40(d). The average microhardness value is found to be 167 HV.

4.4 Summary

In the proposed SJED process, voltage and scanning speeds are the key factors that decide the uniformity of the deposition, layer width, and total layer height of the deposited nickel parts. The total layer height and width increase with the increased applied voltage. The scanning speed has a negligible effect on layer width. However, the total layer height decreases with increased scanning speed. The uniformity on the deposited bead surface can be achieved with the help of lower applied voltage and higher scanning speed. With the help of a lesser electrolyte jet diameter, a minimal layer width up to submicron size can be deposited. The center distance (d) of 0.5w between two adjacent beads offers a flat surface condition, and a gradient-based structure can be printed, maintaining d= 0.5w.

The SJED process is investigated by depositing copper beads using varying input process parameters. The height and width of the bead increase with the applied voltage; however, scanning speed has a negligible effect on bead width. Deposition profiles at 2.5V and 5V, across scanning speeds, exhibit a parabolic shape. The bead profile becomes non-parabolic (cup-shaped) at 7.5V applied voltage with decreasing cup height (hc) at higher scanning speeds. The optimal center distance (d) for achieving flat surface condition ($hv \approx 0$) is 0.45w. Surface roughness value of the deposited beads is influenced by the turns in the toolpath, with fewer turns yielding smoother surfaces. The developed SJED process allows for density-based metallic part deposition.

TH-3378_196103004

Chapter 5 Application of SJED process in micromanufacturing and coating

5.1 Introduction

Selective Jet Electrodeposition (SJED) emerges as a cutting-edge Additive Manufacturing (AM) technology, offering the ability to produce metallic components at both nano and micro scales. The atom-by-atom deposition with the SJED process showcases its application for coating and fabricating microparts with different metals. Micromanufacturing and coating using the SJED process require the application of optimized input parameters, including a carefully selected center distance between the beads. This aspect is crucial to achieve void-free and dimensionally accurate deposition. The following section elaborates on deploying the optimized parameters discussed in Chapter 4 for manufacturing and coating purposes. Two distinct metals, namely nickel and copper, have been chosen for these applications.

5.2 Manufacturing of nickel-based complicated features through SJED process

This section discusses the micromanufacturing of the nickel-based metal through the SJED process. The optimized parameters, such as applied voltage, scanning speed, and center distance between two adjacent beads for deposition, were selected based on the analysis performed in Section 4.2. The substrate material for easy separation of the deposited nickel parts is selected from Section 3.3.

5.2.1 Deposition and separation of circuit

The developed setup and methods (Section 4.2 and Section 3.3) for nickel deposition are utilized for the direct printing of complex micro-parts of nickel. A pair of circuits are printed with 15V applied voltage and 100 mm/min scanning speed and further separated. The separated micro-part (i.e., circuit) with dimensions is shown in Fig. 5.1(a). The measured width and total height of the printed circuit at a particular point are approximately 450 μm and 94 μm, respectively, as shown in Fig. 5.1(c). Fig. 5.1(b) depicts the surface morphology of the deposited circuit. A light-emitting diode is connected at both ends of

TH-3378_196103004

the fabricated circuit to validate the conductivity of the deposited micro-part. A potential difference of 3V is applied with the help of a battery source, as shown in Fig. 5.2(a) and its exaggerated view in Fig. 5.2(b). A smooth transfer of electricity is achieved (as observed in Fig. 5.2(b)) from the fabricated parts, and it can be further used to produce complex and integrated circuits. The proposed method demonstrates its capability to completely remove the fabricated micro-parts through the electrodeposition-based micro-additive manufacturing process and further remove them from the substrate surface.

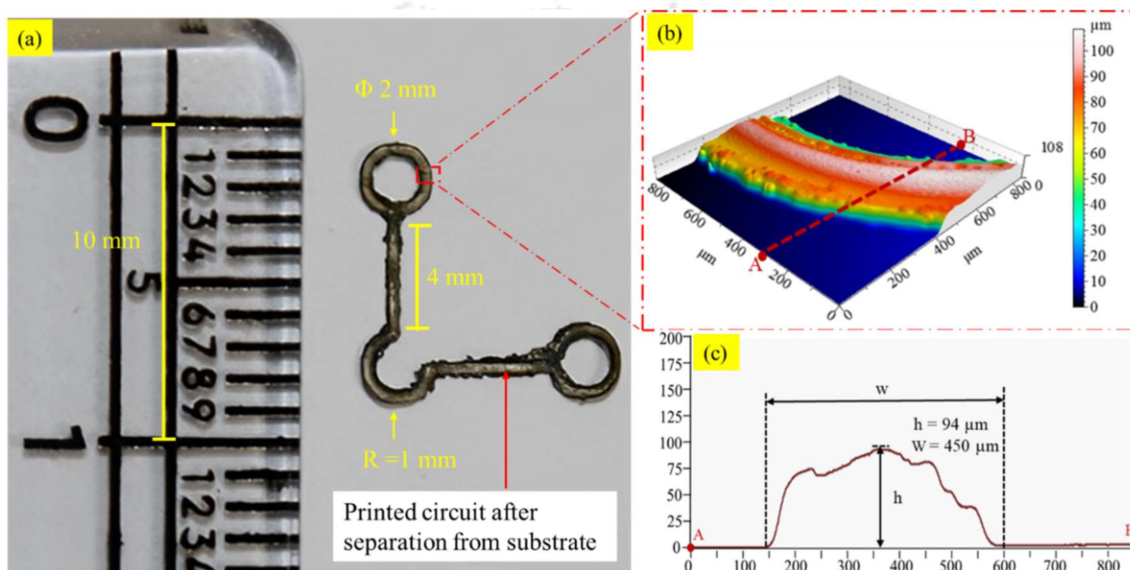

Fig. 5.1 (a) Fabricated circuit by SJED after separating from substrate and its (b) 3D morphology and (c) 2D profilometer image at a particular location

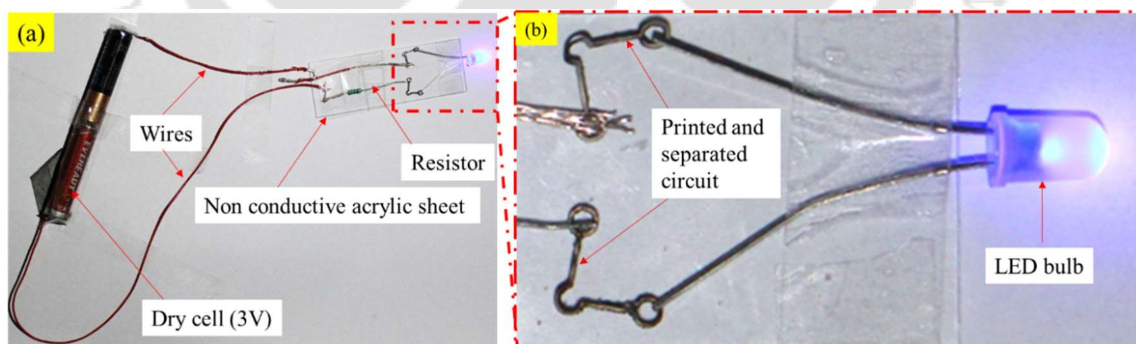

Fig. 5.2 (a) Test setup for case study and (b) its extended view

5.2.2 Deposition and separation of density-based complex structure

With the previously developed method, as discussed in Section 4.2.4, a density-based structure (i.e., a complex contour resembling a rabbit) has been successfully deposited (Fig. 5.3(b)). This complex structure implements the traveling salesman problem (TSP) tool path

algorithm in such a way that the structure's density is maximum in the central region and gradually diminishes as it extends towards the outer contour, as visualized in Fig. 5.3(a). The macroscopic image of the deposited rabbit showcasing the intricacy and precision achieved in the present SJED deposition process is provided in Fig. 5.3(c). For the analysis of the density-based deposition, a 3D profilometer image is captured at a particular location (Fig. 5.3(d)), and 2D profilometer images (Fig. 5.3(e)) are analyzed along different lines (i.e., AB and CD) on the 3D image (Fig. 5.3(d)). It is observed that there is a variation in heights in the 2D images, showing the printed deposition has a density-based gradient as provided by the tool path (Fig. 5.3(a)).

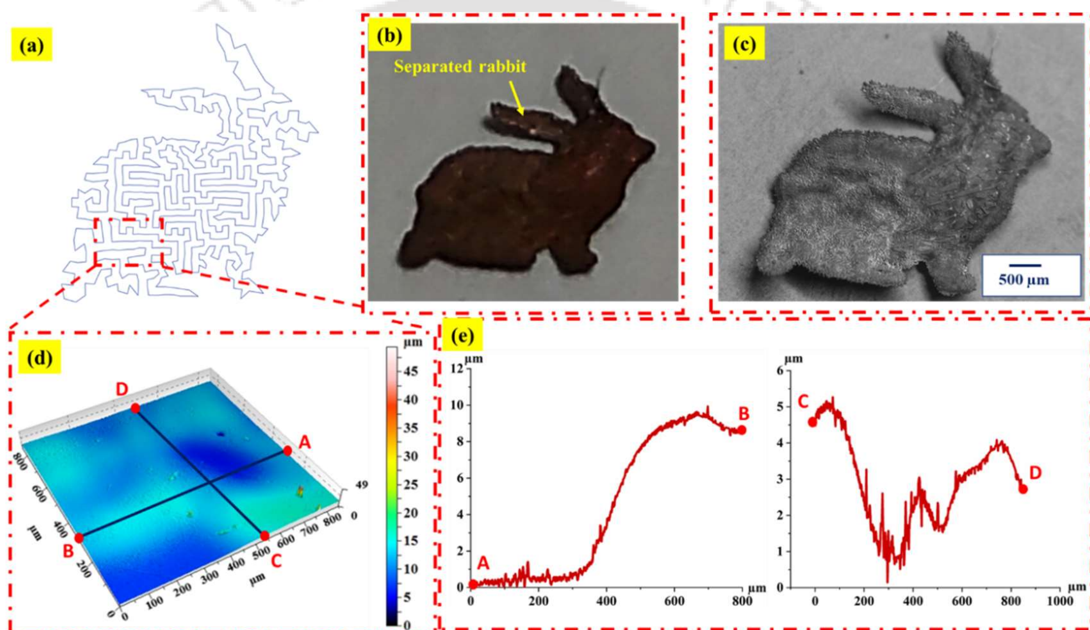

Fig. 5.3 (a) Density based gradient tool path using TSP, (b) deposited structure, and its (c) macroscopic image after separation from substrate; (d) 3D profilometer image at a particular location, and (e) 2D profilometer images along lines AB & CD

5.3 Manufacturing of copper-based complicated features through SJED process

The micromanufacturing of the copper-based feature by the SJED process is discussed in this section. The optimized parameters, such as applied voltage, scanning speed, and center distance between two adjacent beads for deposition, are selected from the analysis performed previously in Section 4.3. The substrate material for easy separation of the deposited copper feature is selected based on analysis in Section 3.3.2.

5.3.1 Deposition of density-based structure

A density-based tool path for area filling is proposed for microfabrication of the feature while implementing a TSP algorithm. The density gradient in the tool path exhibits a pattern with the highest value at the periphery, gradually decreasing towards the center (Fig. 5.4(a)). The micro-feature (i.e., a thin disk) is printed with 5V applied voltage and 100 mm/min scanning speed. The tool path, deposited structure, and its macroscopic image are shown in Fig. 5.4(a), Fig. 5.4(b), and Fig. 5.4(c), respectively. Six points are chosen to analyze density variation further, as depicted in Fig. 5.4(b) with a spacing of 0.5 mm (s=0.5mm) between two points. Fig. 5.4(d) displays 3D profilometer images at those selected points, which shows the variation in materials volume corresponding to each point.

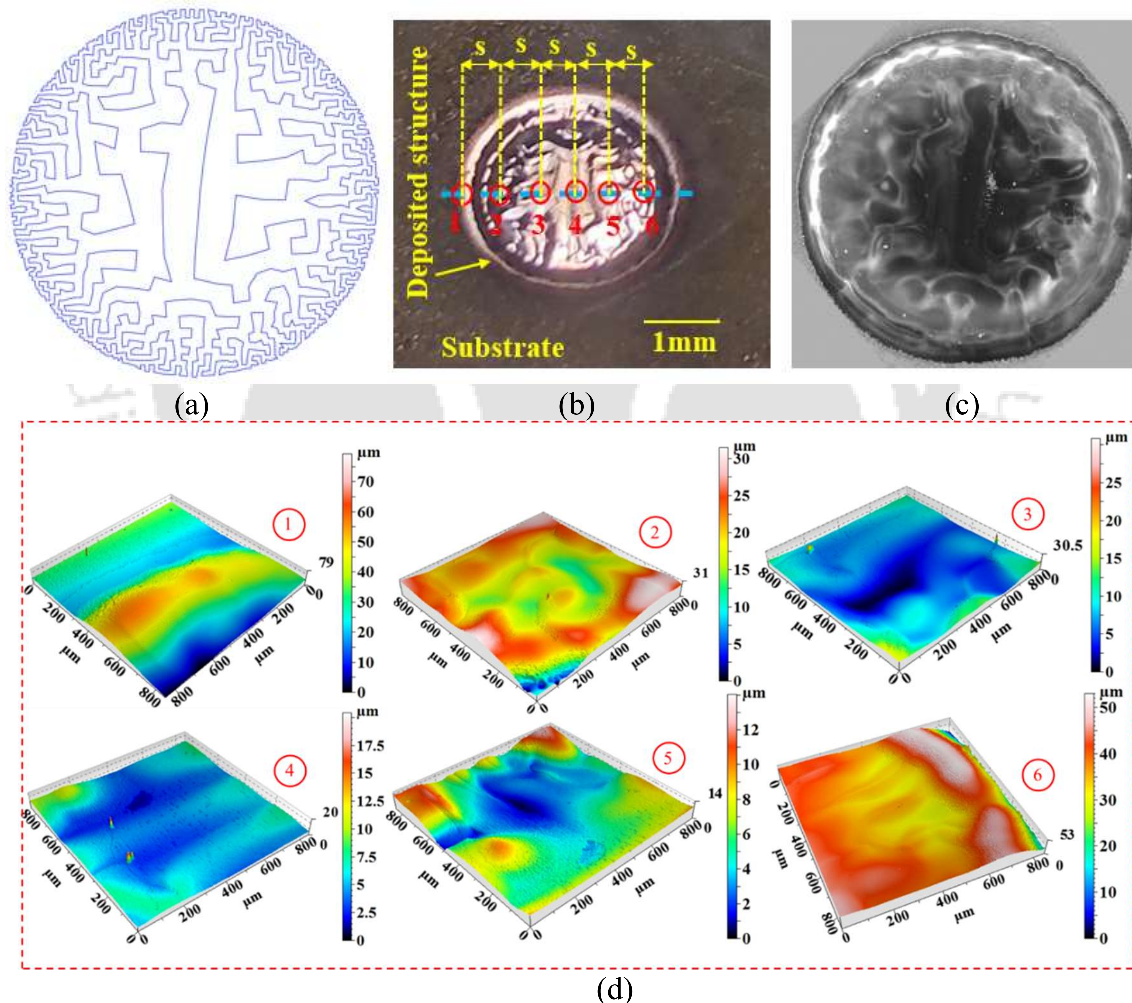

Fig. 5.4 (a) Density based gradient tool path using TSP, (b) deposited structure, (c) macroscopic image of the density-based disk, and (d) 3D surface profiles at several points marked in (b)

TH-3378_196103004

In addition, a density-based structure in the shape of a complex contour (rabbit) is deposited, illustrated in Fig. 5.5(b). The density is highest at the center and gradually decreases towards the outer contour, as depicted in Fig. 5.5(a). Fig. 5.5(c) presents the macroscopic image of the deposited rabbit. These case studies can be utilized to fabricate complex shaped impressions at the end of the tool, which is especially required in the electrochemical (ECM) and electro-discharge machining (EDM) processes.

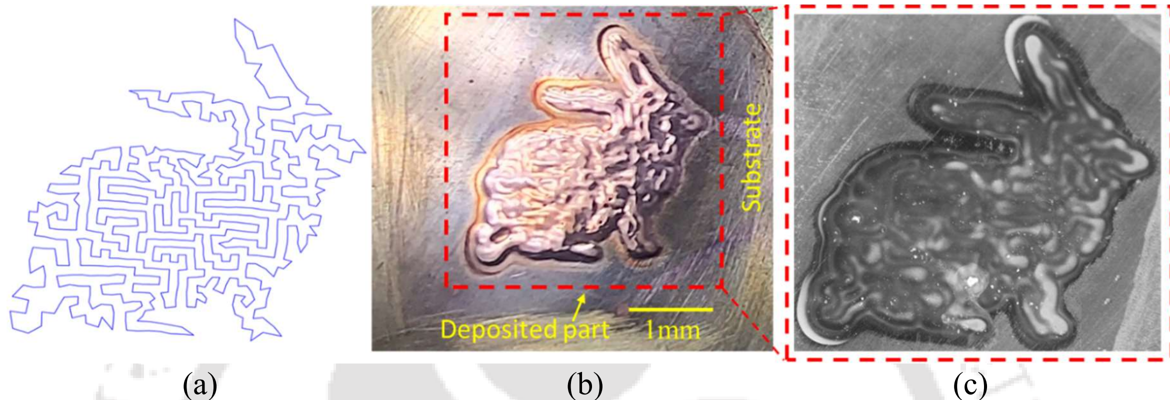

Fig. 5.5 (a) Density-based gradient tool path using TSP, (b) deposited structure, and (c) macroscopic image of deposited rabbit

5.3.2 Deposition and separation of density-based complex structure

The substrate material for the deposition and separation of copper microparts is SUS-304, as discussed in Section 3.3.2. To realize a 3D structure, a gradient-based TSP tool path of pawn shape is developed, as shown in Fig. 5.6(a). In this toolpath, the density is highest in the center and decreases towards the periphery, as shown in Fig. 5.6(a). The center distance between the adjacent beads is 0.45w, and the total layer of deposition is 1000. At the center of the pawn, where the density is highest, the layers climb onto each other. Hence, the height of the depositions increases faster than the periphery, as depicted in Fig. 5.6(b). The macroscopic image of the deposited pawn is shown in Fig. 5.6(c). The 3D pawn structure is separated by bending the substrate, as shown in Fig. 5.6(d). The 3D part and the separated substrate are shown in Fig. 5.6(e).

TH-3378_196103004

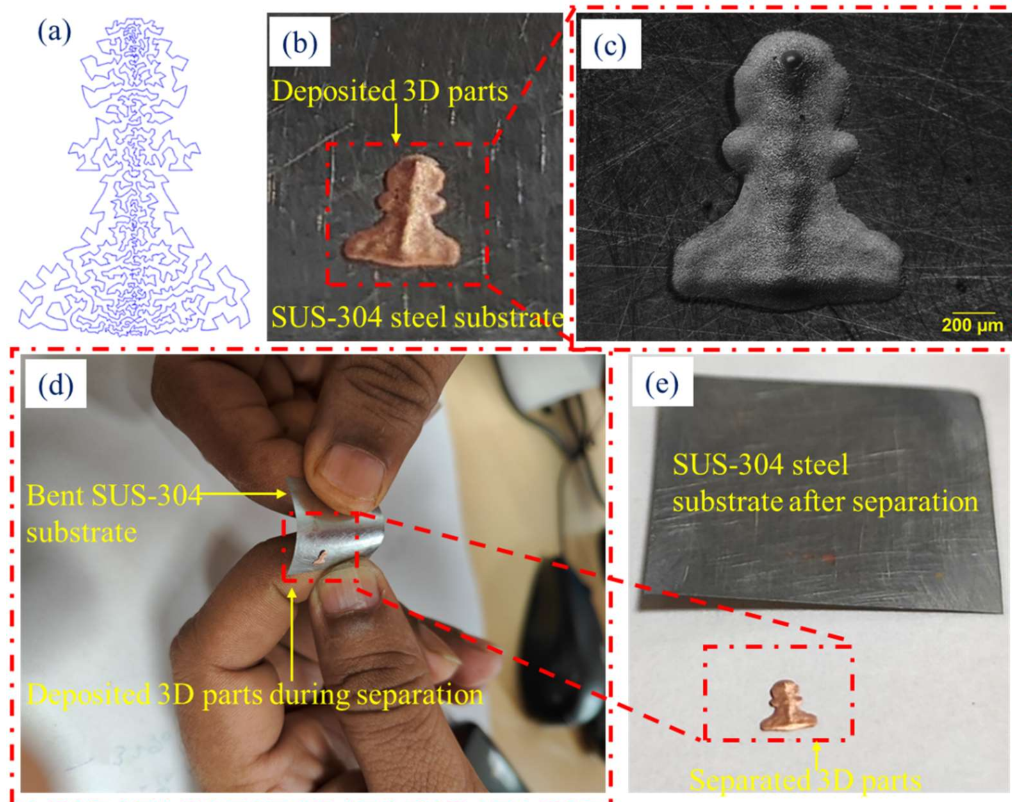

Fig. 5.6 (a) Gradient-based TSP tool path, (b) deposited 3D structure of pawn, and its (c) macroscopic image; (d) Separation of 3D parts by bending substrate, and (e) separated 3D component

5.4 Development of thick coatings through SJED and conventional methods

In this section, a thick layer coating is developed using conventional and SJED techniques and compared with the help of mechanical properties. The optimized parameters (for SJED coating), such as applied voltage, scanning speed, and center distance between two adjacent beads for deposition, are selected from the analysis performed in Appendix 1.

5.4.1 Coating by conventional method

A brass plate is chosen and polished to a mirror-like finish to deposit a thick layer of coating using the conventional electroplating technique. All faces of the substrate plate are coated with insulating paint except the 3 × 3 mm^2 area on the top face of the plate for selective coating. A square copper anode having a 3 × 3 mm^2 cross-sectional area is utilized. The setup for conventional coating is depicted in Fig. 5.7. The coating of thickness up to 48 µm

TH-3378_196103004

is deposited using several trial and error experiments. The deposited copper coating and macroscopic image are shown in Fig. 5.8(a) and Fig. 5.8(b), respectively.

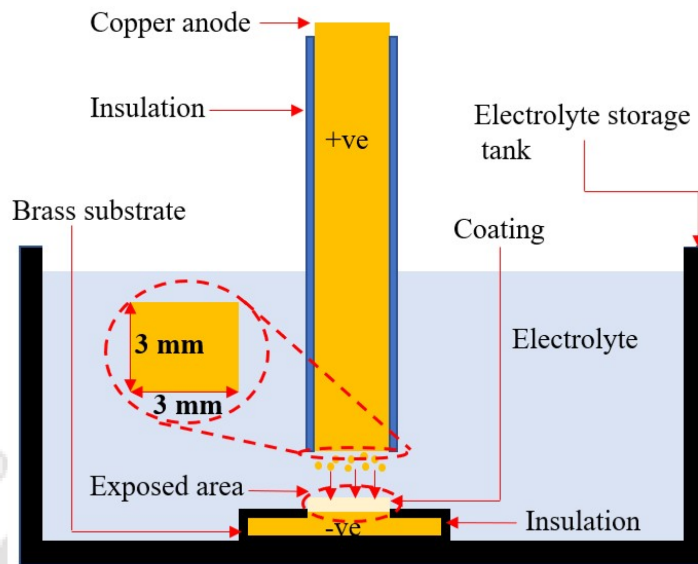

Fig. 5.7 Schematic diagram of conventional electroplating setup

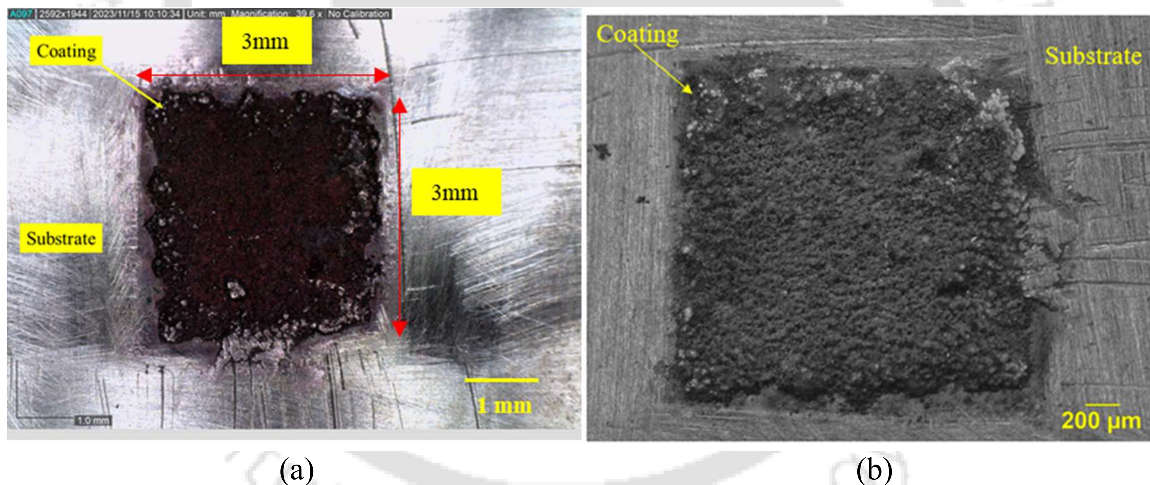

(a) (b)

Fig. 5.8 (a) Coating by conventional method and (b) macroscopic image of coating

5.4.2 Coating by SJED method

In the SJED process, toolpath planning is crucial for coating deposition. This planning is necessary because the deposition thickness achieved with a single bead is in the range of micrometers. The optimized center distance (d=0.45w) for the flat surface condition is carefully selected to prevent voids and ensure a high-quality surface finish. The raster-based toolpath on the area of 3 × 3 mm^2 area is developed with the help of CAM-based software, as shown in Fig. 5.9. The deposited parts, along with the macroscopic image, are depicted in Fig. 5.10(a) and Fig. 5.10(b), respectively. The deposition is conducted at a

TH-3378_196103004

voltage of 3.54 V, scanning speed of 80 mm/min, frequency of 297 kHz, and an electrolyte gap of 3 mm.

Fig. 5.9 Raster tool path for coating by SJED technique

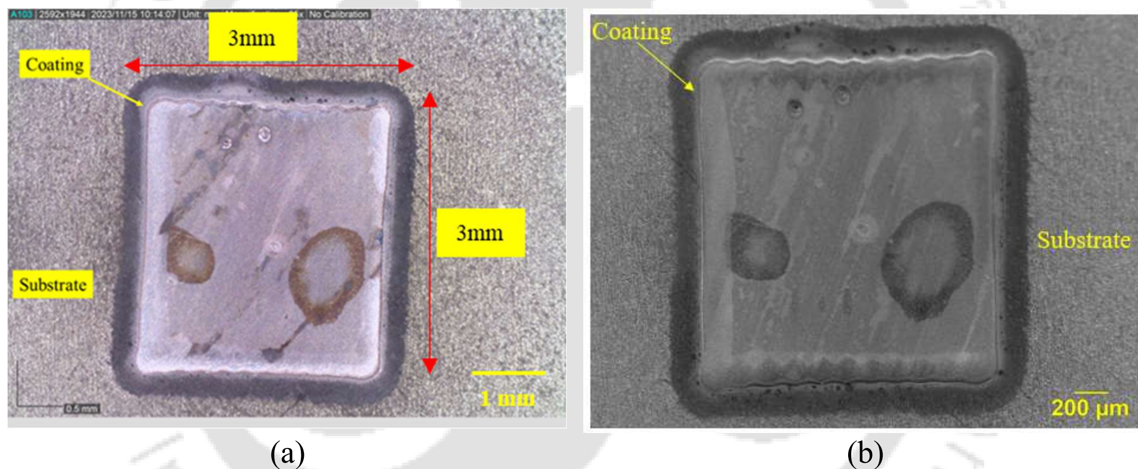

(a) (b)

Fig. 5.10 (a) Coating by SJED method and (b) macroscopic image of coating

5.4.3 Comparative studies of surface topography and mechanical properties of coatings

The following sub-sections compare both the coatings developed by conventional and SJED methods. Mechanical properties such as hardness, adhesion of the coatings with the substrate, and surface morphology of the developed coating by both processes are compared.

TH-3378_196103004

5.4.3.1 Surface morphology

The FESEM images of coatings deposited by conventional and SJED methods are presented in Fig. 5.11(a) and Fig. 5.11(b), respectively. The conventional coating exhibits large nodule size along with noticeable voids. On the other hand, the nodules obtained with SJED are much finer, and the presence of voids is negligible compared to the conventional coating. The conventional method is based on the static electrolyte condition, and the extra depositing material is taken from the copper anode; hence, the nodular size keeps increasing. However, in the case of the SJED process, there is a continuous flow of electrolytes throughout the deposition. Also, since the nozzle moves faster in SJED, the reaction time to grow a nodule is very less.

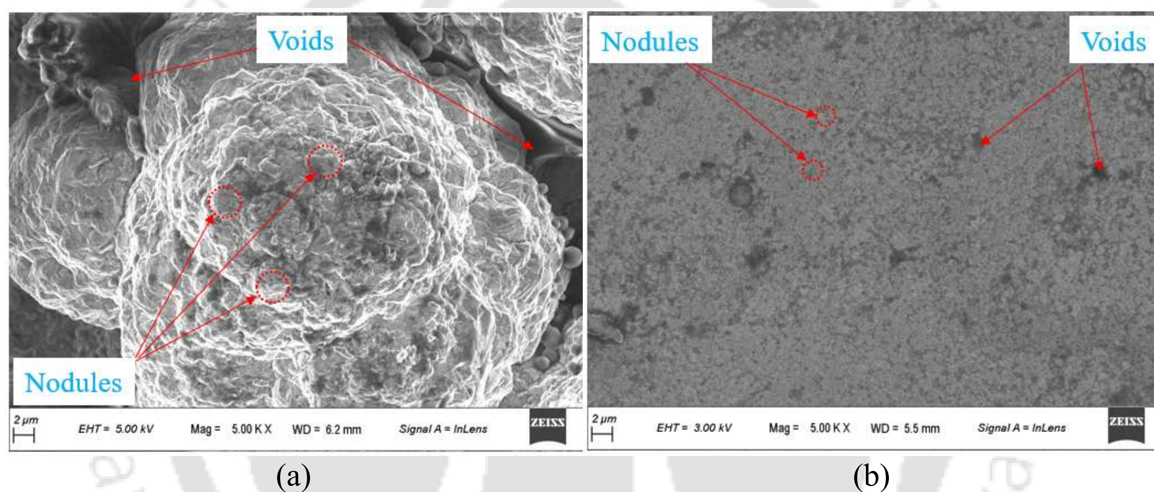

(a) (b)

Fig. 5.11 FESEM images of coating by (a) conventional and (b) SJED methods

5.4.3.2 Surface roughness

The 3D profilometer images of coatings obtained through conventional and SJED techniques are presented in Fig. 5.12(a) and Fig. 5.13(a), respectively. The 2D Surface roughness profiles for conventional (6.2 μm) and SJED (0.148 μm) coatings are shown in Fig. 5.12(b) and Fig. 5.13(b), respectively. The surface roughness value of the conventional coating is significantly higher than that of the SJED process, attributed to the substantial difference in the nodule size of the coatings. Utilizing the flat surface condition (d=0.45w) during SJED-based deposited coating is another contributing factor to achieve a better surface finish. Therefore, SJED coating can be preferred over the conventional technique to achieve a void-free higher level of smoothness.

TH-3378_196103004

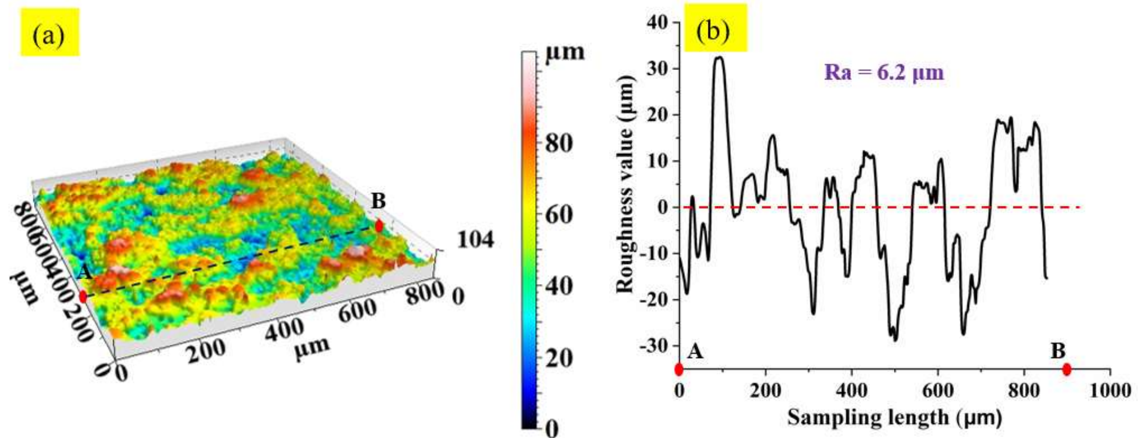

Fig. 5.12 (a) 3D and (b) 2D profilometer images of coating by conventional method

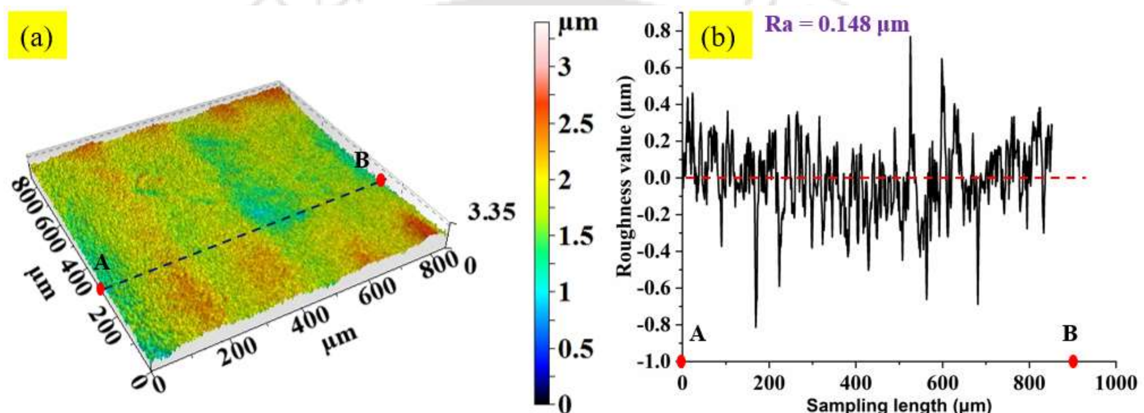

Fig. 5.13 (a) 3D and (b) 2D profilometer images of coating by SJED method

5.4.3.3 Scratch test

Scratch tests are conducted on coatings deposited by both conventional and SJED processes. The test involves a 3 mm scratch length (stroke) with a 30 mm/min scanning speed maintained under a constant normal load of 100 N. The critical load for delamination of the coating deposited by the conventional and SJED processes are 24 N and 30 N, respectively, as measured in Fig. 5.14. This higher critical load for SJED is attributed to the absence of voids and smaller nodular sizes than the conventional coating process. The absence of larger voids within the SJED coating significantly contributes to its enhanced adhesion strength. Voids can serve as initiation points for delamination under stress. Moreover, the smaller nodular sizes in the SJED-coated specimens play a pivotal role in its superior adhesion strength. The finer nodules indicate a more compact and densely packed microstructure capable of resisting crack propagation and initiation of delamination.

TH-3378_196103004

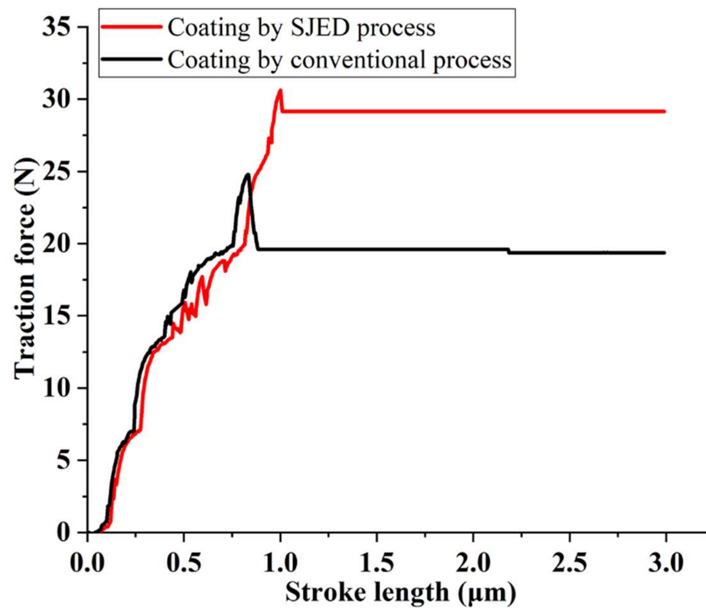

Fig. 5.14 Traction force Vs. stroke length plots for SJED and conventional coatings

5.4.3.4 Microhardness

The Vickers microhardness test was performed using an HVS-1000A tester with a 100 g load and a 20-second dwell period to compare coatings by conventional and SJED processes. The study revealed a notable difference in the microhardness of the coatings by both methods. The indentation corresponding to conventional and SJED coatings are shown in Fig. 5.15(a) and Fig. 5.15(b), respectively. The conventional coating had an average microhardness of 83 HV, while the SJED-coated specimen showed a significantly higher microhardness of 91 HV. This difference in hardness values is attributed to the precision of the SJED process, which has finer nodules in the microstructure. The SJED coating also exhibited minimal voids, enhancing its microhardness by reducing stress concentration. Optimizing deposition parameters (i.e., flat surface condition) in the SJED process likely contributed to the observed microhardness difference. Based on the above discussion, it can be concluded that SJED-based coating exhibits superior mechanical characteristics compared to conventional plating. The advantages include lower surface roughness, increased adhesive strength with the substrate, and elevated microhardness. Therefore, SJED-based coating technology can be preferable when there is a demand for high mechanical properties of the coating, especially for smaller objects.

TH-3378_196103004

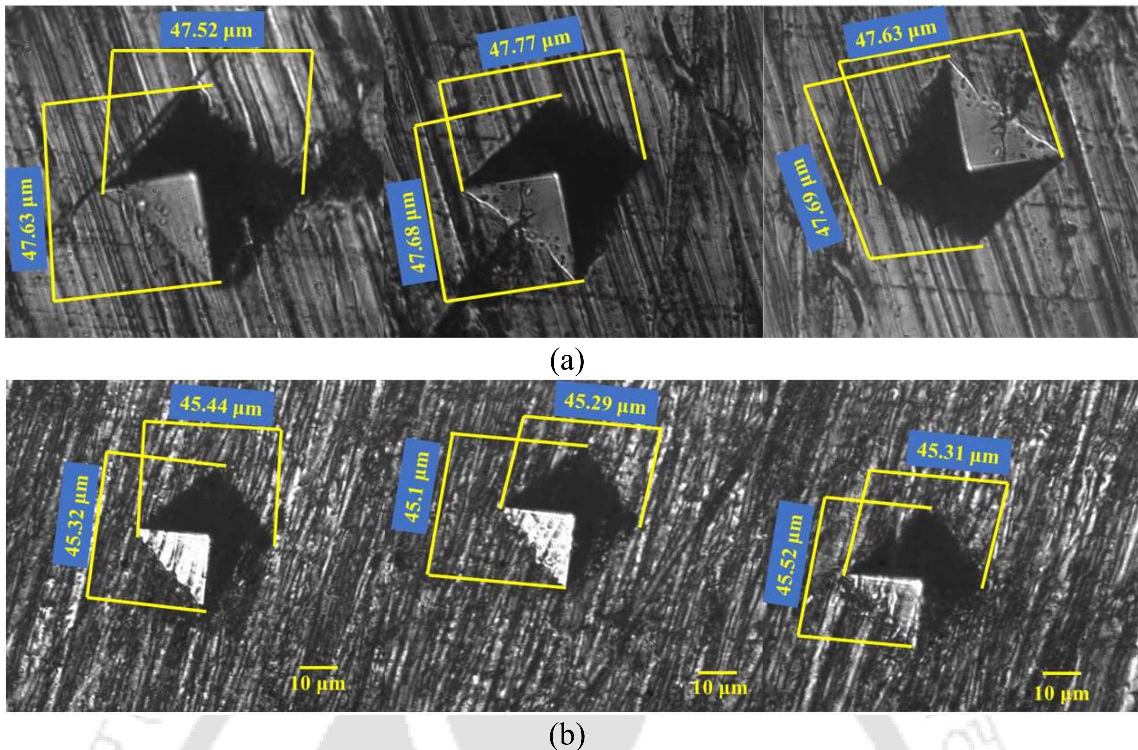

(a)

(b)

Fig. 5.15 Microhardness indentation of coatings fabricated by (a) conventional and (b) SJED methods

5.5 Summary

This chapter discussed the application of the SJED process for nickel and copper-based materials. Detailed discussions on gradient-based micro-manufacturing employing the multi-bead flat condition for copper and nickel are presented. A comparative analysis between the deposited coatings via SJED and conventional methods is conducted. The SJED-based coating exhibits superior characteristics, including higher surface smoothness, increased adhesive strength with the substrate, and elevated microhardness. Hence, SJED-based coating technology is preferred for achieving high mechanical properties in coatings, especially for smaller objects.

TH-3378_196103004

Chapter 6 Conclusions, and scope for future work

6.1 Conclusions

Additive Manufacturing (AM) has widespread applications and potential for further growth. Its key advantage lies in design freedom, enabling complex geometries and versatile material selection. Sequential layer deposition facilitates the creation of geometrically intricate parts, while optimized input parameters allow for enhanced material complexity.

While AM offers immense possibilities, fully realizing its capabilities and overcoming limitations require exploring novel ideas. In essence, this work represents a modest attempt at such exploration. The suggested SJED system features a simple design that allows for easy fabrication of setup components using FDM and SLA-based 3D printers. The SJED process is developed to micromanufacture metallic parts. Toolpath strategies were formulated to generate continuous deposition for both uniform and gradient/density-based microparts. This approach aims to mitigate defects associated with process instabilities during the initiation and cessation of the deposition processes. Two metals, nickel and copper, are investigated for uniform deposition. The study involves exploring and optimizing process parameters specific to each metal.

While the current work strives for detailed exploration, numerous unexplored research possibilities exist within the framework of the presented ideas. This chapter outlines the selection of such research opportunities and their future scope. The following sections provide a comprehensive summary of the present work.

6.1.1 Selective jet electrodeposition (SJED)

6.1.1.1 Development of SJED Setup

An experimental setup of SJED has been designed and developed to fabricate micro-features. The developed setup consists of subsystems: the power supply unit, the electrolyte circulation unit, and the CNC controller for precise movement. The following conclusions are drawn from the present study.

TH-3378_196103004

- The power supply unit consists of a DC power supply, pulse generator, digital oscilloscope, and multimeter. DC power supply provides the constant direct current of set potential. The pulse generator consists of waves like sine, square, triangular, etc., with different frequencies and duty cycles. A digital oscilloscope and multimeter are used to visualize the pulse and the potential difference.
- A tool holder, crucial for the stability and ease of assembly and disassembly, is fabricated using the FDM process. It ensures the secure integration of the nozzle unit components.
- The workpiece fixture is made of Perspex, which is non-reactive to electrolytes and non-conductive, thus resulting in no loss of charge. Allen bolts are used to fix the workpiece at the desired location and provide a power supply.
- The electrolyte circulation and nozzle unit system outlines the intricate electrolyte circulation and nozzle system, featuring precision-engineered components, including a fabricated nozzle using fused filament fabrication (FFF). The tight integration of the capillary tube ensures enhanced fluid dynamics for efficient electrolyte delivery.
- A deposition chamber is also made of Perspex, which is readily machinable and transparent. It holds the electrolyte as well as the workpiece fixture.
- The developed SJED process can directly print the 3D-metallic parts on the micrometer scale. The continuous flow of the electrolyte can be achieved with the help of a commercially available submersible pump, making the process economical.

6.1.1.2 Nickel deposition through SJED

The present study proposes a jet-based electrodeposition technique, also known as SJED process, for manufacturing metal-based micro-parts. The process parameters were decided through several experiments. The surface morphology and uniformity of the deposited structure were observed. A multi-bead analysis is done with different center distances between adjacent beads. Also, a method is proposed to separate the micro-deposited parts from the substrate surface. The critical conclusions from the current study are as follows:

- The voltage and scanning speeds are the key factors that decide the uniformity of the deposition, layer width, and total layer height of the deposited parts. The total layer height and width increase with the increased applied voltage. The scanning speed has a negligible effect on layer width. However, the total layer height decreases with

TH-3378_196103004

increased scanning speed. A uniform deposited micro-parts can be achieved with the help of lower applied voltage and higher scanning speed.

- With the help of a lesser electrolyte jet diameter, a layer width of submicron size can be deposited.
- The optimized center distance (d) of 0.5w between two adjacent beads offers a flat surface condition. Also, with the help of the optimized center distance of 0.5w, a density/gradient-based structure can be printed.

6.1.1.3 Copper deposition through SJED

The SJED process was introduced to manufacture copper-based micro-parts. The parameters were determined through a series of experiments. This process is being investigated by depositing beads with varying input process parameters. The critical conclusions are as follows:

- The height and width of the bead increase with the applied voltage; however, scanning speed has a negligible effect on bead width.
- The deposited profiles generated at 2.5V and 5V for all the scanning speeds (100, 125, and 150mm/min) is parabolic.
- The profile obtained at 7.5V is non-parabolic (cup-shaped), and with increased scanning speed, the height of the cup (hc) decreases.
- The optimum center distance (d) for the SJED process to obtain the flat surface ($hv \approx 0$) is 0.45w.
- The surface roughness obtained is directly affected by the number of turns associated with the toolpath. A smaller number of turns gives high surface smoothness. Therefore, a toolpath with a lower number of turns should be preferred for SJED.

6.1.1.4 Applications of SJED process

Micromanufacturing and coating through the SJED process need optimized input parameters, specifically a center distance between the adjacent beads. This factor is essential in ensuring a void-free and dimensionally accurate deposition. The conclusion is as follows:

- The complete removal of the deposited parts is possible with the proposed method. The separated parts are free from cracks and distortion as no mechanical forces are

TH-3378_196103004

used during separation. The substrate can be reused, making the proposed process economical.

- Gradient-based deposition is possible with the help of toolpath planning.
- 3D parts can be printed and separated easily when acid-treated SUS-304 stainless steel of lesser thickness is used as a substrate in the case of copper electrodeposition.
- SJED process can be used for thick coating with the help of toolpath planning (with a flat surface condition for the multi-bead)
- SJED-based coating demonstrates superior characteristics compared to conventional plating. The advantages include higher surface smoothness, increased adhesive strength with the substrate, and elevated microhardness. Therefore, when aiming for high mechanical properties of the coating, especially for smaller objects, SJED-based coating technology emerges as a preferable choice.

6.2 Scope for future work

- A robust SJED setup with an in-house arrangement, a 5-axis control unit, and a high-speed camera to monitor the real-time behavior of the deposition in the interelectrode gap needs to be developed.
- Image processing needs to be utilized to analyze the deposition error of fabricated micro-parts.
- A numerical model should be developed to analyze the effect of process parameters on the deposition during the SJED process.
- The SJED process needs to be utilized to fabricate micro-parts and coating of high-entropy alloys.
- The SJED process needs to be utilized for depositing free-hanging structures with the help of apprriate toolpath planning.

TH-3378_196103004

Appendix A1 Statistical DOE study of thick coating by SJED process

A1.1 Introduction

Electrodeposition is a widely applied technique in various industries, serving purposes like surface coating, plating, and micro-additive manufacturing. This process is known for its flexibility in selecting materials, precise deposition control, and the capability to fabricate intricate structures with remarkable precision. In the electrodeposition process, both the anode and cathode are submerged in an electrolyte solution. This solution contains metal ions (M^{n+}) that are drawn toward the oppositely charged electrodes. Applying a potential difference between the anode and cathode prompts the ions to migrate to their respective electrodes, where they undergo chemical reactions[109], as indicated in Eqns. (A1.1) and (A1.2). This sequence results in the deposition of the desired material onto the cathode's surface, enabling the controlled growth of the deposited components.

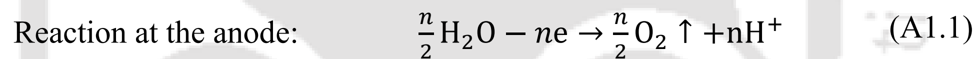

Reaction at the anode: $$\frac{n}{2}\mathrm{H_2O} - ne \rightarrow \frac{n}{2}\mathrm{O_2}\uparrow + n\mathrm{H^+} \quad \text{(A1.1)}$$

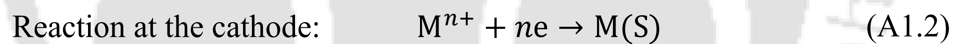

Reaction at the cathode: $$\mathrm{M}^{n+} + ne \rightarrow \mathrm{M(S)} \quad \text{(A1.2)}$$

Conventional electroplating technique (Fig. A1.1(a)) is commonly used to coat conductive components. However, they pose specific challenges, particularly in terms of deposition rate, grain size, and adhesion to the base material. Furthermore, achieving precisely localized coatings using conventional electrodeposition methods is a complex task. To tackle the issues outlined above, selective jet electrodeposition (SJED) has emerged as a promising technology in the field of electrodeposition, as shown in Fig. A1.1(b), which incorporates principles from additive manufacturing. The fundamental principle of SJED resembles conventional electrodeposition, but its key distinction lies in how mass transfer occurs within the electroplating process. In typical electrodeposition, mass transfer primarily relies on diffusion and electromigration. In contrast, with jet electrodeposition, convection takes precedence as the primary mode of mass transfer [115]. Hence, there is an increase in material transfer efficiency, as reported by Liu et al. [69]. SJED is characterized by its distinct fluid dynamics attributes, achieving surface activation

of the cathode workpiece through a high-speed impact of the electroplating solution. This activation reduces the diffusion layer thickness, forming finer metal grain structures while creating more densely packed deposition beads. In the process, a wall jet, often called a relatively thin electrolyte radial layer, forms at a distance from the impingement zone, as depicted in Fig. A1.1 (b). The electrical resistance of this wall jet is notably higher than that of the direct impingement region, mainly due to its thin structure. As a result, the amount of deposition under the wall jet area is either negligible or nonexistent compared to the direct impingement zone [67], [71].

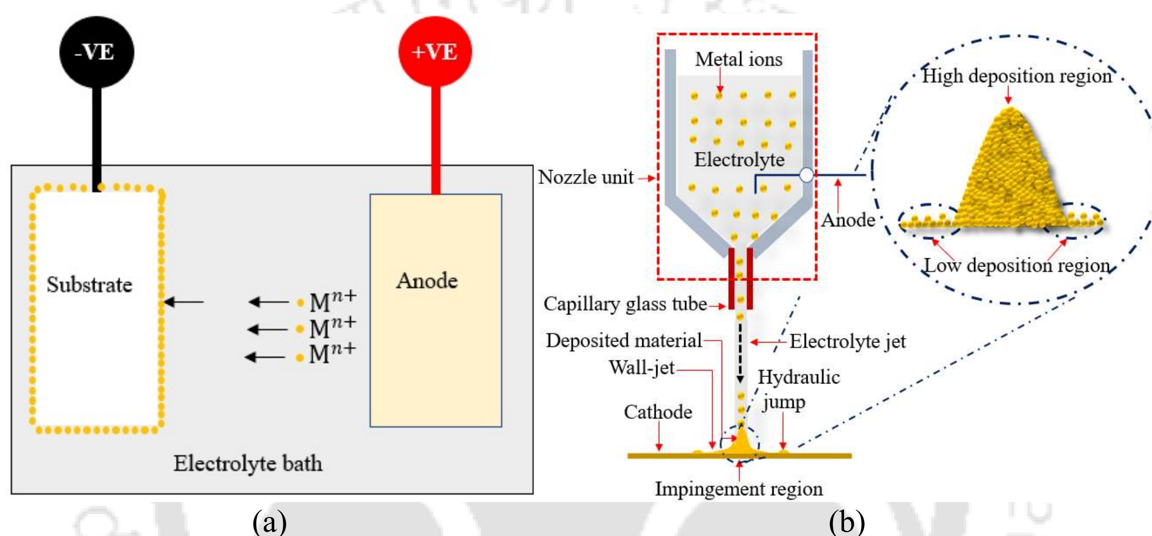

(a) (b)

Fig. A1.1 Method of electrodeposition by (a) conventional and (b) SJED processes

Gervasi et al. [116] comprehensively investigated current density distribution by the SJED process. Their findings indicated that the rate of mass transfer increases with increased current density, which is influenced by the applied hydrodynamic conditions in the impingement zone [117]. This theory is supported by the experiments conducted by Isobe et al. [118]. Isobe and colleagues performed electrodeposition of a conducting polymer, specifically pyrolytic graphite, on a highly oriented pyrolytic graphite substrate. They observed that deposition occurred at a faster rate with increased applied voltage. The gap between the electrolytes serves as resistance and is typically constant during a single run of the electrodeposition process. When the gap widens, it increases resistance, which subsequently leads to a reduction in the current density [53]. Alkire et al. [119] reported an optimal electrode gap ranging from 2.5 to 3 mm. Very few studies have been conducted on the nature of the electrolyte and its influence on the properties of the as-deposited material.

TH-3378_196103004

It has been reported that maintaining a low pH level in the electrolytes enhances the smoothness and brightness of as-deposited pure metallic features [69].

Georgiadou et al. [120] developed a mathematical model to calculate the filling rate of micro trenches through the copper electrodeposition process. They compared direct and reverse pulsing and found that direct pulsing enhances ion movement and deposition rate in the electrodeposition process. Another study revealed that the current density and duty ratio are crucial in forming nuclei and dendritic growth [88]. SJED provides the advantage of achieving denser deposition compared to conventional electrodeposition methods [121]. A high-speed electrolyte plays a crucial role by delivering a substantial number of anodic ions to the cathode, leading to enhanced ion transfer. Employing multiple passes ensures significant deposition, uniformity, and high material density [97]. One study demonstrates that adjusting the pH value to the higher side leads to an increased ion transfer rate, resulting in greater thickness during the deposition process [66]. Also, deposition thickness increases with higher potential difference applied between the electrodes. SJED results in a smoother surface than conventional DC electrodeposition methods [100]. In pulse electrodeposition, a higher duty ratio and an applied electrode potential were observed to result in lower porosity in the deposited material [73]. The pulsing technique in SJED enables it to operate at a high current density, resulting in enhanced control and regulation of grain growth [60]. Many researchers aimed to calculate the deposition rate perpendicular to the base plate in the SJED process, considering that the anode moves primarily in the Z direction. However, when SJED is applied for coating, the tool operates simultaneously in all three coordinate axes (X, Y, and Z). Since the present study uses SJED for coating, further research is essential to ascertain the layer height and width under various process parameter conditions.

The present study investigates the effect of several factors, including the current frequency, applied voltage, and scanning speed, on the deposited layer height and width using an indigenously developed SJED setup (Fig. A1.2) based on a statistical design of experiments (DOE) methodology. The process parameters and their respective ranges are determined through preliminary experimental studies and insights from prior research by other researchers. Each experiment conducted within the DOE framework involves the deposition of a single bead measuring 3 mm in length. The resulting geometric features of these depositions are then characterized using a microscope and a non-contact profilometer. Furthermore, a multi-bead analysis is performed with the optimized parametric conditions. Finally, a tool path strategy is developed with the obtained multi-bead process parameter condition to achieve flat surface conditions for electroplating/coating.

TH-3378_196103004

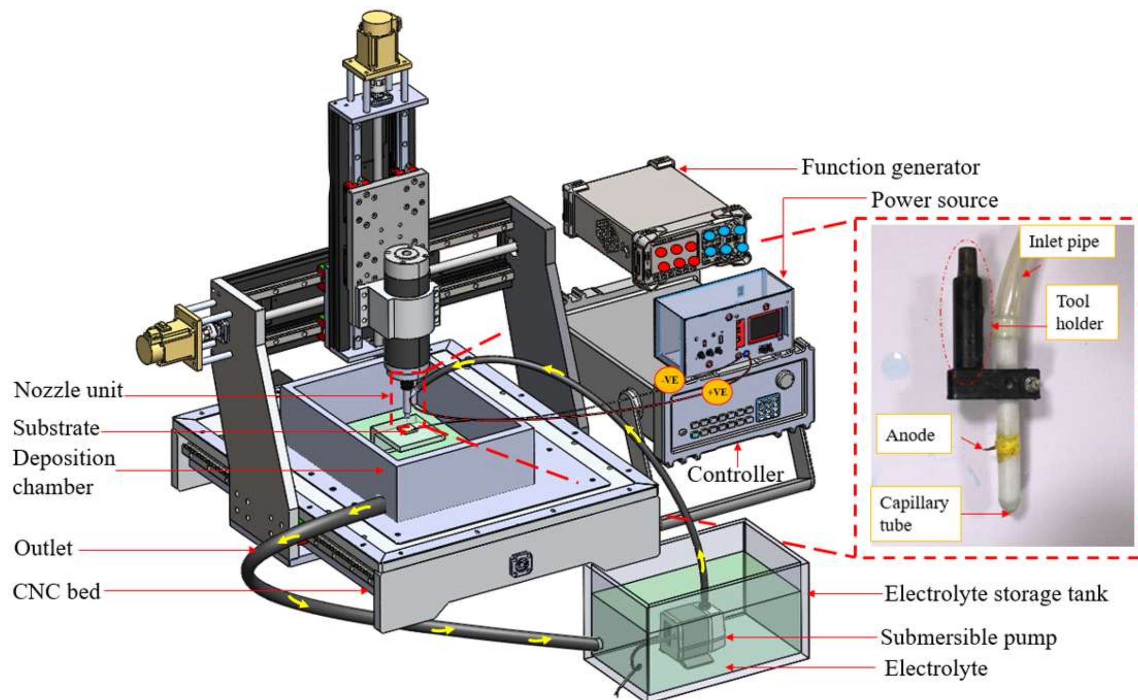

Fig. A1.2 Experimental setup of SJED process

A1.2 Materials and method

The SJED setup features three systems: The Nozzle unit for electrolyte delivery, the CNC unit for controlled motion with a deposition chamber, and the Power unit for current supply, as shown in Fig. A1.2. A function generator is linked to the power supply for configuring frequency and waveform type. The electrolyte commonly employed for copper deposition typically comprises 250 g/L of copper sulfate pentahydrate ($CuSO_4 \cdot 5H_2O$) and 75 g/L of sulfuric acid (H_2SO_4) dissolved in one liter of distilled water [40]. In the current study, the cathode is constructed from a brass sheet measuring 20 × 20 × 3 mm^3, and it possesses a polished surface with a mirror-like finish attained through wet polishing using different grades of emery papers.

Based on the literature survey and preliminary experimental results, the process parameters, including applied voltage, frequency, scanning speed, and their respective ranges, have been chosen to investigate their influence on the output responses (i.e., layer height and width). The duty ratio for all experiments is set at a fixed value of 75% as it yields superior deposition results compared to a lower duty ratio. The electrolyte gap for all the experiments is chosen to be 3 mm. A statistical design of experiments using a central composite design (CCD) has been conducted to explore the relationship between process

TH-3378_196103004

parameters and output responses. Table A1.1 presents the process parameters with three levels. The total number of experiments (D) can be calculated using Eq. (A1.3).

$$D = 2^X + 2X + X_C \quad \text{(A1.3)}$$

Where, X denotes the number of process variables, and X_C represents the center points. For this study, six center points have been chosen to plan and conduct 20 experiments.

Table A1.1 Process variables and their levels

Parameters	Units	Levels		
		-1	0	1
Applied voltage (V)	Volt	3	4	5
Scanning speed (S_s)	mm/min	80	100	120
Frequency (F)	kHz	100	200	300
Constant parameters:	Electrolyte gap	3 mm		
	Duty ratio	75%		

Table A1.2 Statistical design of experiments with corresponding responses

Exp. No.	Process parameters			Responses	
	Voltage (V)	Scanning speed (mm/min)	Frequency (kHz)	Layer height, h (µm)	Layer width, w (µm)
1	4	100	200	46	329
2	4	100	200	49	329
3	4	100	200	48	330
4	3	120	100	29	310
5	4	100	200	48	328
6	5	80	100	71	350
7	5	120	300	54	345
8	4	100	200	47	329
9	4	100	100	49	336
10	4	80	200	52	330
11	4	120	200	41	329
12	3	100	200	34	305
13	5	80	300	70	345
14	4	100	200	48	332
15	3	80	300	40	300
16	5	100	200	62	346
17	3	80	100	39	305
18	3	120	300	30	315
19	4	100	300	49	332
20	5	120	100	55	350

Table A1.2 presents the experimental plan, where each experiment entails depositing a multi-layer (250 layers) single bead measuring 3 mm in length onto a brass substrate.

TH-3378_196103004

Three repetitions are carried out at each experimental condition to ensure the reliability of the results, and the average values of the responses are calculated to reduce the impact of potential experimental interference. Trial experiments are carried out to validate the functionality and suitability of the setup within predefined input parameter ranges. The responses, namely layer height (h) and layer width (w), are assessed using a high-precision, non-contact computerized surface profilometer (Talysurf CCI; Taylor Hobson). Measurements are taken at three different points along the length of the deposited bead, and an average value of the output response is computed.

A1.3 Results and discussion

This section outlines the analysis of variance (ANOVA) study and the optimization of the process parameters. Additionally, experimental validation of the output results is conducted.

A1.3.1 ANOVA study

ANOVA is conducted for both responses, namely layer height and width, as illustrated in Table A1.3 and Table A1.4, respectively. This analysis includes a lack-of-fit test and a test to determine the significance of the models. The significance of the model is assessed by examining the F-values presented in the ANOVA table. In Table A1.3 and Table A1.4, the p-values of the models are less than 0.05, signifying that the models are significant for a 95% confidence interval. However, the lack-of-fit terms are insignificant, which means that both models fulfill the necessary criteria for reliability. The coefficient of multiple determination (R^2) for layer height and width are 0.94 and 0.99, respectively. In both cases, the R^2 values are close to unity, meaning higher fitting of experimental data.

Based on the responses detailed in Table A1.2, quadratic models are developed for layer height and width. The regression model effectively describes the relationship between the input parameters and the output responses. The regression equations for layer height (h) and width (w) are presented in Eqs. (A1.4) and (A1.5), respectively.

$$h = 47.62 + 14 \times V - 6.3 \times S_s - 1.5 \times V \times S_s - 50 \times 10^{-2} \times V \times \mathrm{F} + 45 \times 10^{-2} \times V^2 - 1 \times S_s^2 + 1.45 \times \mathrm{F}^2 \tag{A1.4}$$

$$W = 309.86 + 20.10 \times V + 1.90 \times S_s - 1.4 \times \mathrm{F} - 2.5 \times V \times S_s \tag{A1.5}$$

TH-3378_196103004

$$-1.25 \times V \times \mathrm{F} + 1.25 \times S_s \times \mathrm{F} - 4.91 \times \mathrm{V}^2 - 0.90 \times S_s^2 + 3.59 \times \mathrm{F}^2$$

Where V, S_s, and F signify applied voltage, scanning speed, and frequency of current, respectively (Table A1.3 and Table A1.4).

Table A1.3 ANOVA for layer height

Source	Sum of Squares	df	Mean Square	F-value	p-value	
Model	2385.97	9	265.11	379.71	< **0.0001**	significant
V-Applied voltage	1960.00	1	1960.00	2807.29	< **0.0001**	significant
S_s-Scanning speed	396.90	1	396.90	568.48	< **0.0001**	significant
F -Frequency	0.0000	1	0.0000	0.0000	1.0000	
AB	18.00	1	18.00	25.78	**0.0005**	significant
AC	2.00	1	2.00	2.86	0.1214	
BC	0.0000	1	0.0000	0.0000	1.0000	
A^2	0.5682	1	0.5682	0.8138	0.3882	
B^2	3.01	1	3.01	4.31	0.0648	
C^2	5.82	1	5.82	8.33	**0.0162**	significant
Lack of fit	1.65	5	0.3297	0.3091	0.8883	not significant

Table A1.4 ANOVA for layer width

Source	Sum of Squares	df	Mean Square	F-value	p-value	
Model	4261.32	9	473.48	117.12	< **0.0001**	significant
V -Applied voltage	4040.10	1	4040.10	999.35	< **0.0001**	significant
S_s -Scanning speed	36.10	1	36.10	8.93	**0.0136**	significant
F -Frequency	19.60	1	19.60	4.85	0.0523	
AB	50.00	1	50.00	12.37	**0.0056**	significant
AC	12.50	1	12.50	3.09	0.1092	
BC	12.50	1	12.50	3.09	0.1092	
A^2	66.27	1	66.27	16.39	**0.0023**	significant
B^2	2.27	1	2.27	0.5622	0.4707	
C^2	30.93	5	6.19	3.26	0.1105	
Lack of fit	75.60	5	15.12	2.05	0.2244	not significant

A1.3.2 Parametric study using response surface plots

The ANOVA results in Table A1.3 and Table A1.4 offer insights into how the input variables collectively affect the output responses. However, individual input parameters seem to have conflicting impacts on output responses. Therefore, it is essential to simultaneously evaluate the combined influence of all input parameters to achieve the desired responses and determine the best and most practical solution. The following sections will provide a detailed examination of how applied voltage, scanning speed,

TH-3378_196103004

frequency, and their interactions collectively impact the dimensions of the deposited layer in terms of height and width.

Layer height

The 3D plot in Fig. A1.3(a) illustrates the combined impact of scanning speed and applied voltage on layer height. An increase in applied voltage leads to a higher layer height, primarily because higher applied voltage increases current density, resulting in increased ion deposition and a thicker layer. Conversely, higher scanning speed reduces layer height due to the limited time available for reactions on the cathode surface. The combined influence of applied voltage and frequency on the layer height is depicted in Fig. A1.3(b). The impact of frequency of current on the deposited layer's thickness is minimal compared to other factors. This is primarily because the energy input, which is determined by voltage amplitude and duty ratio, remains constant at varying frequencies. The combined effect of scanning speed and frequency on the layer height is presented in Fig. A1.3(c). It can be noticed that the variation in frequency has a negligible effect on the layer height because of the reasons discussed above. However, the layer height decreases with increased scanning speed.

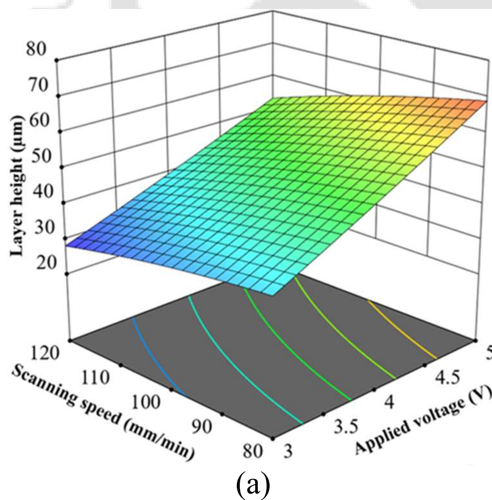

(a)

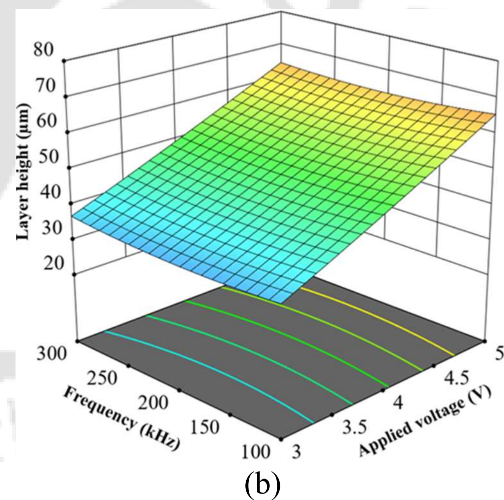

(b)

TH-3378_196103004

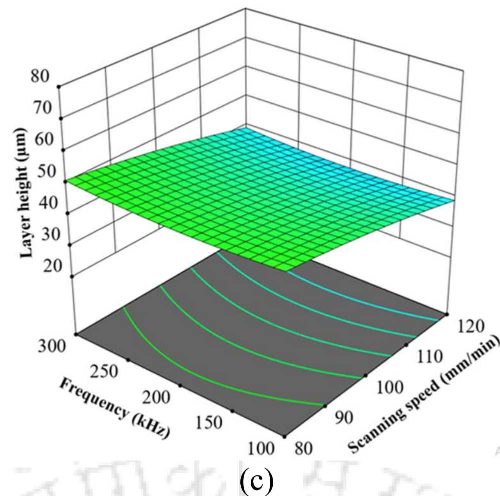

(c)

Fig. A1.3 Combined effect of (a) scanning speed and applied voltage, (b) frequency and applied voltage, and (c) frequency and scanning speed on layer height

Layer width

The 3D plot in Fig. A1.4(a) indicates the combined impact of applied voltage and scanning speed on layer width. The response surface plot demonstrates that as the applied voltage increases, the layer width also increases. A higher applied voltage induces a more rapid ionic reaction, leading to vigorous bubble formation within the electrolyte jet. These intense bubbles generate turbulence in the jet, causing the current density within the electrolyte jet to disperse over a larger surface area. As the deposition follows this current distribution pattern, the layer width also increases with the applied voltage. Fig. A1.4(a) demonstrates that scanning speed has an insignificant impact on the deposited layer width within the selected range. This is because there is no change in current density when scanning speeds are adjusted while keeping the other parameters constant.

The combined influence of applied voltage and frequency on the layer width is depicted in Fig. A1.4(b). As the applied voltage increases, the layer width also increases, as previously shown. However, increasing the frequency reduces the layer width. This is because higher frequencies lead to a faster establishment of a steady-state current at the cathode surface, resulting in a more localized current density and narrower layer width. The reduction in width is relatively small but may be more noticeable with a broader frequency range. The combined effect of scanning speed and frequency on the layer width can be seen in Fig. A1.4(c). It can be noticed that the increase in frequency has an insignificant effect on the layer width for the above-mentioned reasons. Also, the scanning speed is having a negligible impact on layer width.

TH-3378_196103004

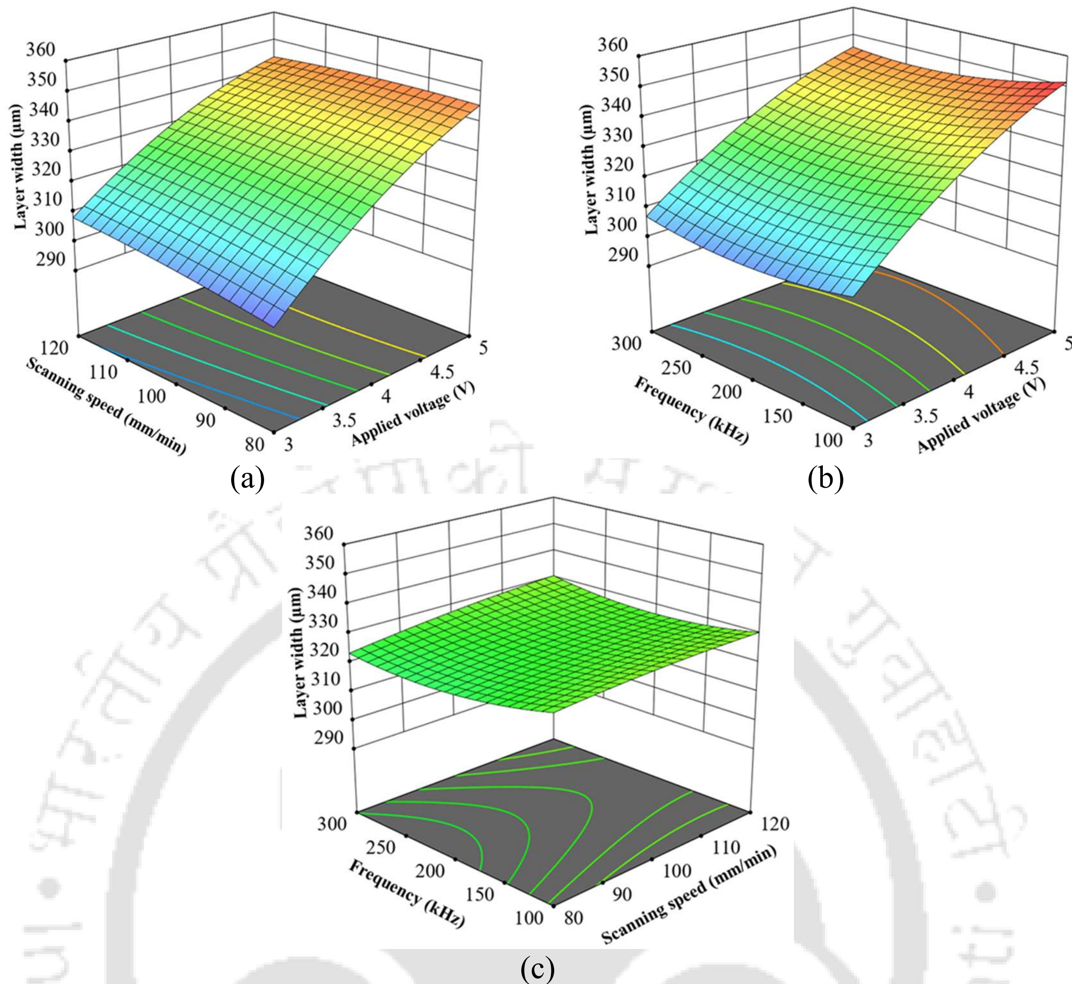

Fig. A1.4 Combined effect of (a) scanning speed and applied voltage, (b) frequency and applied voltage, and (c) frequency and scanning speed on layer width

A1.3.3 Optimization study using desirability function-based approach

The study has revealed that examining the interaction between various process parameters provides valuable insights for achieving improved results. Consequently, identifying the optimal combination of input process parameters is vital for obtaining the best possible output responses. This study employs the desirability approach, utilizing multi-response optimization to find the optimal solution. Multi-objective optimization involves using mathematical transformation functions to consolidate the impacts of different performance measures into a single desirability value. To achieve this single desirability value, two steps are required: (i) determining the desirability (d_i) and (ii) formulating the combined geometric mean (CDGM).

TH-3378_196103004

The first phase of optimization involves normalizing each performance measure (Q_i) to generate a desirability value (d_i), which falls within the range of 0 to 1. In this range, 0 represents the least desirable value, while 1 indicates the most desirable value. In the second phase, the combined geometric mean (CDGM) is applied to merge the performance measures into a single value once the desired state for each is achieved. The strategy aims to maximize layer height for an increased deposition rate and minimize layer width to enhance dimensional accuracy by reducing the stepover. Therefore, the optimization goals are set to maximize layer height and minimize layer width. The desirability functions for maximizing layer height, minimizing layer width, and CDGM are defined in Eqs. (A1.6), (A1.7), and (A1.8), respectively.

$$d_i(Q_i) = \begin{cases} 0, & Qi \le L_i \\ \left(\frac{H_i - Y_i}{H_i - L_i}\right)^w, & L_i < Qi < H_i \\ 1, & Qi \le H_i \end{cases} \quad \text{(A1.6)}$$

$$d_i(Q_i) = \begin{cases} 0, & Qi \le L_i \\ \left(\frac{H_i - Y_i}{H_i - L_i}\right)^w, & L_i < Qi < H_i \\ 1, & Qi \ge H_i \end{cases} \quad \text{(A1.7)}$$

$$CDGM = (d_1(Q_1) * d_2(Q_2) * \dots\dots\dots * d_l(Q_l)^{w_l})^{\frac{1}{l}} \quad \text{(A1.8)}$$

The symbols H_i, L_i, w, and l represent the higher value, lower value, weightage of each performance measure, and the total number of performance measures, respectively.

Table A1.5 Optimization study and range of input process parameters with weightage

		Limits		weightage		
Input parameter	Goal	Lower	Upper	Lower	Upper	Importance
V-Applied voltage	In range	3	5	1	1	3
Ss-Scanning speed	In range	80	120	1	1	3
F-Frequency	In range	100	300	1	1	3
Output parameter	Goal			Weightage		
Layer height (h) (µm)	Maximize			1		
Layer width (w) (µm)	Minimize			1		

The constraints for the optimization process are specified in Table A1.5. When all performance measures are assigned equal weightage and considered equally important, the

TH-3378_196103004

resulting desirability value is 0.96. Table A1.5 demonstrates that the input variables are kept within their specified ranges. In Table A1.6, the optimized results show a maximum layer height of 48 μm and a minimum layer width of 315 μm. These optimized values were achieved by using specific process parameter settings: 3.54 V applied voltage, 297 kHz frequency of current, and a scanning speed of 80 μm/s. The overall desirability for this optimal solution is 0.96.

A1.3.4 Validation of developed model

This section assesses the repeatability of the SJED manufacturing process and validates the ANOVA models. Three repeated tests are conducted at the optimized process parameter condition to validate the ANOVA models while ensuring the reliability and consistency of the SJED manufacturing process. The experiments are conducted for multi-layer (250-layer) deposition of 3 mm length, as illustrated in Fig. A1.5(a). The measured responses, which include layer height and width, are averaged along the deposition direction based on data collected from three repeated experiments. The 3D profilometer image of the same is presented in Fig. A1.5(b). The maximum values obtained for layer height and width are 45.5 μm and 305 μm, respectively, as demonstrated in Fig. A1.5(c). A percentage error of 5.20% for layer height and 3.17% for layer width, as indicated in Table A1.6, is observed when comparing the predicted results to the experimental results. These errors fall within an acceptable and feasible range, suggesting the repeatability and consistency of the process.

The profile obtained at optimized parameters is curve-fitted, as depicted in Fig. A1.5(c). Notably, the deposited bead conforms to a parabolic profile, demonstrating a high goodness of fit value (R^2) of 0.99. Following the optimization of results for a single bead, a multi-bead analysis is conducted using the same optimized parameters. This enables the application of the SJED process for coating purposes.

Table A1.6 Validation of predicted results from DOE with experimental results

Experimental conditions (V, Ss, and F)	Responses					
	Predicted		Experimental		% Error	
	h (μm)	w (μm)	h (μm)	w (μm)	h	w
3.54 V, 80 mm/min, and 297 kHz	48	315	45.5	305	5.20	3.17

TH-3378_196103004

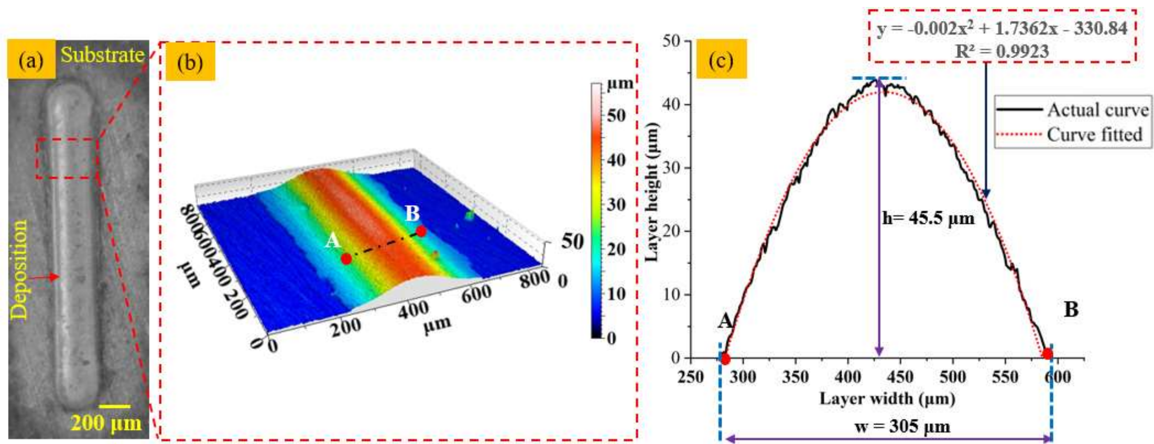

Fig. A1.5 (a) Deposited bead, (b) 3D and (c) 2D profile images of deposited bead at 3.54 V applied voltage, 297 kHz frequency of current, and 80 mm/min scanning speed

A1.3.5 Multi-bead optimization for flat surface condition

In this section, the height of the valley (hv) between adjacent beads is introduced as an additional criterion for assessing the flatness of multi-bead deposition. A lower valley height indicates a flatter surface. The main objective is to experimentally achieve a flat surface by minimizing the valley height through adjustments in the center distance (d) between adjacent beads. The single-bead optimized process parameter conditions of 3.54 V applied voltage, 80 mm/min scanning speed, and 297 kHz current frequency, as discussed in Section A1.3.3, are employed for subsequent multi-bead optimization.

Experiments were conducted on overlapping bead profiles with varying center distances (d). Fig. A1.6(a), Fig. A1.7(a), and Fig. A1.8(a) display the deposited multi-beads corresponding to d=0.55w, d=0.50w, and d=0.45w, respectively. The 3D profile images of the same are presented in Fig. A1.6(b), Fig. A1.7(b), Fig. A1.8(b). The analysis presented in Fig. A1.6(c), Fig. A1.7(c), and Fig. A1.8(c) suggests that as the center distance (d) increases, the valley height (hv) also increases. It can be observed clearly from Fig. A1.8 (c) that the valley height becomes nearly zero (hv $\approx$ 0) when the center distance equals 0.45 times the layer width (d=0.45w). This center distance (d=0.45w) can be considered the optimal condition for generating flat deposition. This optimized flat surface condition (d=0.45w) can provide a lesser number of voids along with high dimensional accuracy, which can be further utilized for coating purposes.

TH-3378_196103004

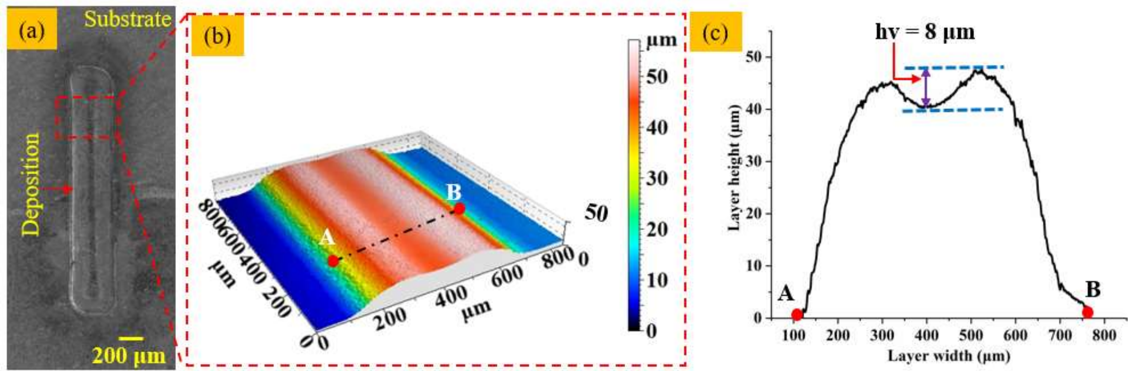

Fig. A1.6 (a) Deposited multi-bead, (b) 3D and (c) 2D profile images at d= 0.55w

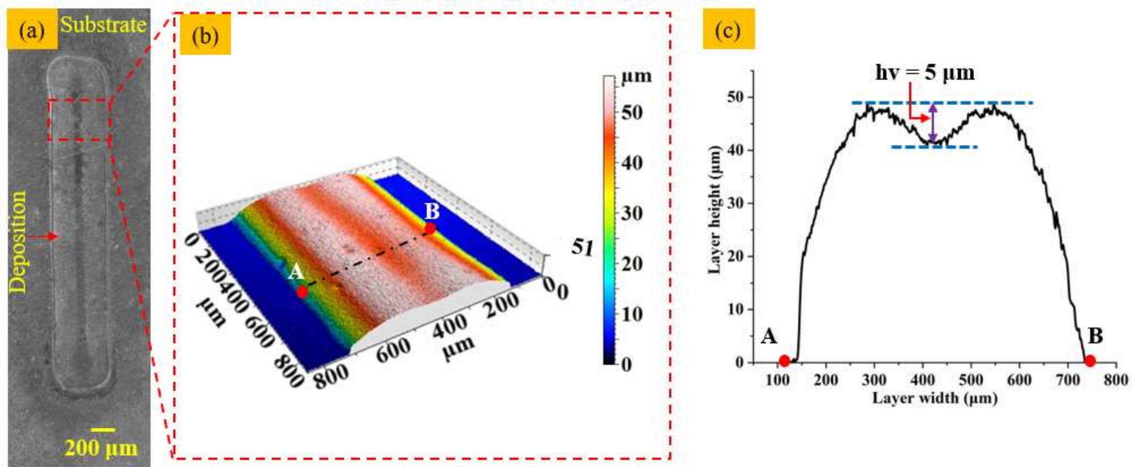

Fig. A1.7 (a) Deposited multi-bead, (b) 3D and (c) 2D profile images at d= 0.50w

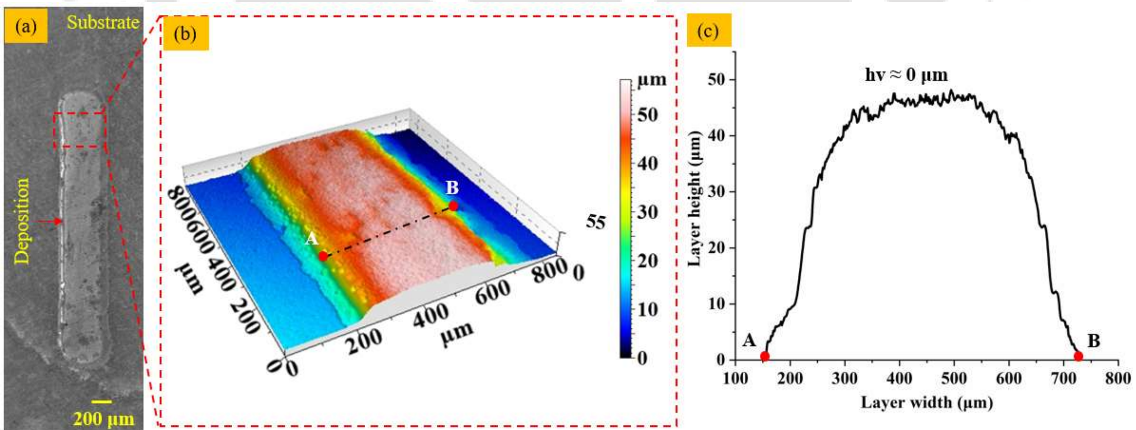

Fig. A1.8 (a) Deposited multi-bead, (b) 3D and (c) 2D profile images at d= 0.45w

A1.3.6 Summary

This chapter discussed the development of the SJED setup for the deposition of copper. The effect of input process parameters such as applied voltage, frequency of current, and scanning speed on the deposition profile is investigated. Single-bead multilayer

experiments were carried out to optimize the input parameters using desirability approach .The optimized results show a maximum layer height of 48 μm and a minimum layer width of 315 μm. These optimized values were achieved using specific process parameter settings: 3.54 V applied voltage, 297 kHz frequency of current, and a scanning speed of 80 μm/s. The overall desirability for this optimal solution is 0.96. Multi-bead experiments are performed to achieve a flat surface condition for uniform and void-free deposition. The center distance of 0.45w for the flat surface condition is obtained experimentally.

TH-3378_196103004

Appendix A2 Experimental investigation of electrochemical deposition-based micro-additive manufacturing process

A2.1 Introduction

Microstructures with a high aspect ratio have multiple applications, like, in integrated hydro and thermodynamic microsystems[122], life science[123], micro-robotics[124], and countless utilization in other fields such as micro-sensors, actuators, and miniature devices. Few *Additive Manufacturing* (*AM*) techniques like selective laser melting (SLM)[125], electron beam melting (EBM), and directed energy deposition (DED) are capable of fabricating macro parts where regulated deposition can be achieved, which enables constricted geometries. However, the parts manufactured by these processes have very high residual stress as heat energy is utilized to melt the metal while manufacturing. Most of these processes require further post-heat treatment to release residual stress. They also have other drawbacks, such as limitations on component size because of laser spot diameter, excessive heat input, larger powder particle size, etc. To overcome these limitations, an electrochemical-based AM process known as *Localized Electrochemical deposition (LED)* is developed in the present study.

Electrochemical deposition, also known as electroplating, is popularly used to add a metal layer of 2-3 μm thickness on a substrate. However, in LED, a particular type of electroplating process, a micro-electrode is used as an anode and a relative motion is provided between the conductive substrate (i.e., cathode) and the micro-electrode. In the LED process, the material is deposited atom-by-atom in the desired region with a higher deposition rate. As shown in Fig. A2.1, the LED process involves immersing a micro-electrode inside an electrolyte chamber containing reducible metal ions. Also, the micro-electrode is carefully positioned close to the conducting substrate maintaining a small inter-electrode gap (IEG) in the micron range. Apart from an exposed area at the tip, the electrode is insulated from all surfaces. A faradic current travels through the electrolytic solution between the tool and the substrate when a potential difference is applied between them. The current flow initiates an oxidation reaction at the tool's tip, which causes metal ions to deposit on the substrate.

TH-3378_196103004

The deposition current density can be varied by changing the inter-electrode gap (i.e., IEG). The microelectrode moves on a predefined trajectory based on the G code provided to the controller of the XYZ table while fabricating a required shape in a horizontal plane. Further, this process is extended to multiple layers while fabricating 3D objects.

LED is a type of AM process that can print micro-components or features directly at an atomic level at a specific location without using a mask or supporting material.[39] Unlike the AM process, the LED process does not require additional thermal energy sources; hence, the generated residual stress is negligible due to the Ohmic heating of the electrodes. [79] However, because of lattice mismatch during the growth of the film, some stresses, often referred to as intrinsic stress, may be generated.[126], [127] Most studies by previous researchers on LED are focused mainly on how process variables affect deposition rate and quality in the direction normal to the substrate surface.[128] Giar et al.[129] found that for deposition to occur, the applied voltage between the micro-anode and substrate should exceed a particular threshold value. However, the deposition rate drops at a very high voltage due to aggressive bubble formation and ion depletion.[129] They also observed that at a very high voltage, the deposition becomes irregular in shape and powdery. A maximum localization with faster ion migration is achieved when an optimum inter-electrode gap (IEG) is maintained for a given voltage and tool diameter. An ion depletion region is developed below this IEG; hence, a nonuniform deposition can be observed.[130] The average deposition rate decreases with increased IEG. [46]

The electrolyte concentration plays an insignificant role in the deposition rate; however, the deposited structure becomes rough, spongy, irregular, and porous with decreased electrolyte concentration.[129], [131] A smooth and fined-grained structure is obtained when the organic additives are mixed with the electrolyte proportionally. [40]

Manukyan et al.[132] reported that the frequency of current has an insignificant effect on the deposition rate; However, using an ultra-high-frequency pulse current, the deposition can be constricted to a smaller area than the tool size. Kamaraj and Sundaram[48] reported that the pulse power with a duty ratio of 0.75 gives the highest deposition rate than a lower duty ratio. However, Qian Ningkai et al.[130] observed that the duty ratio has the least impact on the deposition process out of three input factors, i.e., applied voltage, IEG, and duty ratio. Furthermore, the advantage of using pulse current decreases with an increased interelectrode gap due to the availability of more ions at a higher inter-electrode gap.[48] Due to the pulse current during LED, components with higher strength are produced than those with a DC power source, as observed by Daryadel et al. [45]. Giar et al.[129] reported

that the deposition will be irregular when the tool withdrawal rate is greater than the deposition rate. To overcome this issue, Said[44] developed an adaptive tool withdrawal method based on monitoring the current gradient rather than the value of the current. The improved tribological properties of the deposit were found with the addition of a mechanical rotary and ultrasonic vibration system.[133] Many mathematical models have been formulated to determine the relationship between the input process parameters and output responses, i.e., deposition rate, deposition quality, etc., during the LED process.[26], [134]

Most studies on the LED process are primarily based on the deposition rate calculation perpendicular to the base plate while considering the anode to move only in the Z direction. However, for depositing a 3D complex object using LED, the tool moves simultaneously in all three coordinate axes (i.e., XYZ axes). Hence, further study is necessary to determine the layer height and width at different process parameter conditions. The deposition resolution is governed by the minimum layer height in a single pass. Smaller layer heights and finer deposits can achieve improved component strength. Layer width decides the stepover, and an improper stepover can give a porous structure. Since LED is a micro-deposition method that allows 3D structures to be generated layer by layer, the accurate prediction of layer height and layer width for a set of process parameters is essential; otherwise, geometrical errors could be imparted in the next deposited layer.

The present work investigates the effects of the frequency of the current, applied voltage, scanning speed, and inter-electrode gap on the deposited layer height and width using an indigenously developed LED setup based on statistical design of experiments (DOE). The process parameters and their ranges are determined using preliminary experimental studies and prior studies by previous researchers. A single bead of 5 mm in length is deposited during each experiment under DOE. The geometric features obtained from the depositions are measured using a microscope and non-contact type profilometer. The capability of the developed LED process is also studied while fabricating a component having application in the micro-manufacturing field.

TH-3378_196103004

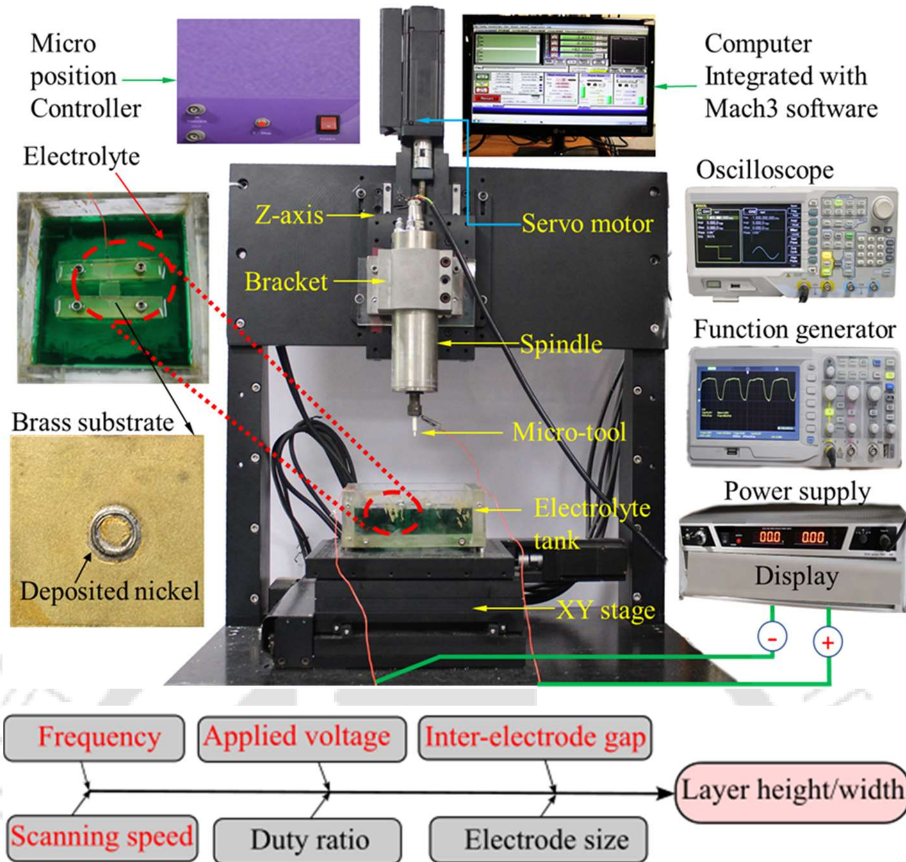

Fig. A2.1 Localized electrochemical deposition (LED) experimental setup and input & output process variables

A2.2 Materials and method

The deposition is performed experimentally by utilizing the developed LED setup shown in Fig. A2.1. It consists of various parts, such as a CNC-controlled X-Y table with an independent Z axis, power supply, electrolyte container, spindle, electrode holder, etc. All three axes of the XYZ stage are connected to a servo motor having 0.1 μm resolution. An arbitrary function generator is connected to the power supply to set the frequency and waveform types.

A platinum wire of 300 μm diameter is used to fabricate the micro-tool. The wire is coaxially held in a specially designed plastic tube and is fixed using a cold-setting resin to get a Pt-centric conical cylinder. To expose a disk-like end with a diameter of 300 μm, the bottom end of the cylinder is polished with emery papers of varying grits (800 –1500) and further wet polished with Al_2O_3. The cross-sectional view of the CAD model of the LED tool is shown in Fig. A2.2. Platinum is selected as a tool material due to its chemical inertness with the electrolyte and stability under the experimental environment.[135] The

TH-3378_196103004

cathode in the present study is made of brass (20 ×20 ×3 mm^3) which has a mirror-like finished surface achieved after wet polishing using emery paper.

The electrolyte used in this work is a Watt's bath, which has less throwing power than other nickel-based electrolytes. It contains nickel chloride (45 g), boric acid (30 g), and nickel sulfate (240 g), per liter of distilled water. Nickel sulfate supplies the majority of the cations necessary for deposition. In contrast, nickel chloride increases the solution's conductivity and helps in achieving fine-grained deposition.[136] Boric acid is a pH buffer. The electrical conductivity of the electrolyte is measured as 5.2 s/m.

Based on the review of the literature survey and preliminary experimental results, the following process parameters, i.e., applied voltage, frequency, scanning speed, and inter-electrode gap (IEG), and their ranges have been selected to examine their effects on the output responses[42], [48]. The duty ratio for all experiments is fixed at 75%, as it gives the best deposition compared to lower duty ratios.[48] A statistical design of experiments has been formulated to investigate the relationship between the process parameters with output responses. Table A2.1 displays the process parameter levels (3 levels) and ranges.

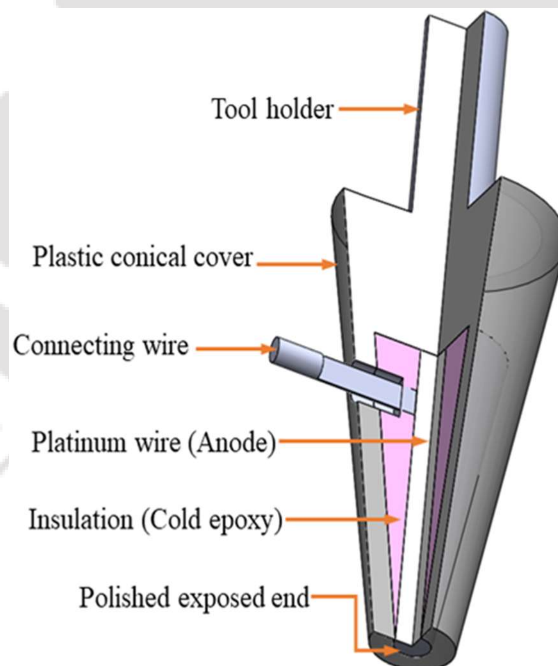

Fig. A2.2 Cross-sectional view of LED tool CAD model

TH-3378_196103004

Table A2.1 Process parameters and their levels

Parameters	Unit	Levels -1	Levels 0	Levels +1
Applied Voltage (V)	Volt	3	4	5
Inter-electrode gap (I_g)	µm	5	7.5	10
Frequency (F)	kHz	100	300	500
Scanning speed (S)	µm/s	1	3	5
Constant parameter: Duty cycle		75%		

Table A2.2 Statistical design of experiments with responses

Exp. No.	Process parameters: Voltage (V)	IEG (µm)	Frequency (kHz)	Scanning speed (µm/s)	Responses: Layer height, h (µm)	Layer width, w (µm)
1	3	5	100	5	0.98	360
2	5	5	100	1	4.3	372
3	5	10	500	5	1.2	410
4	3	5	100	1	3.7	361
5	4	7.5	300	5	1.05	361
6	4	7.5	300	3	3.1	360
7	3	5	500	1	3.9	342
8	5	10	100	5	1.02	423
9	3	10	100	5	0.53	393
10	4	7.5	300	3	2.5	358
11	4	7.5	300	3	3.2	357
12	4	5	300	3	3.5	354
13	4	7.5	100	3	2.9	372
14	3	5	500	5	1.1	342
15	3	10	100	1	1.8	393
16	5	10	100	1	2.1	423
17	3	10	500	1	1.98	375
18	4	7.5	500	3	3	353
19	4	7.5	300	1	3.98	363
20	4	7.5	300	3	2.9	361
21	5	5	100	5	1.3	372
22	3	7.5	300	3	1.38	356
23	4	7.5	300	3	2.8	362
24	5	5	500	5	1.58	351
25	5	10	500	1	2.3	410
26	4	7.5	300	3	2.8	360
27	5	5	500	1	4.6	351
28	3	10	500	5	0.57	375
29	5	7.5	300	3	1.49	370
30	4	10	300	3	1.2	391

TH-3378_196103004

The experiments were planned, performed, and analyzed using central composite design (CCD) of statistical design experiment (DOE). The total number of experiments can be obtained by Eq. (A2.3).

$$N = 2^v + 2v + v_c \tag{A2.3}$$

Where N denotes the total number of experiments, v denotes the number of process variables, and v_c represents the center points. Four process parameters and six center points have been selected to design and carry out thirty experiments for the present study. Table A2.2 contains the relevant experimental scheme. A total of three experiments are carried out for each experimental condition to avoid interference from the experiments, and the average values of the responses along the deposition length are calculated. Trial experiments are conducted to verify the setup's functionality and suitability within a specified range of input parameters. The responses, i.e., layer height (h) and layer width (w) are measured with a high precision non-contact type computerized surface profilometer (Talysurf CCI; Taylor Hobson). The measurements are taken at various points along the length of the deposited structure, and an average value of output response is calculated, as shown in Table A2.2.

`

A2.3 Results and discussion

Analysis of variance (ANOVA) is carried out for both responses, i.e., layer height and width, as shown in Table A2.3 and Table A2.4, respectively, providing a lack-of-fit test and test for the significance of the models. The significance of the model is evaluated using the F-values in the ANOVA table. The P-value shows the model structure's reliability at a 95% confidence level. The p-values of the models are in Table A2.3 and Table A2.4 are less than 0.05, meaning the models are significant, but the lack-of-fit fit terms are not significant; hence, both meet the requirements for a model. The value of the coefficient of multiple determination (R^2) for layer height and width is found to be 0.95 and 0.99, respectively. In both cases, the value of R^2 is near unity. Based on responses shown in Table A2.2, quadratic models are developed for both layer height and width. The regression model best explains the relationship between the input parameters and the output responses. The regression equations for layer height (h) and width (w) are provided in Eqs. (A2.4) and (A2.5), respectively.

TH-3378_196103004

$$
\begin{aligned}
h = 2.68 &+ 2.19 \times 10^{-2}V - 68.11 \times 10^{-2}I_g + 8.89 \times 10^{-2}F - 1.07S \\
&- 22.5 \times 10^{-3}VI_g + 2.62 \times 10^{-2}VF - 18.80 \times 10^{-3}I_gF \\
&+ 41.75 \times 10^{-2}I_gS - 1.62 \times 10^{-2}FS - 1.04V^2 - 0.13{I_g}^2 \\
&+ 0.48F^2 + 4.15 \times 10^{-2}S^2
\end{aligned} \tag{A2.4}
$$

$$
\begin{aligned}
w = 360.04 &+ 10.28V + 21.56I_g - 8.89F - 16.67 \times 10^{-2}S + 5.56VI_g \\
&+ 31.25 \times 10^{-2}VF + 6.25 \times 10^{-2}VS + 1.06I_gF \\
&+ 6.25 \times 10^{-2}I_gS + 6.5 \times 10^{-2}FS + 2.58V^2 + 12.08{I_g}^2 \\
&+ 2.08F^2 + 1.58S^2
\end{aligned} \tag{A2.5}
$$

Where V, I_g, F, and S signify applied potential, IEG, frequency, and scanning speed, respectively.

A2.3.1 Effect of process parameters

The following section describes the individual effects of applied voltage, frequency, inter-electrode gap, and scanning speed on layer height and width.

Applied voltage

The current density increases with an increased applied voltage, causing more ion deposition. Hence, layer height increases to a critical voltage of 4V, as shown in Fig. A2.3(a). Beyond this critical voltage, deposition height decreases due to aggressive bubble formation and ion depletion at a higher current.[129] Investigations are carried out in a single-layer experiment where the deposition was carried out at 5V. A nonuniform and comparatively lower layer height, as shown in Fig. A2.4(a), Fig. A2.4(b), and Fig. A2.4(c), are observed. The deposition width increases with increased applied voltage, as shown in Fig. A2.3(a). Rapid ionic reaction leads to vigorous bubble formation; therefore, the turbulence generated due to the bubble formation also increases. Hence, the current density is not confined and spreads over more surface area.

Inter-electrode gap (IEG)

With an increase in IEG, the current density decreases; hence, the rate of reaction decreases, which causes less ion deposition. Consequently, the layer height decreases with increased IEG[42], as shown in Fig. A2.3(b). However, the layer width increases with increased IEG,

TH-3378_196103004

as shown in Fig. A2.3(b). It is due to the non-localized current density at higher IEG, which results in a wider deposition width.

Frequency

The effect of current frequency over the deposited layer height is negligible compared to other parameters[48] because of the constant energy that consists of the amplitude of voltage and duty ratio, as shown in Fig. A2.3(c). According to Fig. A2.3(c), the layer's width decreases as frequency increases as the current in the electrolyte at the cathode surface reaches the steady-state condition more quickly at a higher frequency, leading to a more confined current density and a simultaneous increase in the confined deposition.[137]

Scanning speed

The effect of scanning speed on the layer height is highest compared to other parameters considered in the present study. It is found that the layer height decreases with the increase of the scanning speed, as shown in Fig. A2.3(d). It is observed that at the highest scanning speed of 5 μm/s, the layer height of 2.5 μm is achieved.

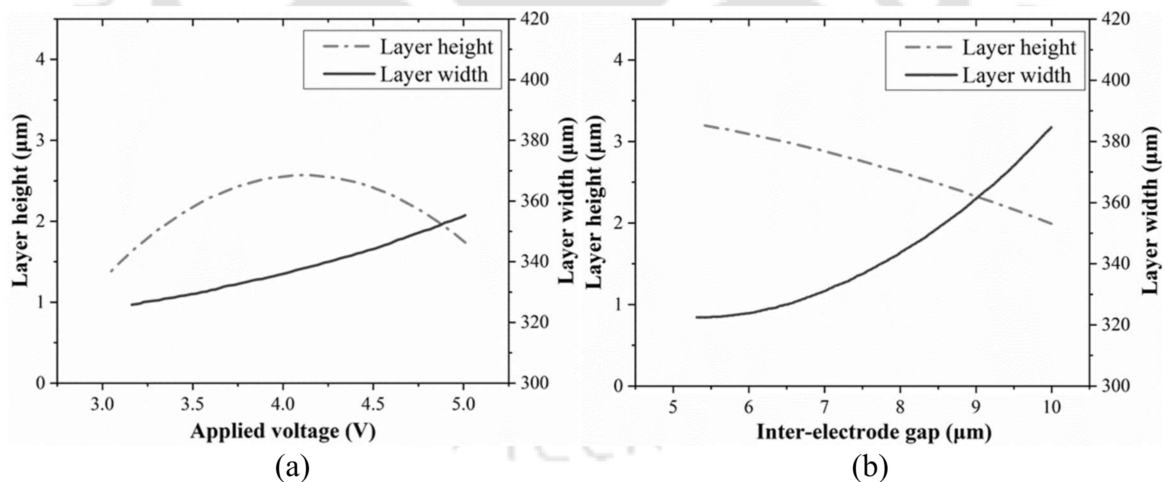

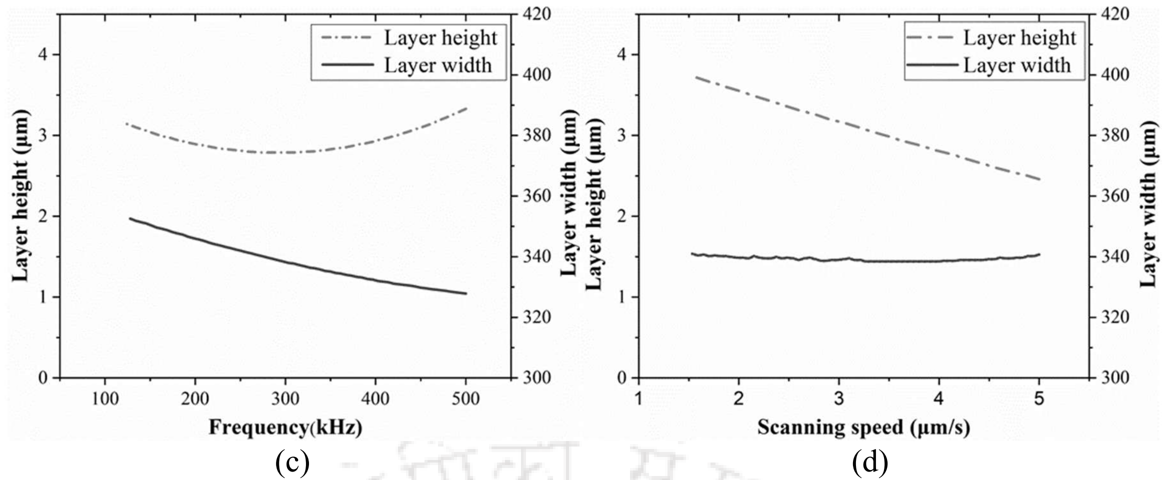

Fig. A2.3 Effect of (a) applied voltage, (b) inter-electrode gap, (c) frequency, and (d) scanning speed on layer height and width

At a higher scanning speed, the reaction time at a particular point on the cathode surface is less, leading to less ion deposition.[48] An insignificant effect on the deposited layer width is observed with scanning speed in the selected range, as shown in Fig. A2.3(d). With changing scanning speeds, there is no change in the current density as the other parameters are kept constant.

Table A2.3 ANOVA for layer height

Source	Sum of Squares	df	Mean Square	F-value	p-value	Remarks	% Contribution
Model	37.74	14	2.70	21.56	< **0.0001**	significant	
V-Applied voltage	0.8668	1	0.8668	6.93	**0.0188**	significant	2.39
I_g-Inter electrode gap	8.35	1	8.35	66.79	< **0.0001**	significant	22.96
F-Frequency	0.1422	1	0.1422	1.14	0.3030		0.39
S-Scanning speed	20.76	1	20.76	166.03	< **0.0001**	significant	57.09
VI_g	0.0081	1	0.0081	0.0648	0.8025		0.02
VF	0.0110	1	0.0110	0.0882	0.7706		0.03
VS	0.0000	1	0.0000	0.0000	1.0000		0
I_gF	0.0056	1	0.0056	0.0450	0.8349		0.01
I_gS	2.79	1	2.79	22.31	**0.0003**	significant	7.67
FS	0.0042	1	0.0042	0.0338	0.8566		0.02
V^2	2.79	1	2.79	22.35	**0.0003**	significant	7.67
I_g^2	0.0395	1	0.0395	0.3161	0.5823		0.10
F^2	0.5883	1	0.5883	4.71	**0.0466**	significant	1.62
S^2	0.0045	1	0.0045	0.0357	0.8527		0.02
Lack of Fit	1.57	10	0.1567	2.54	0.1575	Not-significant	

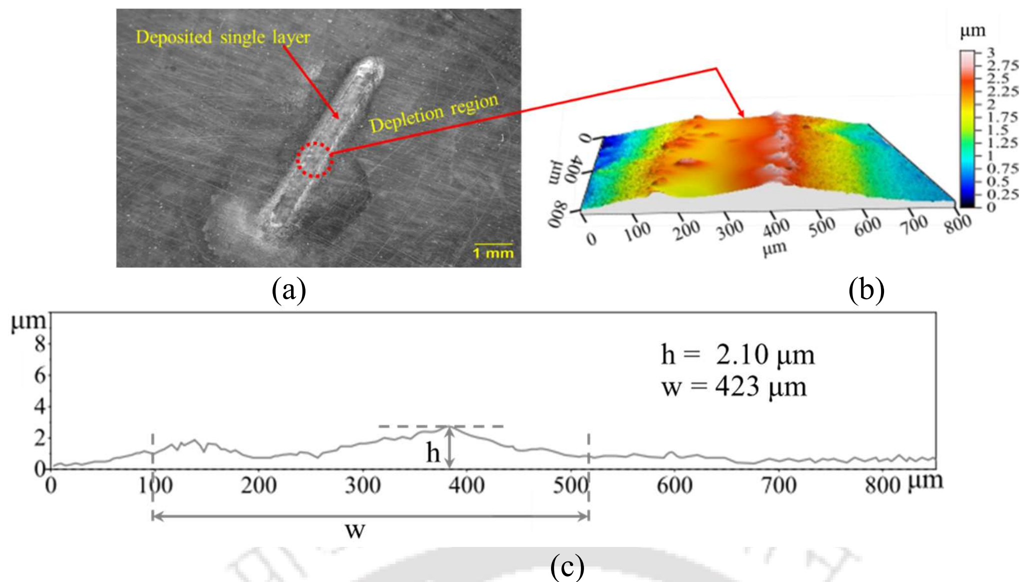

Fig. A2.4 (a) Optical microscopic image of deposited single layer at 5V applied voltage, 100 kHz frequency, 10 µm IEG, and 1 µm/s scanning speed; (b) 3D and (c) 2D optical profilometer images of deposited single layer

Table A2.4 ANOVA for layer width

Source	Sum of Squares	df	Mean Square	F-value	p-value	% Contribution
Model	14265.71	14	1018.98	188.10	**< 0.0001***	
V-Applied voltage	1901.39	1	1901.39	351.00	**< 0.0001***	15.07
I_g-Inter electrode gap	8363.56	1	8363.56	1543.92	**< 0.0001***	66.30
F-Frequency	1422.22	1	1422.22	262.54	**< 0.0001***	11.28
S-Scanning speed	0.5000	1	0.5000	0.0923	0.7654	0.003963
VI_g	495.06	1	495.06	91.39	**< 0.0001***	3.93
VF	1.56	1	1.56	0.2884	0.5991	0.02
VS	0.0625	1	0.0625	0.0115	0.9159	0
I_gF	18.06	1	18.06	3.33	0.0878	0.15
I_gS	0.0625	1	0.0625	0.0115	0.9159	0
FS	0.0625	1	0.0625	0.0115	0.9159	0
V^2	17.23	1	17.23	3.18	0.0947	0.14
I_g^2	378.02	1	378.02	69.78	**< 0.0001***	3
F^2	11.20	1	11.20	2.07	0.1710	0.09
S^2	6.46	1	6.46	1.19	0.2921	0.06
Lack of Fit	63.92	10	6.39	1.84	0.2590**	

*Significant, ** Not-significant

A2.3.2 Combined effect of process parameters

The ANOVA results are in Table A2.3 and Table A2.4 demonstrate the cumulative impact of the input variables over output responses. Based on the actual results of each input parameter's impact on the output responses, there is a conflict in determining the best process parameter conditions. Hence, it is required to simultaneously examine the combined impact

of all the input parameters to get the desired responses while achieving the best and most feasible solution. A multi-response optimization study [138], [139] is carried out to find the best solution in the present work. The following subsections describe the interaction of applied voltage, frequency, inter-electrode gap, scanning speed, and their combined effect on layer height and width.

Layer height

The 3D plot in Fig. A2.5(a) illustrates the combined influence of applied voltage and inter-electrode gap on layer height. It shows a significant decrease in layer height beyond critical voltage (4V).

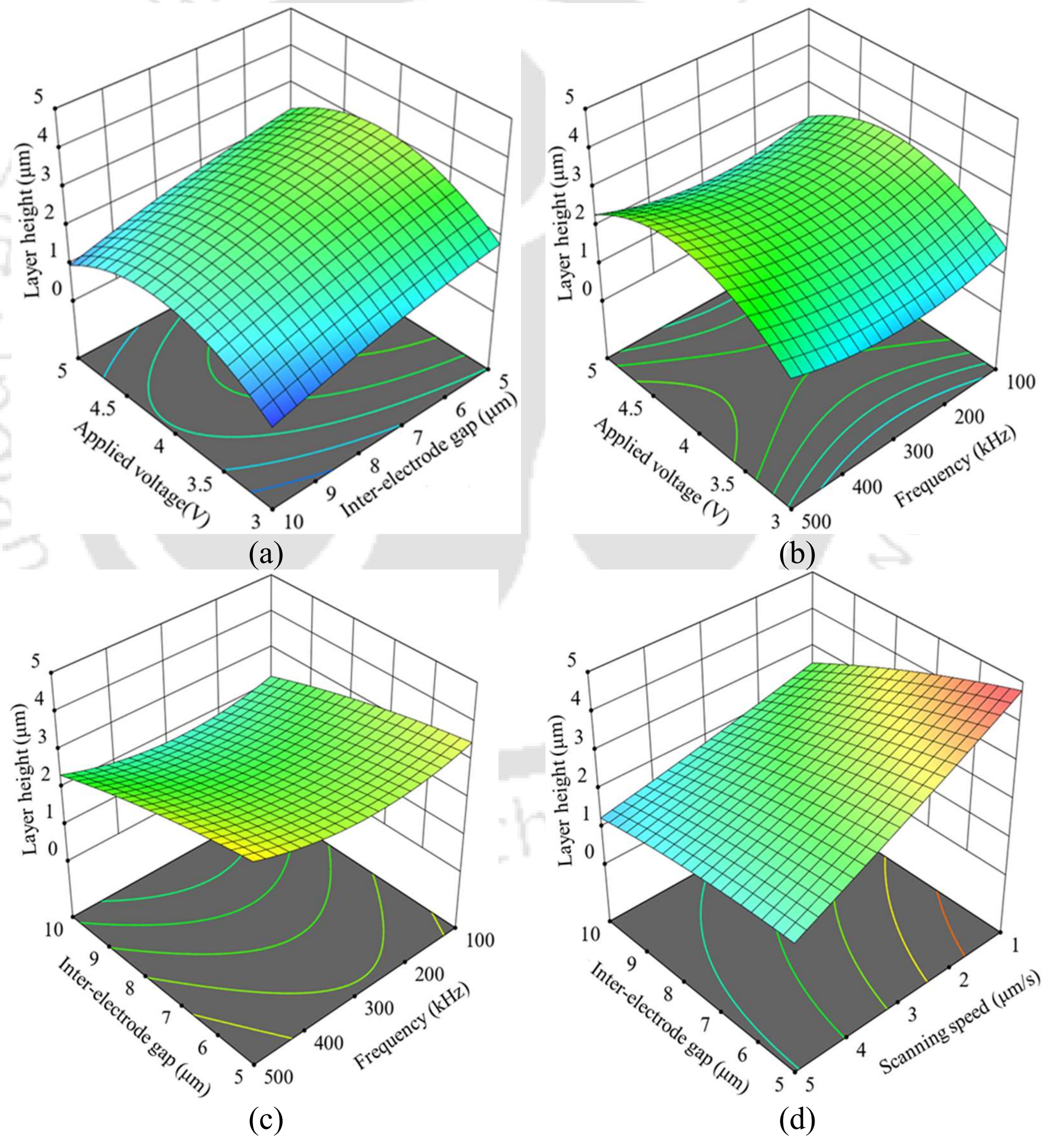

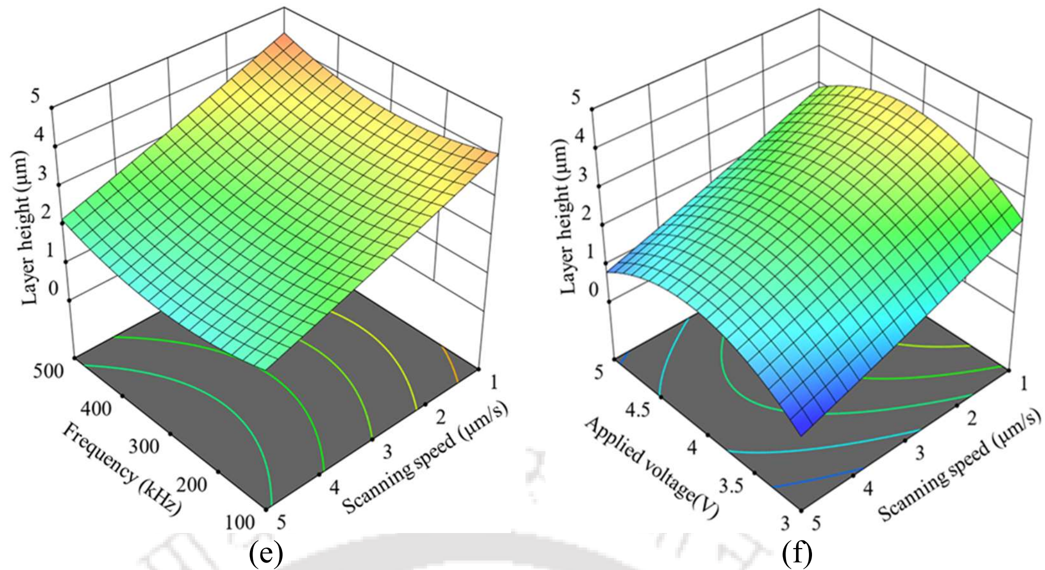

Fig. A2.5 Combined effect of (a) IEG and applied voltage, (b) frequency and applied voltage, (c) frequency and IEG, (d) scanning speed and IEG, (e) scanning speed and frequency, and (f) scanning speed and applied voltage on layer height

This can be attributed to the fact that voltage beyond critical value causes more ionic reactions, leading to vigorous bubble formation and disrupting growth.

The combined effect of applied voltage and frequency on layer height is shown in Fig. A2.5(b). A higher impact of the applied voltage than the current frequency is observed on the layer height because of the constant energy consisting of voltage amplitude and duty ratio.[48] The combined effect of IEG and frequency on the layer height is shown in Fig. A2.5(c). The IEG is a strong function of current density; hence with an increase in IEG, a significant decrease in layer height is found. Fig. A2.5(d) represents the combined effect of scanning speed and IEG on layer height. It is noticed that the layer height increases with a decrement in scanning speed and IEG. This is because the available ionic reaction time is greater at the lower scanning speed and higher current density at lower IEG. The combined effect of scanning speed and frequency on layer height has been presented in Fig. A2.5(e). It is noticed that, in comparison to frequency, scanning speed has a more significant impact on layer height. Fig. A2.5(f) shows how applied voltage and scanning speed jointly affect the layer height. It is identified that scanning speed has a more significant impact than the applied voltage.

Layer width

The 3D plot in Fig. A2.6(a) illustrates the combined impact of applied voltage and IEG on layer width. The response surface plot indicates that the layer width increases with an

TH-3378_196103004

increase in both applied voltage and IEG. Furthermore, the influence of IEG on layer width is greater than that of the applied voltage, as the current density highly depends on the IEG. At lower IEG, the current density is highly constricted into a smaller area than at higher IEG, leading to a focused deposition width. Fig. A2.6(b) represents the combined effect of scanning speed and IEG. It is observed that the layer width decreases with a decrement in IEG, and there is an insignificant variation in layer width with the scanning speed. The combined effect of IEG and frequency on the layer width is shown in Fig. A2.6(c). It is found that the layer width reduces with increased frequency; as frequency rises, the steady state condition of current inside the electrolyte reaches more quickly at the cathode, resulting in a confined current density and a more consistent deposition process.[137] Fig. A2.6(d) represents the combined effect of frequency and applied voltage on layer width.

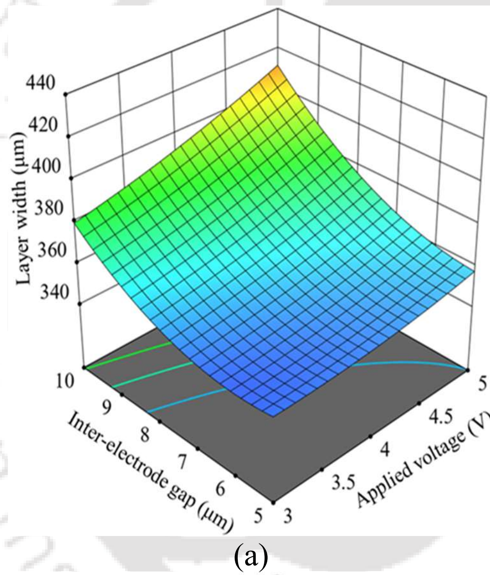

(a)

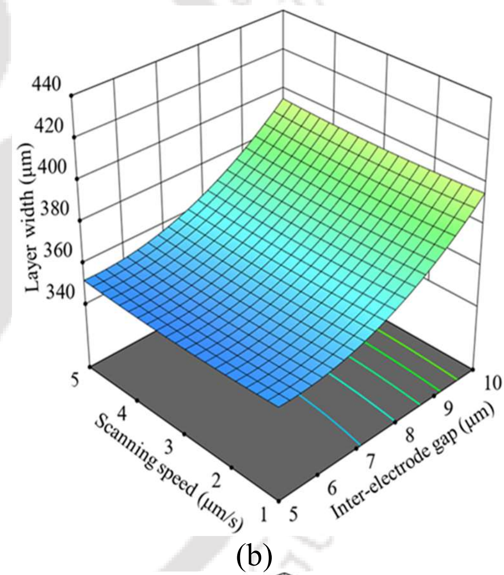

(b)

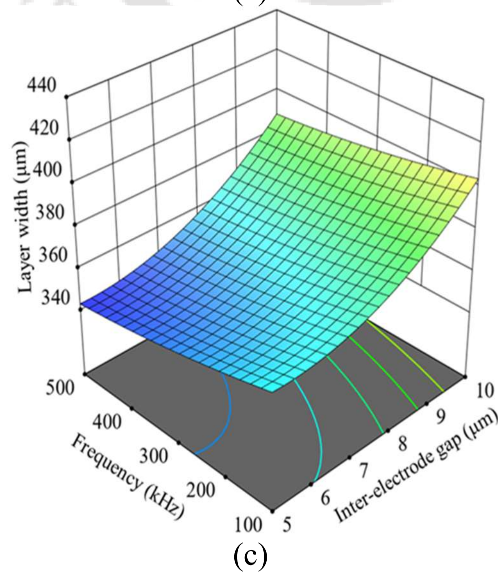

(c)

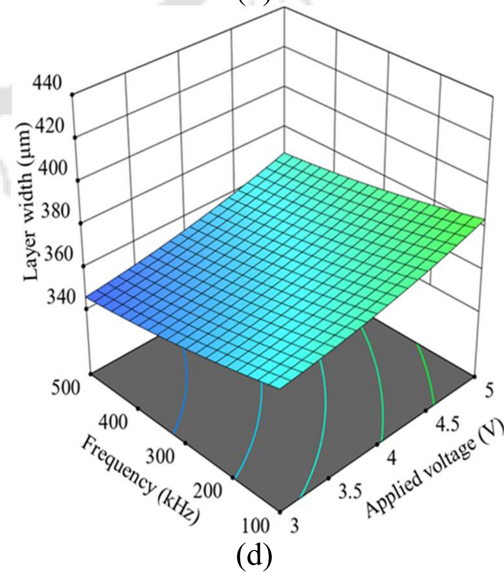

(d)

TH-3378_196103004

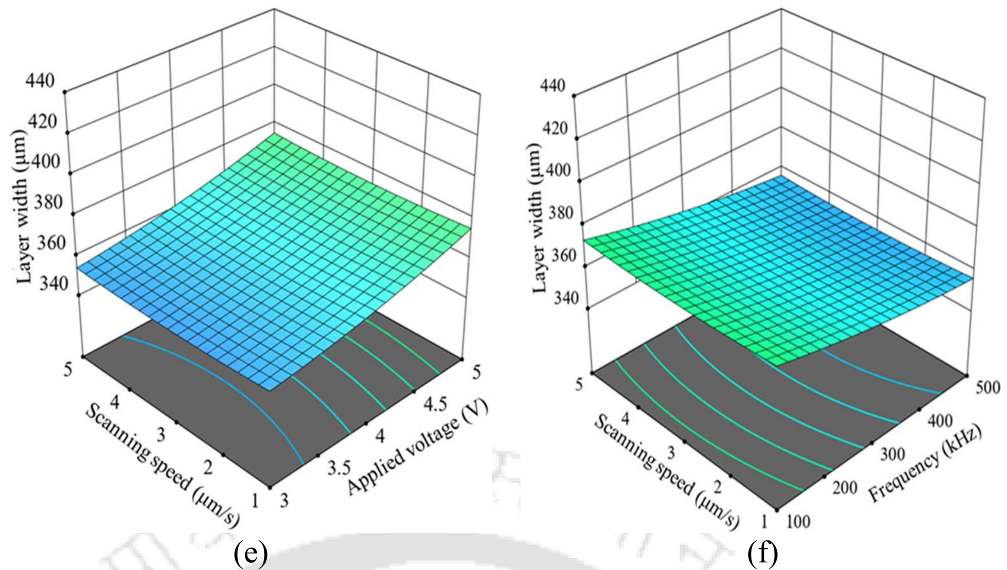

Fig. A2.6 Combined effect of (a) applied voltage and IEG, (b) IEG and scanning speed, (c) IEG and frequency, (d) applied voltage and frequency, (e) applied voltage and scanning speed, and (f) frequency and scanning speed on layer width

It is observed that layer width increases with increased applied voltage due to high ion deposition; however, its value reduces with increased frequency for the same reason. Fig. A2.6(e) shows the combined effect of scanning speed and applied voltage.

An insignificant effect of scanning speed on layer width is noticed. It is observed that layer width increases as the voltage increases. Fig. A2.6(f) represents the effect of scanning speed and frequency on layer width. A lesser impact of scanning speed on layer width is observed. It can be seen that layer width decreases with increased frequency.

A2.3.3 Optimization study

The desirability approach using multi-response optimization is used in the present study to find the optimum solution (as discussed in section A1.3.3). The constraints of the optimization are listed in Table A2.5. For equal weightage and the equal importance of all the performance measures, the desirability achieved is 0.97.

TH-3378_196103004

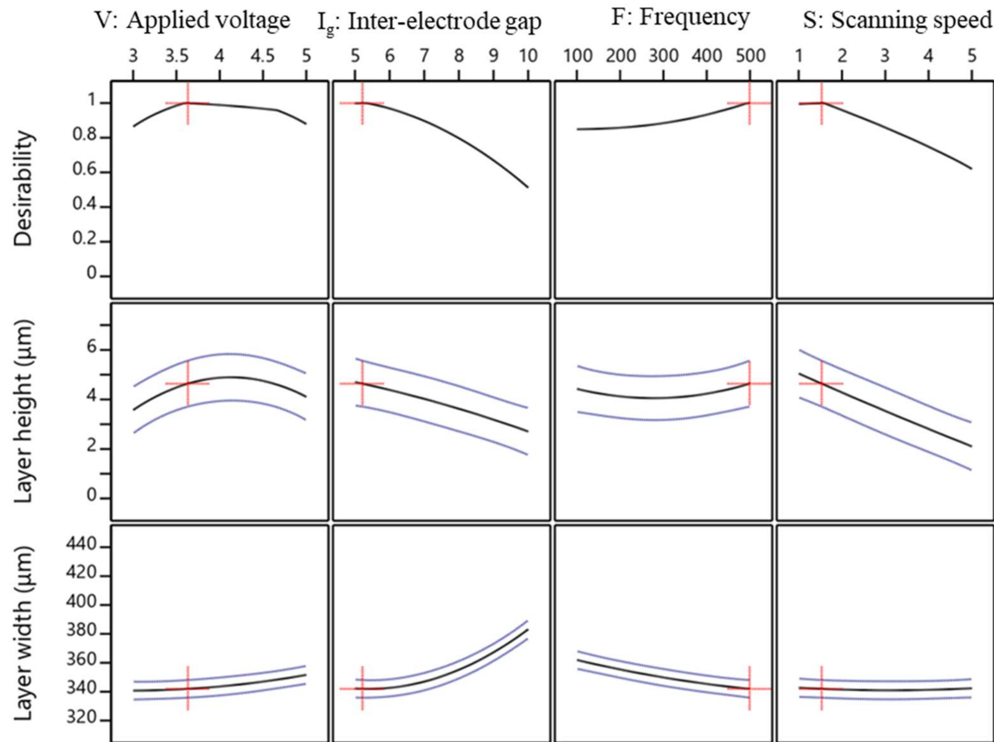

Fig. A2.7 Optimization graph of Layer height and width

As shown in Table A2.5, the input variables are considered within their range. Table A2.6 shows the optimized maximum value of 4.60 µm layer height and minimum value of 341.93 µm layer width obtained at optimized process parameter values of 3.57 V applied voltage, 5.38 µm IEG, 497 kHz frequency, and 1.41 µm/s scanning speed with the desirability of 0.97 at the best optimal solution as shown in Fig. A2.7.

Table A2.5 Optimization study and range of input process parameters with weightage

Input parameter	Goal	Limits		Weightage		Importance
		Lower	Upper	Lower	Upper	
V-Applied voltage	in range	3	5	1		3
I_g-Inter-electrode gap	in range	5	10	1		3
F-Frequency	in range	100	500	1		3
S-Scanning speed	in range	1	5	1		3
Output parameter	**Goal**			**Weightage**		
Layer height (h) (µm)	maximize			1		
Layer width (w) (µm)	minimize			1		

A2.3.4 Validation of ANOVA model

This section discusses the LED process's repeatability with the ANOVA models' validation. Three repeated confirmatory tests are performed at optimized process parameter conditions to validate the ANOVA model. Experiments are performed for the single-layer deposition,

TH-3378_196103004

as shown in Fig. A2.8(a). An average value is calculated from measured responses (i.e., layer height and width) along the deposition direction from 3 repeated experiments. The maximum layer height and width are 4.35 μm and 325 μm, respectively, as shown in Fig. A2.8(c).

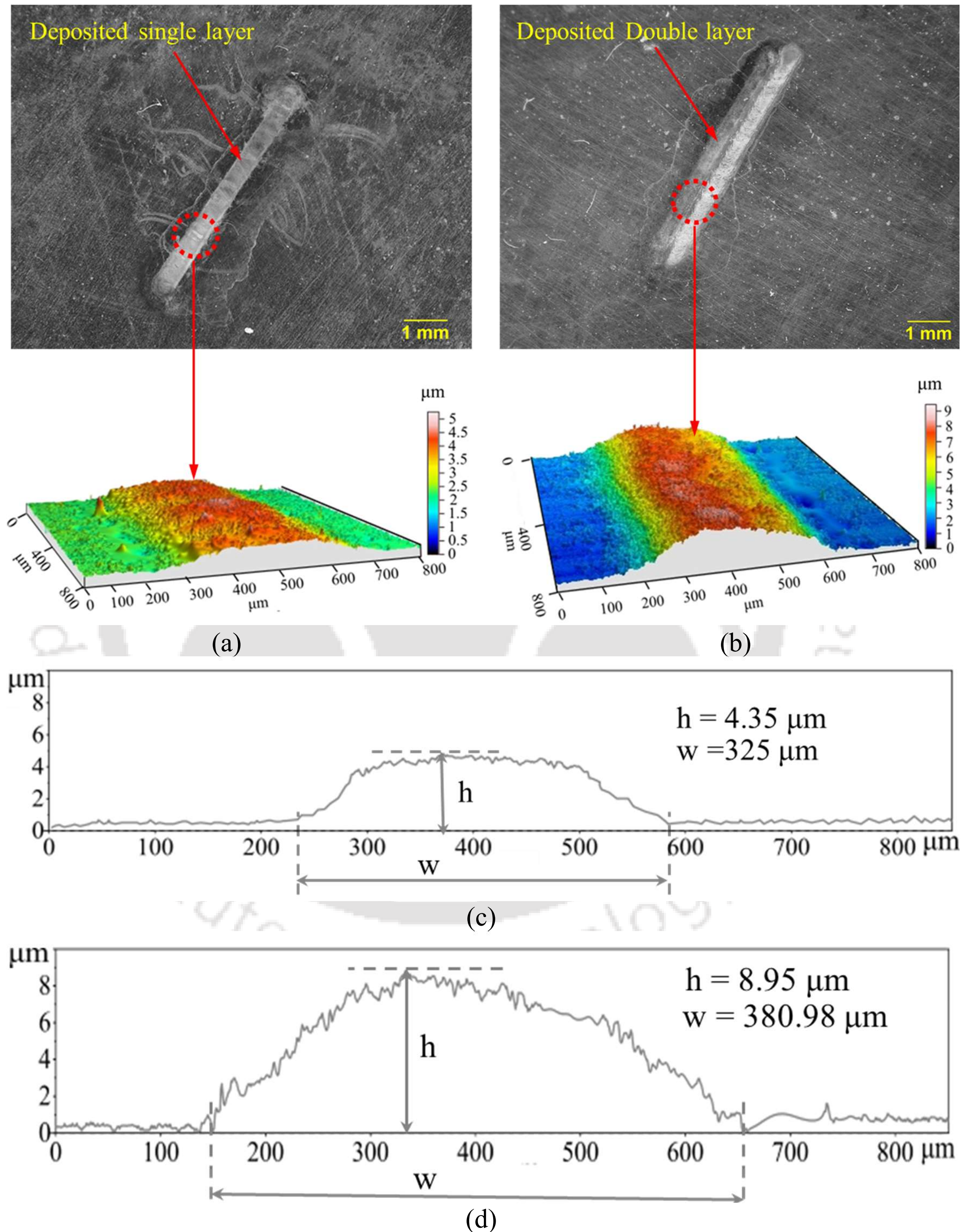

Fig. A2.8 Optical microscopy and 3D optical profilometer images of deposited (a) single and (b) double layers; Layer height measurement from 2D profilometer images of (c) single and (d) double layers

A percentage error of 5.43% for layer height and 4.95% for layer width between the predicted and experimental results is observed (Table A2.6), which is within the feasible range. This reflects the repeatability of the process.

As per the optimal experimental result, the layer height obtained for a single bead deposition is 4.35 μm (Fig. A2.8(c)). Hence, for the deposition of each layer, the tool is lifted accordingly to maintain the constant IEG. Fig. A2.8(b) shows the optical microscopy and 3D optical profilometer images of a deposited double layer. The measured layer height and width are 8.95 μm and 380.98 μm, respectively, as shown in the 2D profilometer image in Fig. A2.8(d).

Table A2.6 Validation of predicted results from DOE model with experiments

Experimental conditions		**Responses**				**% Error**	
		Predicted		**Experimental**			
Input variables	Values	Layer height (μm)	Layer width (μm)	Layer height (μm)	Layer width (μm)	Layer height	Layer width
Applied voltage (V)	3.57	4.60	341.93	4.35	325	5.43	4.95
Inter-electrode gap (μm)	5.38						
Frequency (kHz)	497						
Scanning speed (μm/s)	1.41						

At first, a computer-aided design (CAD) model of the component, to be deposited by LED process, is drawn in solid modeling software (Solidworks®). After that, uniform slicing of the CAD model is performed at different slicing heights. Further, the toolpath of the corresponding slices is generated with the help of a computer-aided manufacturing (CAM) package. A 3D circular ring of 4 mm diameter is deposited over a brass substrate by LED process with the optimized process parameters, as shown in Fig. A2.9. It demonstrates LED's capability of realizing complex shaped components.

TH-3378_196103004

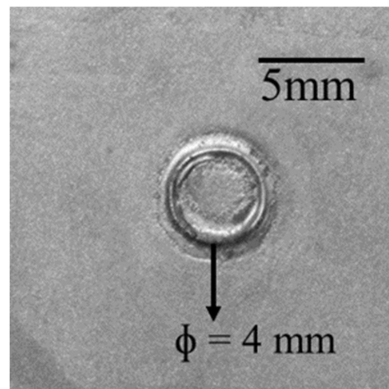

Fig. A2.9 A 3D circular ring deposited over a brass substrate at optimum process parameter condition

A2.3.5 Surface characterization of deposit

The surface characterization of the deposited 3D circular ring is carried out. Fig. A2.10(a) represents the field emission scanning electron microscopy (FESEM) image of the deposited surface where microscale pores are found at different locations. Micro-scale pores are formed due to the nucleation growth interrupted by the pulses. [104]

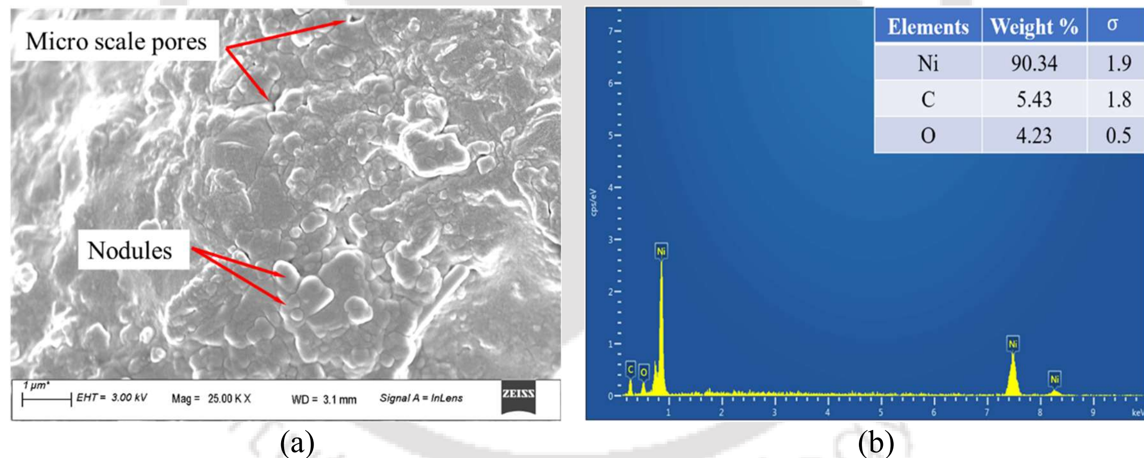

Elements	Weight %	σ
Ni	90.34	1.9
C	5.43	1.8
O	4.23	0.5

Fig. A2.10 Surface characterization of deposited 3D circular ring through (a) field emission scanning electron microscopy (FESEM) and (b) energy dispersive X-ray (EDX) analysis

The deposition is forced to start at many nucleation sites by the pulse current leading to the formation of nodules, and these nodules do not fuse completely.[140] The energy-dispersive X-ray analysis (EDX) image of the deposit is shown in Fig. A2.10(b). It shows the maximum percentage of Ni (90.34%) followed by carbon (5.43%) and oxygen (4.23%). The slight presence of carbon and oxygen in the deposited layer is due to their absorption from the atmosphere.

A2.3.6 Summary

The LED-based micro-additive manufacturing process is developed in the present work. Initial experimental investigations are carried out to maximize the output responses, viz., layer height and width. Regression models are obtained for output responses to study their effect at different applied voltage, current frequency, IEG, and scanning speeds. Further, repeatability and feasibility tests are being conducted. Because of vigorous bubble formation and the development of a depletion region, the deposition becomes nonuniform beyond a critical voltage (4V). The desirability approach is used to optimize the process parameter. The optimal values of the deposited maximum layer height and minimum layer width are 4.60 μm and 341.93 μm, respectively, at an optimal applied voltage of 3.57 V, IEG of 5.38 μm, frequency of 497 kHz, and scanning speed of 1.41 μm/s.

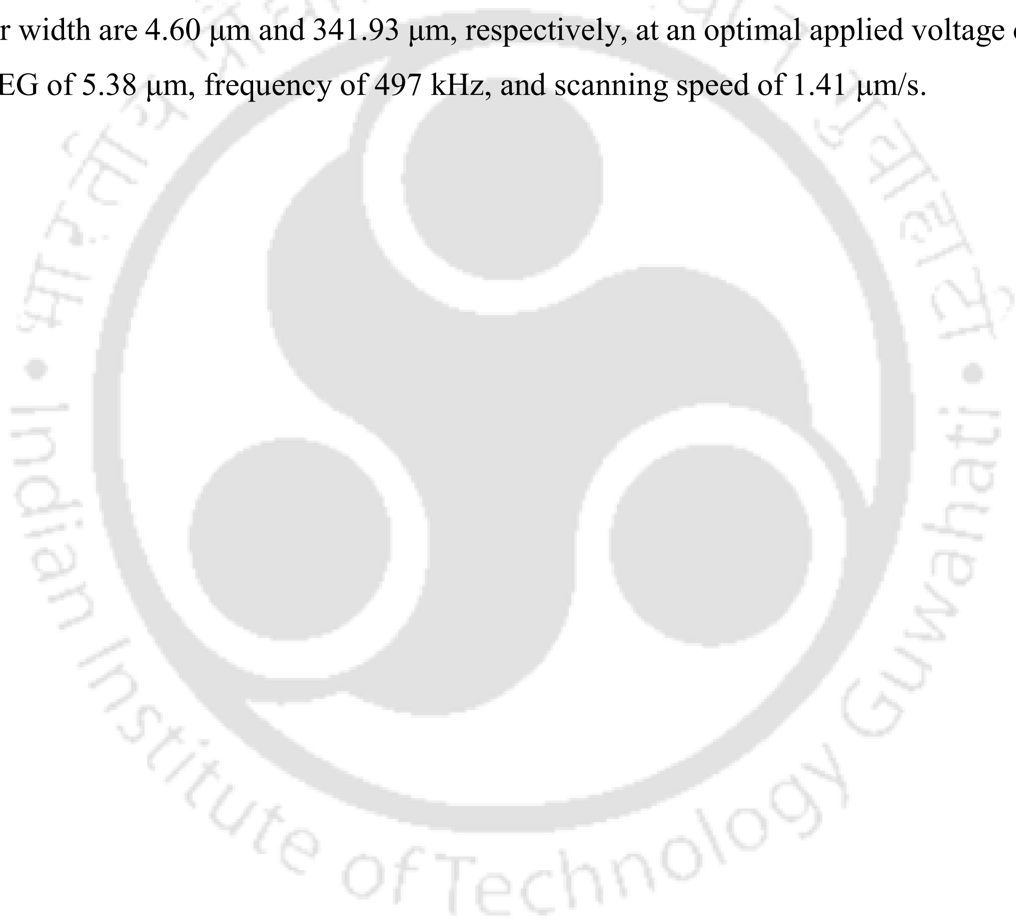

TH-3378_196103004

References

[1] M. J. Foust, D. Thomsen, R. Stickles, C. Cooper, and W. Dodds, “Development of the GE aviation low emissions TAPS combustor for next generation aircraft engines,” *50th AIAA Aerosp. Sci. Meet. Incl. New Horizons Forum Aerosp. Expo.*, p. 936, 2012, doi: 10.2514/6.2012-936.

[2] L. E. Murr *et al.*, “Next-generation biomedical implants using additive manufacturing of complex, cellular and functional mesh arrays,” *Philos. Trans. R. Soc. A Math. Phys. Eng. Sci.*, vol. 368, no. 1917, pp. 1999–2032, Apr. 2010, doi: 10.1098/RSTA.2010.0010.

[3] J. Madden, I. H.-J. of Microelectromechanical, and U. 1996, “Three-dimensional microfabrication by localized electrochemical deposition,” *ieeexplore.ieee.org*, vol. 5, pp. 24--32, 1996, Accessed: Sep. 24, 2021. [Online]. Available: https://ieeexplore.ieee.org/abstract/document/485212/

[4] R. Fratesi and G. Roventi, “Electrodeposition of zinc-nickel alloy coatings from a chloride bath containing NH4Cl,” *J. Appl. Electrochem.*, vol. 22, no. 7, pp. 657–662, Jul. 1992, doi: 10.1007/BF01092615/METRICS.

[5] “State of the Industry Reports - Wohlers Associates.” https://wohlersassociates.com/reports/ (accessed Feb. 16, 2024).

[6] T. Birtchnell and J. Urry, “A Brief History of 3D Printing,” *A New Ind. Futur.*, pp. 18–42, Oct. 2018, doi: 10.4324/9781315776798-2/BRIEF-HISTORY-3D-PRINTING-THOMAS-BIRTCHNELL-JOHN-URRY.

[7] E. Gentili, L. Tabaglio, and F. Aggogeri, “Review on micromachining techniques,” *CISM Int. Cent. Mech. Sci. Courses Lect.*, vol. 486, pp. 387–396, 2005, doi: 10.1007/3-211-38053-1_37/COVER.

[8] S. Mishra and V. Yadava, “Laser Beam MicroMachining (LBMM) – A review,” *Opt. Lasers Eng.*, vol. 73, pp. 89–122, Oct. 2015, doi: 10.1016/J.OPTLASENG.2015.03.017.

[9] H. E. Joe, E. G. Kang, and M. B. G. Jun, “A Review of State of the Art of Electron Beam and Ion Beam Machining,” *J. Korean Soc. Precis. Eng.*, vol. 35, no. 3, pp. 241–252, Mar. 2018, doi: 10.7736/KSPE.2018.35.3.241.

[10] P. Ghosh, D. Mondal, D. Dutta, and M. Mukhopadhyay, “A Review On Micromachining of Ti-6Al-4V Using Micro-EDM,” *Electro-Micromachining Microfabr.*, pp. 337–353, Jan. 2024, doi: 10.1201/9781003397793-15.

TH-3378_196103004

[11] Y. Zhu, G. Liu, Y. Li, and H. Tong, "Wear mechanism and preventive method of silicon electrodes in micro ECM," *Int. J. Adv. Manuf. Technol.*, pp. 1–13, Feb. 2024, doi: 10.1007/S00170-024-13166-X/FIGURES/19.

[12] M. Sreedhar *et al.*, "Electrochemical deposition of Cr3+ doped CuInSe2 thin films for electrocatalytic activity and photovoltaic performance," *Electrochim. Acta*, vol. 477, p. 143757, Feb. 2024, doi: 10.1016/J.ELECTACTA.2024.143757.

[13] A. L. Cohen, U. Frodis, F.-G. Tseng, G. Zhang, F. Mansfeld, and P. M. Will, "EFAB: low-cost automated electrochemical batch fabrication of arbitrary 3D microstructures," *https://doi.org/10.1117/12.361227*, vol. 3874, pp. 236–247, Aug. 1999, doi: 10.1117/12.361227.

[14] "Electrochemical fabrication methods incorporating dielectric materials and/or using dielectric substrates," Jan. 2005.

[15] A. Cohen, G. Zhang, F. G. Tseng, U. Frodis, F. Mansfeld, and P. Will, "EFAB: Rapid, low-cost desktop micromachining of high aspect ratio true 3-D MEMS," *Proc. IEEE Micro Electro Mech. Syst.*, pp. 244–251, 1999, doi: 10.1109/MEMSYS.1999.746824.

[16] A. Cohen, R. Chen, U. Frodis, M. T. Wu, and C. Folk, "Microscale metal additive manufacturing of multi-component medical devices," *Rapid Prototyp. J.*, vol. 16, no. 3, pp. 209–215, Jan. 2010, doi: 10.1108/13552541011034889.

[17] A. Jansson, G. Thornell, and S. Johansson, "High Resolution 3D Microstructures Made by Localized Electrodeposition of Nickel," *J. Electrochem. Soc.*, vol. 147, no. 5, p. 1810, May 2000, doi: 10.1149/1.1393439/XML.

[18] S. K. Seol, J. T. Kim, J. H. Je, Y. Hwu, and G. Margaritondo, "Three-dimensional (3D) polypyrrole microstructures with high aspect ratios fabricated by localized electropolymerization," *Macromolecules*, vol. 41, no. 9, pp. 3071–3074, May 2008, doi: 10.1021/MA702786G/ASSET/IMAGES/LARGE/MA-2007-02786G_0005.JPEG.

[19] E. M. Zimmerman and E. M. Zimmerman Y, "Method of jet plating," Jun. 1956.

[20] C. Wang, L. Shen, M. Qiu, Z. Tian, and W. Jiang, "Characterizations of Ni-CeO2 nanocomposite coating by interlaced jet electrodeposition," *J. Alloys Compd.*, vol. 727, pp. 269–277, Dec. 2017, doi: 10.1016/J.JALLCOM.2017.08.105.

[21] H. Fan, Y. P. Zhao, and S. K. Wang, "Technical Study of Jet Electrodeposition in Manufacture of Metal Parts," *Key Eng. Mater.*, vol. 667, pp. 259–264, 2016, doi: 10.4028/WWW.SCIENTIFIC.NET/KEM.667.259.

TH-3378_196103004

[22] R. A. Said, "Microfabrication by localized electrochemical deposition: Experimental investigation and theoretical modelling," *Nanotechnology*, vol. 14, no. 5, pp. 523–531, May 2003, doi: 10.1088/0957-4484/14/5/308.

[23] R. A. Said, "Shape Formation of Microstructures Fabricated by Localized Electrochemical Deposition," *J. Electrochem. Soc.*, vol. 150, no. 8, p. C549, 2003, doi: 10.1149/1.1591753/META.

[24] A. Brant, … M. S.-J. of, and U. 2015, "Finite element simulation of localized electrochemical deposition for maskless electrochemical additive manufacturing," *asmedigitalcollection.asme.orgAM Brant, MM Sundaram, AB KamarajJournal Manuf. Sci. Eng. 2015•asmedigitalcollection.asme.org*, vol. 137, p. 011018, 2015, Accessed: Jan. 06, 2024. [Online]. Available: https://asmedigitalcollection.asme.org/manufacturingscience/article-abstract/137/1/011018/375242

[25] A. B. Kamaraj and M. Sundaram, "A study on the effect of inter-electrode gap and pulse voltage on current density in electrochemical additive manufacturing," *J. Appl. Electrochem.*, vol. 48, no. 4, pp. 463–469, Apr. 2018, doi: 10.1007/S10800-018-1177-3.

[26] V. M. Volgin, T. B. Kabanova, and A. D. Davydov, "Modeling of local maskless electrochemical deposition of metal microcolumns," *Chem. Eng. Sci.*, vol. 183, pp. 123–135, Jun. 2018, doi: 10.1016/J.CES.2018.03.019.

[27] K. Nielsch, F. Mueller, A. Li, and U. Goesele, "ChemInform Abstract: Uniform Nickel Deposition into Ordered Alumina Pores by Pulsed Electrodeposition.," *ChemInform*, vol. 31, no. 27, Jul. 2000, doi: 10.1002/CHIN.200027243.

[28] C. Y. Lee, C. S. Lin, and B. R. Lin, "Localized electrochemical deposition process improvement by using different anodes and deposition directions," *J. Micromechanics Microengineering*, vol. 18, no. 10, Oct. 2008, doi: 10.1088/0960-1317/18/10/105008.

[29] F. Wang, H. Bian, and Y. Xiao, "Fabrication of Micro-Sized Copper Columns Using Localized Electrochemical Deposition with a 20 µm Diameter Micro Anode," *ECS J. Solid State Sci. Technol.*, vol. 8, no. 4, pp. P223–P227, 2019, doi: 10.1149/2.0111903JSS.

[30] S. Yeo, J. H. Choo, K. S. Yip, S. Yeo, J. H. Choo, and K. S. Yip, "Localized electrochemical deposition: the growth behavior of nickel microcolumns," *SPIE*, vol. 4174, pp. 30–39, Aug. 2000, doi: 10.1117/12.396421.

TH-3378_196103004

[31] R. A. Said, “Localized electro-deposition (LED): The march toward process development,” *Nanotechnology*, vol. 15, no. 10, Oct. 2004, doi: 10.1088/0957-4484/15/10/025.

[32] J. C. Lin, T. K. Chang, J. H. Yang, Y. S. Chen, and C. L. Chuang, “Localized electrochemical deposition of micrometer copper columns by pulse plating,” *Electrochim. Acta*, vol. 55, no. 6, pp. 1888–1894, Feb. 2010, doi: 10.1016/J.ELECTACTA.2009.11.002.

[33] S. K. Seol, A. R. Pyun, Y. Hwu, G. Margaritondo, and J. H. Je, “Localized electrochemical deposition of copper monitored using real-time X-ray microradiography,” *Adv. Funct. Mater.*, vol. 15, no. 6, pp. 934–937, Jun. 2005, doi: 10.1002/ADFM.200400514.

[34] Y.-J. Ciou, Y.-R. Hwang, J.-C. Lin, and Y.-T. Tseng, “Fabrication of 3D Microstructure by Localized Electrochemical Deposition with Image Feedback Distance Control and Five-Axis Motion Platform,” *ECS J. Solid State Sci. Technol.*, vol. 5, no. 7, pp. P425–P432, 2016, doi: 10.1149/2.0191607JSS.

[35] C. S. Lin, C. Y. Lee, J. H. Yang, and Y. S. Huang, “Improved copper microcolumn fabricated by localized electrochemical deposition,” *Electrochem. Solid-State Lett.*, vol. 8, no. 9, 2005, doi: 10.1149/1.1999911.

[36] J. C. Lin *et al.*, “Fabrication of micrometer Ni columns by continuous and intermittent microanode guided electroplating,” *J. Micromechanics Microengineering*, vol. 15, no. 12, pp. 2405–2413, Dec. 2005, doi: 10.1088/0960-1317/15/12/024.

[37] S. H. Yeo and J. H. Choo, “Effects of rotor electrode in the fabrication of high aspect ratio microstructures by localized electrochemical deposition,” *J. Micromechanics Microengineering*, vol. 11, no. 5, pp. 435–442, Sep. 2001, doi: 10.1088/0960-1317/11/5/301.

[38] S. H. Yeo, J. H. Choo, and K. H. A. Sim, “On the effects of ultrasonic vibrations on localized electrochemical deposition,” *J. Micromechanics Microengineering*, vol. 12, no. 3, pp. 271–279, May 2002, doi: 10.1088/0960-1317/12/3/312.

[39] Y. Wu *et al.*, “Study on application of laser in maskless localized electrodeposition and surface quality enhancement,” *Opt. Laser Technol.*, vol. 143, p. 107383, Nov. 2021, doi: 10.1016/J.OPTLASTEC.2021.107383.

[40] E. M. El-Giar, R. A. Said, G. E. Bridges, and D. J. Thomson, “Localized Electrochemical Deposition of Copper Microstructures,” *J. Electrochem. Soc.*, vol.

TH-3378_196103004

147, no. 2, p. 586, 2000, doi: 10.1149/1.1393237.

[41] Y. T. Tseng, J. C. Lin, Y. J. Ciou, and Y. R. Hwang, "Fabrication of a novel microsensor consisting of electrodeposited ZnO nanorod-coated crossed Cu micropillars and the effects of nanorod coating morphology on the gas sensing," *ACS Appl. Mater. Interfaces*, vol. 6, no. 14, pp. 11424–11438, Jul. 2014, doi: 10.1021/AM5019836.

[42] M. A. Habib, S. W. Gan, and M. Rahman, "Fabrication of complex shape electrodes by localized electrochemical deposition," *J. Mater. Process. Technol.*, vol. 209, no. 9, pp. 4453–4458, May 2009, doi: 10.1016/J.JMATPROTEC.2008.10.041.

[43] M. A. Habib and M. Rahman, "Performance of electrodes fabricated by localized electrochemical deposition (LECD) in micro-EDM operation on different workpiece materials," *J. Manuf. Process.*, vol. 24, pp. 78–89, Oct. 2016, doi: 10.1016/J.JMAPRO.2016.08.003.

[44] R. A. Said, "Adaptive tip-withdrawal control for reliable microfabrication by localized electrodeposition," *J. Microelectromechanical Syst.*, vol. 13, no. 5, pp. 822–832, Oct. 2004, doi: 10.1109/JMEMS.2004.835774.

[45] S. Daryadel *et al.*, "Localized Pulsed Electrodeposition Process for Three-Dimensional Printing of Nanotwinned Metallic Nanostructures," *Nano Lett.*, vol. 18, no. 1, pp. 208–214, Jan. 2018, doi: 10.1021/ACS.NANOLETT.7B03930/ASSET/IMAGES/LARGE/NL-2017-03930R_0005.JPEG.

[46] F. Wang, H. Xiao, and H. He, "Effects of applied potential and the initial gap between electrodes on localized electrochemical deposition of micrometer copper columns OPEN," *Sci. Rep.*, vol. 6, no. 26270, 2016, doi: 10.1038/srep26270.

[47] M. Sundaram, A. Drexelius, and A. B. Kamaraj, "Machining Science and Technology An International Journal A study on the effect of interelectrode gap in the electrochemical additive manufacturing process," *Mach. Sci. Technol.*, vol. 23, pp. 232--248, 2019, doi: 10.1080/10910344.2018.1486419.

[48] A. B. Kamaraj and M. Sundaram, "A mathematical model of the deposition rate and layer height during electrochemical additive manufacturing," *Int. J. Adv. Manuf. Technol.*, vol. 102, pp. 2367--2374, 2019, doi: 10.1007/s00170-019-03292-2.

[49] K. C. Chan, W. K. Chan, and N. S. Qu, "Effect of current waveform on the deposit quality of electroformed nickels," *J. Mater. Process. Technol.*, vol. 89–90, pp. 447–450, May 1999, doi: 10.1016/S0924-0136(99)00053-9.

TH-3378_196103004

[50] N. Manukyan, A. Kamaraj, and M. Sundaram, “Localized Electrochemical Deposition Using Ultra-High Frequency Pulsed Power,” *Procedia Manuf.*, vol. 34, pp. 197–204, Jan. 2019, doi: 10.1016/J.PROMFG.2019.06.139.

[51] D. T. Chin and K. L. Hsueh, “MASS TRANSFER TO A CYLINDRICAL SURFACE FROM AN UNSUBMERGED IMPINGING JET.,” *Electrochem. Soc. Ext. Abstr.*, vol. 85–1, no. 1, p. 730, Jan. 1985, doi: 10.1149/1.2108549/XML.

[52] M. Chen, R. Chalupa, A. C. West, and V. Modi, “High Schmidt mass transfer in a laminar impinging slot jet flow,” *Int. J. Heat Mass Transf.*, vol. 43, no. 21, pp. 3907–3915, Nov. 2000, doi: 10.1016/S0017-9310(00)00052-1.

[53] M. S. Rajput, P. M. Pandey, and S. Jha, “Modelling of high speed selective jet electrodeposition process,” *J. Manuf. Process.*, vol. 17, pp. 98–107, Jan. 2015, doi: 10.1016/J.JMAPRO.2014.07.012.

[54] T. J. Chen and R. C. Alkire, “HIGH-SPEED SELECTIVE ELECTROPLATING WITH SINGLE CIRCULAR JETS.,” *Proc. - Electrochem. Soc.*, vol. 83–12, no. 11, pp. 55–65, Nov. 1983, doi: 10.1149/1.2123560/XML.

[55] C. Karakus and D. -T. Chin, “Metal Distribution in Jet Plating,” *J. Electrochem. Soc.*, vol. 141, no. 3, pp. 691–697, Mar. 1994, doi: 10.1149/1.2054793/XML.

[56] M. Kunieda, R. Katoh, and Y. Mori, “Rapid Prototyping by Selective Electrodeposition Using Electrolyte Jet,” *CIRP Ann.*, vol. 47, no. 1, pp. 161–164, Jan. 1998, doi: 10.1016/S0007-8506(07)62808-X.

[57] G. Qiao *et al.*, “High-speed jet electrodeposition and microstructure of nanocrystalline Ni–Co alloys,” *Electrochim. Acta*, vol. 51, no. 1, pp. 85–92, Oct. 2005, doi: 10.1016/J.ELECTACTA.2005.03.050.

[58] M. S. Rajput, P. M. Pandey, and S. Jha, “Experimental investigations into ultrasonic-assisted jet electrodeposition process,” *J Eng. Manuf.*, vol. 228, no. 5, pp. 682–694, 2014, doi: 10.1177/0954405413506198.

[59] J. C. Lin, T. K. Chang, J. H. Yang, J. H. Jeng, D. L. Lee, and S. B. Jiang, “Fabrication of a micrometer Ni–Cu alloy column coupled with a Cu micro-column for thermal measurement,” *J. Micromechanics Microengineering*, vol. 19, no. 1, p. 015030, Dec. 2008, doi: 10.1088/0960-1317/19/1/015030.

[60] H. Fan, Y. Zhao, S. Wang, and H. Guo, “Effect of jet electrodeposition conditions on microstructure and mechanical properties of Cu–Al2O3 composite coatings,” *Int. J. Adv. Manuf. Technol.*, vol. 105, no. 11, pp. 4509–4516, Dec. 2019, doi: 10.1007/S00170-019-03419-5/METRICS.

TH-3378_196103004

[61] Y. Wang, F. Yi, T. Zhang, J. Liu, B. Wang, and Y. Zhou, "Design and property study of micro-slot optics," *Opt. Commun.*, vol. 386, pp. 14–21, Mar. 2017, doi: 10.1016/J.OPTCOM.2016.11.020.

[62] R. J. Von Gutfeld, M. H. Gelchinski, L. T. Romankiw, and D. R. Vigliotti, "Laser-enhanced jet plating: A method of high-speed maskless patterning," *Appl. Phys. Lett.*, vol. 43, no. 9, pp. 876–878, Nov. 1983, doi: 10.1063/1.94534.

[63] G. F. Wang, Z. J. Tian, Z. D. Liu, L. Da Shen, and J. Zhu, "Preparation of Nickel Parts by Jet Electro-Deposition Technique Based on Templates and Grinding," *Int. J. Electrochem. Sci.*, vol. 10, no. 8, pp. 6844–6854, Aug. 2015, doi: 10.1016/S1452-3981(23)06766-4.

[64] L. Xinchao *et al.*, "Compressed Air-Film Encircling Jet Electrodeposition with High Deposition Accuracy," *J. Electrochem. Soc.*, vol. 167, no. 10, p. 102502, Jun. 2020, doi: 10.1149/1945-7111/AB971D.

[65] J. B. Nelson and D. T. Schwartz, "Characterization of Buffered Electrolytes for Nickel Electrochemical Printing," *J. Electrochem. Soc.*, vol. 155, no. 3, p. D181, Jan. 2008, doi: 10.1149/1.2825166/XML.

[66] W. Wei *et al.*, "Additive manufacturing of three-dimensional intricate microfeatures by electrolyte-column localized electrochemical deposition," *Addit. Manuf.*, vol. 50, Feb. 2022, doi: 10.1016/J.ADDMA.2021.102582.

[67] H. Kim, J. G. Kim, J. W. Park, and C. N. Chu, "Selective copper metallization of nonconductive materials using jet-circulating electrodeposition," *Precis. Eng.*, vol. 51, pp. 153–159, Jan. 2018, doi: 10.1016/J.PRECISIONENG.2017.08.005.

[68] Z. J. Tian, D. S. Wang, G. F. Wang, L. Da Shen, Z. D. Liu, and Y. H. Huang, "Microstructure and properties of nanocrystalline nickel coatings prepared by pulse jet electrodeposition," *Trans. Nonferrous Met. Soc. China*, vol. 20, no. 6, pp. 1037–1042, Jun. 2010, doi: 10.1016/S1003-6326(09)60254-5.

[69] X. Liu, L. Shen, M. Qiu, Z. Tian, Y. Wang, and K. Zhao, "Jet electrodeposition of nanocrystalline nickel assisted by controllable friction," *Surf. Coatings Technol.*, vol. 305, pp. 231–240, Nov. 2016, doi: 10.1016/J.SURFCOAT.2016.08.043.

[70] C. Sun, H. Fan, J. Jiang, Z. Li, and Y. Zhao, "Effect of Current Density on Microstructure, Microhardness, and Tribological Properties of Cu-Al2O3 Composite Coatings Prepared by Jet Electrodeposition," *J. Electron. Mater.*, vol. 51, no. 11, pp. 6518–6524, Nov. 2022, doi: 10.1007/S11664-022-09892-1/FIGURES/7.

[71] H. Fan, Z. Li, Y. Zhao, S. Wang, and S. Cao, "The Effects of Pulsed Current

TH-3378_196103004

Parameters on Porosity of Copper Prepared by Jet Electrodeposition," *Int. J. Electrochem. Sci*, vol. 14, pp. 3326–3335, 2019, doi: 10.20964/2019.04.48.

[72] M. S. Rajput, P. M. Pandey, and S. Jha, "Micromanufacturing by selective jet electrodeposition process," *Int. J. Adv. Manuf. Technol. 2013 761*, vol. 76, no. 1, pp. 61–67, Nov. 2013, doi: 10.1007/S00170-013-5470-3.

[73] V. K. Deshmukh, M. S. Rajput, and H. K. Narang, "A systematic review on high speed selective jet electrodeposition manufacturing," *World J. Eng.*, vol. ahead-of-print, no. ahead-of-print, 2022, doi: 10.1108/WJE-04-2022-0179/FULL/PDF.

[74] S. Pané *et al.*, "The effect of saccharine on the localized electrochemical deposition of Cu-rich Cu–Ni microcolumns," *Electrochem. commun.*, vol. 13, no. 9, pp. 973–976, Sep. 2011, doi: 10.1016/J.ELECOM.2011.06.015.

[75] L. Yong, Z. Yunfei, Y. Guang, and P. Liangqiang, "Localized electrochemical micromachining with gap control," *Sensors Actuators A*, vol. 108, pp. 144–148, 2003, doi: 10.1016/S0924-4247(03)00371-6.

[76] G. Thornell, A. Jansson, and S. A. I. Johansson, "Direct writing of nickel by electrodeposition from various electrolytes," *Smart Mater. Nano-, Micro- Smart Syst.*, vol. 3892, pp. 166–175, Oct. 1999, doi: 10.1117/12.364480.

[77] T. K. Chang, J. C. Lin, J. H. Yang, P. C. Yeh, D. L. Lee, and S. B. Jiang, "Surface and transverse morphology of micrometer nickel columns fabricated by localized electrochemical deposition," *J. Micromechanics Microengineering*, vol. 17, no. 11, pp. 2336–2343, Nov. 2007, doi: 10.1088/0960-1317/17/11/022.

[78] J. B. Nelson, Z. Wisecarver, and D. T. Schwartz, "Electrochemical printing: mass transfer effects," *J. Micromechanics Microengineering*, vol. 17, no. 6, p. 1192, May 2007, doi: 10.1088/0960-1317/17/6/013.

[79] M. M. Sundaram, A. B. Kamaraj, and V. S. Kumar, "Mask-less electrochemical additive manufacturing: A feasibility study," *J. Manuf. Sci. Eng. Trans. ASME*, vol. 137, no. 2, Apr. 2015, doi: 10.1115/1.4029022/377491.

[80] M. Sundaram, A. B. Kamaraj, and G. Lillie, "Experimental Study of Localized Electrochemical Deposition of Ni-Cu Alloy Using a Moving Anode," *Procedia CIRP*, vol. 68, pp. 227–231, 2018, doi: 10.1016/J.PROCIR.2017.12.053.

[81] X. Chen, X. Liu, P. Childs, N. Brandon, and B. Wu, "A Low Cost Desktop Electrochemical Metal 3D Printer," *Adv. Mater. Technol.*, vol. 2, no. 10, p. 1700148, Oct. 2017, doi: 10.1002/ADMT.201700148.

[82] F. F. Wang *et al.*, "Nanofabrication of the gold scanning probe for the STM-SECM

TH-3378_196103004

coupling system with nanoscale spatial resolution," *Sci. China Chem.*, vol. 60, no. 5, pp. 649–655, May 2017, doi: 10.1007/S11426-017-9029-9/METRICS.

[83] J. Hu and M. F. Yu, "Meniscus-confined three-dimensional electrodeposition for direct writing of wire bonds," *Science (80-.).*, vol. 329, no. 5989, pp. 313–316, Jul. 2010, doi: 10.1126/SCIENCE.1190496/SUPPL_FILE/HU.SOM.PDF.

[84] T. K. Chang *et al.*, "Surface and transverse morphology of micrometer nickel columns fabricated by localized electrochemical deposition," *JMiMi*, vol. 17, no. 11, pp. 2336–2343, Nov. 2007, doi: 10.1088/0960-1317/17/11/022.

[85] J. C. Lin, T. K. Chang, J. H. Yang, J. H. Jeng, D. L. Lee, and S. B. Jiang, "Fabrication of a micrometer Ni–Cu alloy column coupled with a Cu micro-column for thermal measurement," *J. Micromechanics Microengineering*, vol. 19, no. 1, p. 015030, Dec. 2008, doi: 10.1088/0960-1317/19/1/015030.

[86] S. K. Seol, J. T. Kim, J. H. Je, Y. Hwu, and G. Margaritondo, "Fabrication of freestanding metallic micro hollow tubes by template-free localized electrochemical deposition," *Electrochem. Solid-State Lett.*, vol. 10, no. 5, pp. 44–46, 2007, doi: 10.1149/1.2713660.

[87] H. Kim, N. P. Subramanian, and B. N. Popov, "Preparation of PEM fuel cell electrodes using pulse electrodeposition," *J. Power Sources*, vol. 138, no. 1–2, pp. 14–24, Nov. 2004, doi: 10.1016/J.JPOWSOUR.2004.06.012.

[88] A. E. Bolzán, "Electrodeposition of copper on glassy carbon electrodes in the presence of picolinic acid," *Electrochim. Acta*, vol. 113, pp. 706–718, Dec. 2013, doi: 10.1016/J.ELECTACTA.2013.09.132.

[89] A. Kamaraj, S. Lewis, and M. Sundaram, "Numerical Study of Localized Electrochemical Deposition for Micro Electrochemical Additive Manufacturing," *Procedia CIRP*, vol. 42, pp. 788–792, Jan. 2016, doi: 10.1016/J.PROCIR.2016.02.320.

[90] X. Fu, J. Li, H. Zhang, and J. Xian, "Simulation and experimental research on nickel-based coating prepared by jet electrodeposition at different scanning speeds," *Int. J. Adv. Manuf. Technol.*, vol. 1, p. 3, 2022, doi: 10.1007/s00170-022-09308-8.

[91] M. Pole, M. Sadeghilaridjani, J. Shittu, C. Mahajan, N. Ghodki, and S. Mukherjee, "Electrodeposited metallic glasses with superlative wear resistance," *Mater. Sci. Eng. A*, vol. 816, p. 141315, Jun. 2021, doi: 10.1016/J.MSEA.2021.141315.

[92] L. Xinchao *et al.*, "Compressed Air-Film Encircling Jet Electrodeposition with High Deposition Accuracy," *J. Electrochem. Soc.*, vol. 167, no. 10, p. 102502, Jun. 2020,

TH-3378_196103004

doi: 10.1149/1945-7111/AB971D.

[93] C. Kasper, “The Theory of the Potential and the Technical Practice of Electrodeposition III . Linear Polarization on Some Line-Plane Systems,” *Trans. Electrochem. Soc.*, vol. 78, no. 1, p. 131, 1940, doi: 10.1149/1.3071296.

[94] C. W. Tobias and R. Wijsman, “Theory of the Effect of Electrode Resistance on Current Density Distribution in Electrolytic Cells,” *J. Electrochem. Soc.*, vol. 100, no. 10, p. 459, Oct. 1953, doi: 10.1149/1.2780879/XML.

[95] V. M. Volgin, V. V. Lyubimov, I. V. Gnidina, T. B. Kabanova, and A. D. Davydov, “Effect of Anode Shape on Uniformity of Electrodeposition onto Resistive Substrates,” *Electrochim. Acta*, vol. 230, pp. 382–390, Mar. 2017, doi: 10.1016/J.ELECTACTA.2017.02.015.

[96] “Crystal Quality and Photoelectrochemical Response of Bismuth Containing Cu2ZnSnS4 (CZTS) Absorber Layers for Photovoltaic Applications,” *ECS Meet. Abstr.*, pp. 2102--2102, 2018, doi: 10.1149/MA2018-01/36/2102.

[97] V. K. Deshmukh, A. Namdev, H. K. Narang, M. S. Rajput, and P. M. Pandey, “Instantaneous fabrication of thin MEMS features by copper electrodeposition using modified inkjet printer,” *J. Nano- Electron. Phys.*, vol. 12, no. 2, 2020, doi: 10.21272/JNEP.12(2).02044.

[98] M. F. Alebrahim, I. A. Khattab, and A. O. Sharif, “Electrodeposition of copper from a copper sulfate solution using a packed-bed continuous-recirculation flow reactor at high applied electric current,” *Egypt. J. Pet.*, vol. 24, no. 3, pp. 325–331, Sep. 2015, doi: 10.1016/J.EJPE.2015.07.009.

[99] M. H. Gelchinski, L. T. Romankiw, D. R. Vigliotti, and R. J. von Gutfeld, “Electrochemical and Metallurgical Aspects of Laser-Enhanced Jet Plating of Gold,” *J. Electrochem. Soc.*, vol. 132, no. 11, pp. 2575–2581, Nov. 1985, doi: 10.1149/1.2113627/META.

[100] M. S. Rajput, P. M. Pandey, and S. Jha, “Micromanufacturing by selective jet electrodeposition process,” *Int. J. Adv. Manuf. Technol.*, vol. 76, no. 1–4, pp. 61–67, Jan. 2015, doi: 10.1007/S00170-013-5470-3/METRICS.

[101] H. Babaei, M. Khosravi, M. R. Sovizi, and S. A. Khorramie, “Investigating the Au-Cu thick layers Electrodeposition Rate with Pulsed Current by Optimization of the Operation Condition,” *J. Electrochem. Sci. Technol.*, vol. 11, no. 2, pp. 172–179, 2020, doi: 10.33961/JECST.2019.00087.

[102] A. Baral, C. K. Sarangi, B. C. Tripathy, I. N. Bhattacharya, and T. Subbaiah,

TH-3378_196103004

“Copper electrodeposition from sulfate solutions—Effects of selenium,” *Hydrometallurgy*, vol. 146, pp. 8–14, May 2014, doi: 10.1016/J.HYDROMET.2014.03.001.

[103] L. Shen, C. Wang, Z. Tian, W. Jiang, W. Zhuo, and K. Zhao, “Study on the properties of jet electrodeposited nickel coating by rotating interlacing method,” *Int. J. Electrochem. Sci.*, vol. 13, no. 2, pp. 1831–1843, 2018, doi: 10.20964/2018.02.12.

[104] A. B. Kamaraj, H. Shrestha, E. Speck, and M. Sundaram, “Experimental Study on the Porosity of Electrochemical Nickel Deposits,” *Procedia Manuf.*, vol. 10, pp. 478–485, Jan. 2017, doi: 10.1016/J.PROMFG.2017.07.032.

[105] C. Léger, L. Servant, J. L. Bruneel, and F. Argoul, “Growth patterns in electrodeposition,” *Phys. A Stat. Mech. its Appl.*, vol. 263, no. 1–4, pp. 305–314, Feb. 1999, doi: 10.1016/S0378-4371(98)00484-1.

[106] N. A. Ogolo, O. G. Akinboro, J. E. Inam, F. E. Akpokere, and M. O. Onyekonwu, “Effect of grain size on porosity revisited,” *Soc. Pet. Eng. - SPE Niger. Annu. Int. Conf. Exhib. NAICE 2015*, 2015, doi: 10.2118/178296-MS.

[107] L. Jinlong, L. Tongxiang, and W. Chen, “Effect of electrodeposition temperature on grain orientation and corrosion resistance of nanocrystalline pure nickel,” *J. Solid State Chem.*, vol. 240, pp. 109–114, Aug. 2016, doi: 10.1016/J.JSSC.2016.05.025.

[108] R. Sen, S. Bhattacharya, S. Das, and K. Das, “Effect of surfactant on the co-electrodeposition of the nano-sized ceria particle in the nickel matrix,” *J. Alloys Compd.*, vol. 489, no. 2, pp. 650–658, Jan. 2010, doi: 10.1016/J.JALLCOM.2009.09.142.

[109] A. M. Pandey, S. Kapil, and M. Das, “Experimental investigation of localized electrochemical deposition-based micro-additive manufacturing process,” *Mater. Manuf. Process.*, 2023, doi: 10.1080/10426914.2023.2190383.

[110] V. Vitry, A. Sens, and F. Delaunois, “Comparison of various electroless nickel coatings on steel: Structure, hardness and abrasion resistance,” *Mater. Sci. Forum*, vol. 783–786, pp. 1405–1413, 2014, doi: 10.4028/WWW.SCIENTIFIC.NET/MSF.783-786.1405.

[111] X. Zheng, J. Tan, Q. Zhang, M. Wang, and L. Meng, “Effect of laser surface texturing depth on the adhesion of electroless plated nickel coating on alumina,” *Surf. Coatings Technol.*, vol. 311, pp. 151--156, 2017, doi: 10.1016/j.surfcoat.2017.01.002.

[112] Y. Cao, S. Zhu, X. Liang, and W. Wang, “Overlapping model of beads and curve

TH-3378_196103004

fitting of bead section for rapid manufacturing by robotic MAG welding process," *Robot. Comput. Integr. Manuf.*, vol. 27, no. 3, pp. 641–645, Jun. 2011, doi: 10.1016/j.rcim.2010.11.002.

[113] S. Suryakumar, K. P. Karunakaran, A. Bernard, U. Chandrasekhar, N. Raghavender, and D. Sharma, "Weld bead modeling and process optimization in Hybrid Layered Manufacturing," *Comput. Des.*, vol. 43, no. 4, pp. 331–344, Apr. 2011, doi: 10.1016/J.CAD.2011.01.006.

[114] S. Singh, A. Singh, S. Kapil, and M. Das, "Utilization of a TSP solver for generating non-retractable, direction favouring toolpath for additive manufacturing," *Addit. Manuf.*, vol. 59, p. 103126, Nov. 2022, doi: 10.1016/j.addma.2022.103126.

[115] H. Fan, Y. Zhao, J. Jiang, S. Wang, W. Shan, and Z. Li, "Effect of the Pulse Duty Cycle on the Microstructure and Properties of a Jet Electrodeposited Nanocrystalline Copper Coating," *Mater. Trans.*, vol. 61, pp. 795--800, 2020, doi: 10.2320/matertrans.MT-M2019364.

[116] L. A. Azpeitia, C. A. Gervasi, and A. E. Bolzán, "Electrochemical aspects of tin electrodeposition on copper in acid solutions," *Electrochim. Acta*, vol. 298, pp. 400–412, Mar. 2019, doi: 10.1016/J.ELECTACTA.2018.12.040.

[117] A. Mani and K. M. Wang, "Electroconvection Near Electrochemical Interfaces: Experiments, Modeling, and Computation," *https://doi.org/10.1146/annurev-fluid-010719-060358*, vol. 52, pp. 509–529, Jan. 2020, doi: 10.1146/ANNUREV-FLUID-010719-060358.

[118] K. Isobe, T. Fukunaga, W. Takashima, and K. Kaneto, "Selective electrodeposition of conducting polymers," *Synth. Met.*, vol. 85, no. 1–3, pp. 1435–1436, Mar. 1997, doi: 10.1016/S0379-6779(97)80307-4.

[119] R. Alkire and J. Ju, "High Speed Selective Electroplating with Impinging Two-Dimensional Slot Jet Flow," *J. Electrochem. Soc.*, vol. 134, no. 2, pp. 294–299, Feb. 1987, doi: 10.1149/1.2100449/XML.

[120] M. Georgiadou and D. Veyret, "Optimization of trench filling during copper electrodeposition by additives and pulse plating," *http://dx.doi.org/10.1243/09544050360673233*, vol. 217, no. 6, pp. 857–863, Jun. 2003, doi: 10.1243/09544050360673233.

[121] B. Unveroglu and G. Zangari, "Crystal Quality and Photoelectrochemical Response of Bismuth Containing Cu2ZnSnS4 (CZTS) Absorber Layers for Photovoltaic Applications," *ECS Meet. Abstr.*, vol. MA2018-01, no. 36, p. 2102, Apr. 2018, doi:

TH-3378_196103004

10.1149/MA2018-01/36/2102.

[122] X. Li, P. Ming, S. Ao, and W. Wang, "Review of additive electrochemical micro-manufacturing technology," *Int. J. Mach. Tools Manuf.*, vol. 173, p. 103848, Feb. 2022, doi: 10.1016/J.IJMACHTOOLS.2021.103848.

[123] R. R. Reddy, Y. Okamoto, and Y. Mita, "An On-Chip Micromachined Test Structure to Study the Tribological Behavior of Deep-RIE MEMS Sidewall Surfaces," *IEEE Trans. Semicond. Manuf.*, vol. 33, no. 2, pp. 187–195, May 2020, doi: 10.1109/TSM.2020.2982659.

[124] M. Tyagi, G. M. Spinks, and E. W. H. Jager, "Fully 3D printed soft microactuators for soft microrobotics," *Smart Mater. Struct.*, vol. 29, no. 8, p. 085032, Jul. 2020, doi: 10.1088/1361-665X/AB9F48.

[125] C. Y. Yap *et al.*, "Review of selective laser melting: Materials and applications," *Appl. Phys. Rev.*, vol. 2, no. 4, p. 041101, Dec. 2015, doi: 10.1063/1.4935926.

[126] A. M. Engwall, Z. Rao, and E. Chason, "Residual Stress in Electrodeposited Cu Thin Films: Understanding the Combined Effects of Growth Rate and Grain Size," *J. Electrochem. Soc.*, vol. 164, no. 13, pp. D828–D834, Oct. 2017, doi: 10.1149/2.0921713JES/XML.

[127] L. M. Jiang *et al.*, "A modified layer-removal method for residual stress measurement in electrodeposited nickel films," *Thin Solid Films*, vol. 519, no. 10, pp. 3249–3253, Mar. 2011, doi: 10.1016/J.TSF.2011.01.260.

[128] X. Yuqing, W. Menghua, and J. Weiping, "Effect of process parameters on growth pattern of micro-nickel column in mask-less localized electrodeposition," *Procedia CIRP*, vol. 113, pp. 552–557, Jan. 2022, doi: 10.1016/J.PROCIR.2022.09.173.

[129] E. M. Giar, R. A. Said, G. E. Bridges, and D. J. Thomson, "Localized Electrochemical Deposition of Copper Microstructures," *J. Electrochem. Soc.*, vol. 147, no. 2, p. 586, Feb. 2000, doi: 10.1149/1.1393237.

[130] N. Qian, M. Wu, S. Zuo, and J. Wu, "Research on technology of additive manufacturing 3D metallic microstructure by maskless localized electrodepositing method," *Procedia CIRP*, vol. 95, pp. 815–820, 2020, doi: 10.1016/J.PROCIR.2020.02.300.

[131] S. Morsali, S. Daryadel, Z. Zhou, A. Behroozfar, D. Qian, and M. Minary-Jolandan, "Multi-physics simulation of metal printing at micro/nanoscale using meniscus-confined electrodeposition: Effect of environmental humidity," *J. Appl. Phys.*, vol. 121, no. 2, p. 024903, Jan. 2017, doi: 10.1063/1.4973622.

TH-3378_196103004

[132] M. Aarts, A. Reiser, R. Spolenak, and E. Alarcon-Llado, "Confined pulsed diffuse layer charging for nanoscale electrodeposition with an STM," *Nanoscale Adv.*, vol. 4, no. 4, pp. 1182–1190, Feb. 2022, doi: 10.1039/D1NA00779C.

[133] E. García-Lecina, I. García-Urrutia, J. A. Díez, J. Morgiel, and P. Indyka, "A comparative study of the effect of mechanical and ultrasound agitation on the properties of electrodeposited Ni/Al2O3 nanocomposite coatings," *Surf. Coatings Technol.*, vol. 206, no. 11–12, pp. 2998–3005, Feb. 2012, doi: 10.1016/J.SURFCOAT.2011.12.037.

[134] F. Wang, F. Wang, and H. He, "Parametric Electrochemical Deposition of Controllable Morphology of Copper Micro-Columns," *J. Electrochem. Soc.*, vol. 163, no. 10, pp. E322–E327, Sep. 2016, doi: 10.1149/2.1191610JES/XML.

[135] M. Zhang and X. Lian, "Rapid Fabrication of High-Aspect-Ratio Platinum Microprobes by Electrochemical Discharge Etching," 2016, doi: 10.3390/ma9040233.

[136] W. E. Org, M. A. El Sayed, M. M. El-Hendawy, and M. A. M. Ibrahim, "Article Number: 22044," *Int. J. Electrochem. Sci*, vol. 17, 2022, doi: 10.20964/2022.04.12.

[137] S. Jiang, Z. Guo, Y. Deng, H. Dong, X. Li, and J. Liu, "Effect of pulse frequency on the one-step preparation of superhydrophobic surface by pulse electrodeposition," *Appl. Surf. Sci.*, vol. 458, pp. 603–611, Nov. 2018, doi: 10.1016/J.APSUSC.2018.07.120.

[138] F. A. Shamim, A. Dvivedi, and P. Kumar, "On near-dry wire ECDM of Al6063/SiC/10p MMC," *https://doi.org/10.1080/10426914.2020.1802044*, vol. 36, no. 1, pp. 122–134, 2020, doi: 10.1080/10426914.2020.1802044.

[139] T. Tiwari, A. Dvivedi, and P. Kumar, "Investigations on the fabrication of a patterned tool by chemical etching," *Mater. Manuf. Process.*, vol. 36, no. 16, pp. 1840–1852, 2021, doi: 10.1080/10426914.2021.1926491.

[140] A. B. Kamaraj and M. Sundaram, "A mathematical model to predict the porosity of nickel pillars manufactured by localized electrochemical deposition under pulsed voltage conditions," *Procedia Manuf.*, vol. 48, pp. 181–186, 2020, doi: 10.1016/j.promfg.2020.05.036.

TH-3378_196103004

List of Publications

Journals

1. **A.M. Pandey**, S. Kapil, M. Das, Experimental investigation of localized electrochemical deposition-based micro-additive manufacturing process, Mater. Manuf. Process. (2023). https://doi.org/10.1080/10426914.2023.2190383.
2. **Anand Mohan Pandey**, Ambrish Singh, Sajan Kapil, and Manas Das "An efficient toolpath planning of realizing 3D micro metallic features via selective jet electrodeposition (SJED) process" Progress in additive manufacturing (**under review**)
3. **Pandey, A.M.**, Kapil, S. and Das, M. (2024), "A novel method of effectively fabricating the micro-objects by selective jet electrodeposition (SJED)", Rapid Prototyping Journal, Vol. ahead-of-print No. ahead-of-print. https://doi.org/10.1108/RPJ-10-2023-0352
4. **Anand Mohan Pandey**, Sajan Kapil, and Manas Das "A novel approach of thick coating through the Selective Jet Electrodeposition (SJED) process" Surface engineering **(Accepted)**

Conferences

1. **A. Mohan Pandey**, S. Kapil, M. Das, Numerical and experimental analysis of the localized electrodeposition (LED) based micro additive manufacturing process, Mater. Today Proc. (2023). https://doi.org/10.1016/J.MATPR.2023.10.063.
2. **Anand Mohan Pandey**, Sajan kapil, and Manas Das "Metal Based μ-Additive Manufacturing by Localized Electrochemical deposition" International Conference on Precision, Meso, Micro & Nano Engineering (COPEN-12), IIT Kanpur, Uttar Pradesh, India, 8th -10th Dec, 2022.
3. **Anand Mohan Pandey**, Sajan kapil and Manas Das "Metal Based μ-Additive Manufacturing by Localized Electrochemical deposition "NERC 2022 May 20-22, 2022, IIT Guwahati.
4. **Anand Mohan Pandey**, Sajan Kapil, and Manas Das "Micro deposition with localized electrodeposition" Research and industrial conclave-Integration 2023, 14-16 May 2023, IIT Guwahati

TH-3378_196103004

Patents

1. **Anand Mohan Pandey**, Sajan Kapil, and Manas Das "Systems and methods for removal of micro-printed parts deposited by electrodeposition" Indian Patent**, Application number**: 202331028369| **Patent filed.**
2. **Anand Mohan Pandey**, Sajan Kapil, and Manas Das "A Portable device for simultaneous coating and texturing of the surface by an electrochemical deposition-based process", Indian Patent **Application number**: 202331002410 | **Patent filed**

Indian Institute of Technology Guwahati

TH-3378_196103004